

THESIS FOR THE DEGREE OF DOCTOR OF PHILOSOPHY

Wideband THz Mixers and Components for the Next Generation of Receivers for Radioastronomy

Cristian Daniel López



CHALMERS
UNIVERSITY OF TECHNOLOGY

Group for Advanced Receiver Development
Department of Space, Earth and Environment
CHALMERS UNIVERSITY OF TECHNOLOGY
Gothenburg, Sweden 2024

Wideband THz Mixers and Components for the Next Generation of Receivers for
Radioastronomy
Cristian Daniel López
ISBN 978-91-7905-981-1

Acknowledgments, dedications, and similar personal statements in this thesis, reflect the author's own views.

© Cristian Daniel López, 2024.

Doktorsavhandlingar vid Chalmers tekniska högskola
Ny serie nr 5447
ISSN 0346-718X

Department of Space, Earth and Environment
Chalmers University of Technology
SE-412 96 Gothenburg
Sweden
Telephone + 46 (0)31-772 1000

Cover:

Top Left: 3D Model of Proposed Finline Mixer Chip. The different layers are indicated.

Top Right: Measurement setup inside a closed cycle cryostat. The setup was employed for the measurement of the relative insertion loss of slotline-to-microstrip transition at 4K.

Bottom Left: Fabricated electroplated finline for SIS over metal DC characterization.

Bottom Right: Scanning Electron Microscope (SEM) picture of the electroplated finline. The area in red is magnified in the insert.

Printed by Chalmers Dygitaltryck
Gothenburg, Sweden 2024

To my wife, Marcela
and my son, Björn



Abstract

In recent decades, there has been a growing interest in THz research, leading to substantial improvements in technology and the emergence of new applications. In particular, the ever-evolving field of radio astronomy instrumentation has been pushing the limits of millimeter and sub-millimeter technology boundaries, redefining the state-of-the-art for wideband low-noise receivers. The technological roadmaps for radio astronomy applications, such as “The ALMA 2030 Wideband Sensitivity Upgrade”, set the requirements for the next generation of heterodyne receivers. Among these requirements, it establishes the need for a wider IF bandwidth and the possibility of covering multiple existing RF bands with a single receiver, e.g., combining ALMA bands 6 (211–275 GHz) and 7 (275–373 GHz), i.e., a ~56% fractional bandwidth. To build receivers with such a large fractional bandwidth, each of their components must be able to cover the required bandwidth with minimal insertion loss, or equivalently, add the minimum noise to the system. In particular, it is essential to focus on the components that are critical for the performance of such receivers, such as front-end waveguide components and the mixer chip. This thesis addresses this need and focuses on the design, simulation, fabrication, and characterization of ultra-wideband THz devices for the next generation of radio astronomy receivers.

The thesis starts by presenting the development of waveguide passive components key to future ultra-wideband receivers, such as waveguide twists and power dividers. Waveguide twists are essential interconnection parts in most polarization-sensitive THz receivers that make use of orthomode transducers. Since compactness and low insertion loss are critical requirements, step-twists have become a promising solution. This work introduces novel designs for step twists covering the frequency ranges of 120-220 GHz and 210-375 GHz, i.e., 44% and 56% fractional bandwidth with 20 dB return loss, respectively. In the first design, the experimental verification showed an insertion loss of 0.4 dB, while the second demonstrated an insertion loss as low as 0.3 dB. Additionally, the thesis investigates waveguide power dividers, a fundamental component in the development of 2SB receivers for LO injection. It presents a waveguide power divider that incorporates a substrate-based element into a waveguide structure to enhance the output port’s isolation and matching in the frequency range of 150-220 GHz, i.e. 38% fractional bandwidth.

THz mixers are implemented with thin-film technology. As a consequence, the waveguide-to-substrate transitions have a fundamental role in the performance and bandwidth of such systems. In this work, a waveguide-to-slotline superconducting transition based on substrateless finlines is proposed. Moreover, for the majority of modern mixers with Superconductor Insulator Superconductor (SIS) technology, the microstrip line topology is the most suitable. Hence, this work presents the development of a broadband slotline to microstrip transition based on Marchand baluns. Both transitions were experimentally verified at cryogenic temperatures. Remarkably, each of these transitions achieved a fractional bandwidth of ~56%, while the substrateless finline transition demonstrated an insertion loss of 0.5 dB, the Marchand Balun showed an insertion loss as low as 0.3 dB. The integration of the substrateless finline and the Marchand balun transitions served as the first approach to a platform for the development of an ultra-wideband SIS mixer. This platform evolved into the SIS mixer design for 210-375 GHz introduced in this thesis. The mixer chip represents a significant shift from traditional design approaches since the dielectric substrate is removed and replaced with a micromachined metallic substrate which integrates a metallic finline. The micromachined substrate is employed as a technological platform for the Nb-Al/AlN-Nb SIS junctions, the RF matching circuitry, and the IF output filter. The mixer features a designed IF bandwidth of 4-16 GHz. Furthermore, this thesis demonstrates the feasibility of micromachined metallic substrates as a technological platform for SIS devices.

Keywords: Heterodyne receivers, Spectroscopy, Waveguide twist, Finline, Waveguide-to-Substrate Transition, Superconductor-Insulator-Superconductor (SIS) mixers.

List of Publications

Appended Papers

This thesis is based on the following papers:

Paper A: C. López, V. Desmaris, D. Meledin, A. Pavolotsky, & V. Belitsky, "Design and Implementation of a Compact 90° Waveguide Twist With Machining Tolerant Layout," in *IEEE Microwave and Wireless Components Letters*, vol. 30, no. 8, pp. 741-744, Aug. 2020, doi: 10.1109/LMWC.2020.3000833.

Paper B: C. López, D. Montofré, V. Desmaris, A. Henkel, & V. Belitsky, "Ultra-Wideband 90° Waveguide Twist for THz Applications," in *IEEE Transactions on Terahertz Science and Technology*, vol. 13, no. 1, pp. 67-73, Jan. 2023, doi: 10.1109/TTHZ.2022.3213468.

Paper C: A. Gouda, C. López, V. Desmaris, D. Meledin, A. Pavolotsky & V. Belitsky, "Millimeter-Wave Wideband Waveguide Power Divider With Improved Isolation Between Output Ports," in *IEEE Transactions on Terahertz Science and Technology*, vol. 11, no. 4, pp. 408-416, July 2021, doi: 10.1109/TTHZ.2021.3078876.

Paper D: C. López, V. Desmaris, D. Meledin, A. Pavolotsky, & V. Belitsky, "Waveguide-to-Substrate Transition Based on Unilateral Substrateless Finline Structure: Design, Fabrication, and Characterization," in *IEEE Transactions on Terahertz Science and Technology*, vol. 10, no. 6, pp. 668-676, Nov. 2020, doi: 10.1109/TTHZ.2020.3020683.

Paper E: C. López, M. A. Mebarki, V. Desmaris, D. Meledin, A. B. Pavolotsky, & V. Belitsky, "Wideband Slotline-to-Microstrip Transition for 210–375 GHz Based on Marchand Baluns," in *IEEE Transactions on Terahertz Science and Technology*, vol. 12, no. 3, pp. 307-316, May 2022, doi: 10.1109/TTHZ.2022.3149413.

Paper F: C. López, V. Desmaris, D. Meledin, A. Pavolotsky, & V. Belitsky, "Micromachined Metallic Substrates as a Technological Platform for Superconductor-Insulator-Superconductor Tunnel Devices ", *Manuscript submitted to Journal of Superconductor Science and Technology*.

Paper G: C. López, V. Desmaris, D. Meledin, A. Pavolotsky, & V. Belitsky, "Design and Simulation of an Ultra-Wideband 211-375 GHz SIS Mixer based on a Micromachined Metallic Substrate," **Accepted Manuscript to be presented for the 33rd IEEE International Symposium on Space THz Technology (ISSTT 2024), Charlottesville, VA, USA.**

Other Publications

The following publications are excluded from the thesis due to content overlap or because their content falls outside the scope of the thesis.

[I] C. López, V. Desmaris, D. Meledin, A. Pavolotsky, & V. Belitsky, "Surface modification of polytetrafluoroethylene thin films by non-coherent UV light and water treatment for electrowetting applications," *Progress in Organic Coatings*, 2020, vol. 149, p. 105593.

[II] C. López, V. Desmaris, D. Meledin, A. Pavolotsky, & V. Belitsky, "Broadband waveguide-to-substrate transition using a unilateral etched finline structure," *Proc. 30th Int. Symp. Space Terahertz Technol.*, 2019, pp. 47-48.

[III] A. Pavolotsky, C. López, I. V. Tidekrans, D. Meledin, V. Desmaris, & V. Belitsky, "Specific capacitance of Nb/Al-AlN/Nb superconducting tunnel junctions," *Proc. 30th Int. Symp. Space Terahertz Technol.*, 2019, pp. 92-94.

[IV] C. López, V. Desmaris, D. Meledin, A. Pavolotsky, & V. Belitsky, "Design and Implementation of a Broadband and Compact 90-degree Waveguide Twist with Simplified Layout," *Proc. 30th Int. Symp. Space Terahertz Technol.*, 2019, pp. 42-43.

[V] C. López, V. Desmaris, D. Meledin, A. Pavolotsky, & V. Belitsky "Design, Fabrication, and Characterization of Waveguide to Substrate Transition Based on Unilateral Substrateless Finline Structures," *Proc. 31st Int. Symp. Space Terahertz Technol.*, 2020.

[VI] D. Meledin, I. Lapkin, M. Fredrixon, E. Sundin, S. E. Ferm, A. Pavolotsky, M. Strandberg, V. Desmaris, C. López, P. Bergman, M. Olberg, J. Conway, K. Torstensson, C. Durán, F. M. Montenegro-Montes, C. De Breuck, & V. Belitsky, "SEPIA345: A 345 GHz dual polarization heterodyne receiver channel for SEPIA at the APEX telescope," *Astronomy & Astrophysics*, 668, A2, 2022, doi: <https://doi.org/10.1051/0004-6361/202244211>.

[VII] C. López, V. Desmaris, D. Meledin, A. Pavolotsky, & V. Belitsky, "Design and Fabrication of All-metal Micromachined Finline Structures," Presented at the 32nd International Symposium on Space THz Technology (ISSTT2022), Baeza, Spain, October 16-20, 2022.

[VIII] V. Belitsky, I. Lapkin, M. Fredrixon, C. López, S.-E. Ferm, A. Pavolotsky, M. Strandberg, E. Sundin, R. Hesper, J. Adema, J. Barkhof, A. Baryshev, M. Bekema, S. Realini, A. Koops, R. de Haan, M. Rodenhuis, F. Cuttaia, R. Nesti, S. Riccardi, F. Villa, A. Gonzalez, K. Kaneko, R. Sakai, H. Imada, T. Kojima, N. Phillips, P. Yagoubov, "ALMA Band 2 Cold Cartridge Assembly Design," 32nd International Symposium on Space THz Technology (ISSTT2022), Baeza, Spain, October 16-20, 2022.

[IX] D. Montofré, I. Lapkin, L. Helldner, M. Fredrixon, C. López, V. Desmaris, & V. Belitsky, "A broad-band and dual-polarization single layer dichroic filter for applications in Sub-THz Range," Presented at the 32nd International Symposium on Space THz Technology (ISSTT2022), Baeza, Spain, October 16-20, 2022.

[X] I. Lapkin, **C. López**, M. Fredrixon, A. Pavolotsky, S. E. Ferm, V. Desmaris, & V. Belitsky, "Vacuum-Seal Waveguide Feedthrough for Extended W-Band 67–116 GHz," *IEEE Journal of Microwaves*, vol. 3, no. 3, pp. 1014-1018, July 2023, doi: 10.1109/JMW.2023.3279690.

[XI] D. Montofré, D. Meledin, **C. López**, I. Lapkin, V. Desmaris, L. Helldner, M. Fredrixon, S. E. Ferm & V. Belitsky, "A Broad-Band Dual-Polarization All-Metal Dichroic Filter for Cryogenic Applications in Sub-THz Range," in *IEEE Transactions on Terahertz Science and Technology*, 2023, doi: 10.1109/TTHZ.2023.3338472.

Acknowledgments

I would like to thank my main supervisor, Prof. Vincent Desmaris, for his constant support, helpful teachings, and advice during my PhD studies. Special thanks to my examiner, Prof. Victor Belitsky, for sharing his wide knowledge and continued guidance. I'm also grateful to Dr. Denis Meledin for his friendship, lab mentoring, and his assistance whenever needed. My gratitude goes to Dr. Alexey Pavolotsky for his assistance in the cleanroom and for the interesting discussions we had over the many hours we spent there. In addition, I would like to express sincere thanks to my colleagues and friends at GARD for their constant encouragement and support.

Me gustaría agradecer a mi esposa, Marcela, que me ha acompañado siempre en este largo y difícil proceso. Por estar ahí, esperándome cuando los días de trabajo parecían no tener fin, por cuidar a nuestro pequeño en esas largas noches en las que escribí esta tesis, por ayudarme a encontrar soluciones y compartir sus ideas, por apoyarme en los momentos más duros en los que solo estábamos nosotros contra el mundo y por tu gran amor. Siéntete orgullosa, esta tesis también es tuya. Lo logramos.

Finalmente, me gustaría agradecer a mi buen e incondicional amigo, Esteban Quito, que siempre estuvo a mi lado.

List of Abbreviations

ALMA	Atacama Large Millimeter/Submillimeter Array
APEX	Atacama Pathfinder Experiment
Au	Gold
BCS	Bardeen, Cooper and Schrieffer
CNC	Computer Numerical Control
CPW	Coplanar Waveguide
DC	Direct Current
DSB	Double Sideband
EHT	Event Horizon Telescope
GaAs	Gallium Arsenide
GHz	Gigahertz
HEB	Hot Electron Bolometer
HFSS	High-Frequency Structure Simulator
IF	Intermediate Frequency
InP	Indium Phosphide
IV	Current Voltage
LNA	Low Noise Amplifier
LO	Local Oscillator
MgO	Magnesium Oxide
NOEMA	Northern Extended Millimeter Array
Nb	Niobium
Nb/Al-AlN/Nb	Niobium/Aluminum-Aluminum Nitride/Niobium junction
Nb/Al-AlO _x /Nb	Niobium/Aluminum-Aluminum Oxide/Niobium junction
OMT	Orthomode Transducer
RF	Radio Frequency
RIE	Reactive Ion Etching
S2B	Sideband Separating Mixer
SEM	Scanning Electron Microscope
SIS	Superconductor-Insulator-Superconductor
SSPPs	Spoof Surface Plasmon Polaritons
Si	Silicon
SiN	Silicon Nitride
SiO ₂	Silicon Dioxide
TE	Transverse Electric mode
THz	Terahertz
TRL	Thru Reflect Line
UV	Ultraviolet
VLBI	Very Long Baseline Interferometry

Contents

Abstract	iv
List of Publications	v
Other Publications	vi
Acknowledgments	viii
List of Abbreviations	ix
1 – Introduction	1
1.1 – Exploring the Universe: mm and Sub-mm Radioastronomy	1
1.2 – Concepts on Radioastronomy Receivers.....	4
1.2.2 – SIS working principles.....	5
1.2.3 – Concepts of Heterodyne Detection.	6
1.3 – Motivation of the Thesis	8
2 – Waveguide Components for Wideband THz Receivers	11
2.1 – Waveguide Components	11
2.2 – Compact Wideband Waveguide Twists with Low Insertion Loss.....	12
2.2.1 – An Overview of Waveguide Twists.....	12
2.2.3 – Principle of operation of Step twists.....	13
2.2.4 – Design and Performance of Wideband 90° Twists	14
2.2.5 – Comparative Analysis with Existing Designs.....	15
2.3 - Novel Waveguide 3dB Power Divider with Matched Ports	16
2.3.1 – Overview of Power Dividers	16
2.3.2 – Design and Performance of Waveguide Power Divider	17
2.3.3 – State-of-the-Art Comparison	18
3 – Waveguide to Microstrip Transition for Prospective 2SB SIS Mixers	21
3.1 – A Review of Waveguide-to-Substrate Transitions.....	21
3.1.1 – Probes.....	21
3.1.2 – Finlines.....	22
3.2 - Advancements in Finline Technology for THz Applications	25
3.2.1 – Substrateless Finlines.....	25
3.2.2 –Analysis of State-of-the-Art Waveguide to Substrate Transitions	27
3.3 – Wideband Slotline-to-Microstrip Transition.....	30
3.3.1 – Overview of Slotline-to-Microstrip Transitions	30
3.3.2 – Wideband Low-Loss Slotline-to-Microstrip Transition	32

4 – A Novel Ultra Wideband SIS Mixer.....	35
4.1 – Modern SIS Mixers	35
4.1.1 – Fundamentals of SIS Mixer Design.....	35
4.1.2 – RF matching techniques for SIS junctions.....	37
4.1.3 – Overview of Nb-based SIS junctions: Nb/Al-AlO _x /Nb and Nb/Al-AlN/Nb ...	39
4.1.4 – State of The Art SIS Mixers.....	40
4.2 – Ultra-Wideband SIS Mixer Design and Simulation.....	43
4.3 – A Novel Technological platform for SIS mixer Design	45
4.3.1 – Motivation.....	45
4.3.2 – DC Testing and Results	48
5 Concluding Remarks and Future Outlook.....	49
Bibliography	51

Chapter 1

Introduction

The human eyes perceive a small fraction of the electromagnetic spectrum that is commonly referred to as visible light. Nevertheless, the electromagnetic spectrum extends far beyond the optical region, and it is traditionally divided into: radio waves, microwaves, THz, infrared, visible light, UV, and X-rays, as depicted in Fig. 1.1. Among these spectral regions, the THz range, which falls between 100 GHz (corresponding to a wavelength of 3 mm) and 10 THz (corresponding to a wavelength of 30 μm) [1], has recently drawn increasing attention in the scientific community. The interest in this particular frequency range is motivated by its numerous applications in multiple areas such as instrumentation for medical science [2], material science [3], and radioastronomy [4]. Moreover, the continuous advancement in generation and measurement techniques at this frequency range is taking the THz wireless communications systems one step closer to reality [5]. These advancements have been led by the research on radioastronomy instrumentation which has continuously pushed the technological boundaries and redefined the state-of-the-art technology at THz frequencies [6-8].

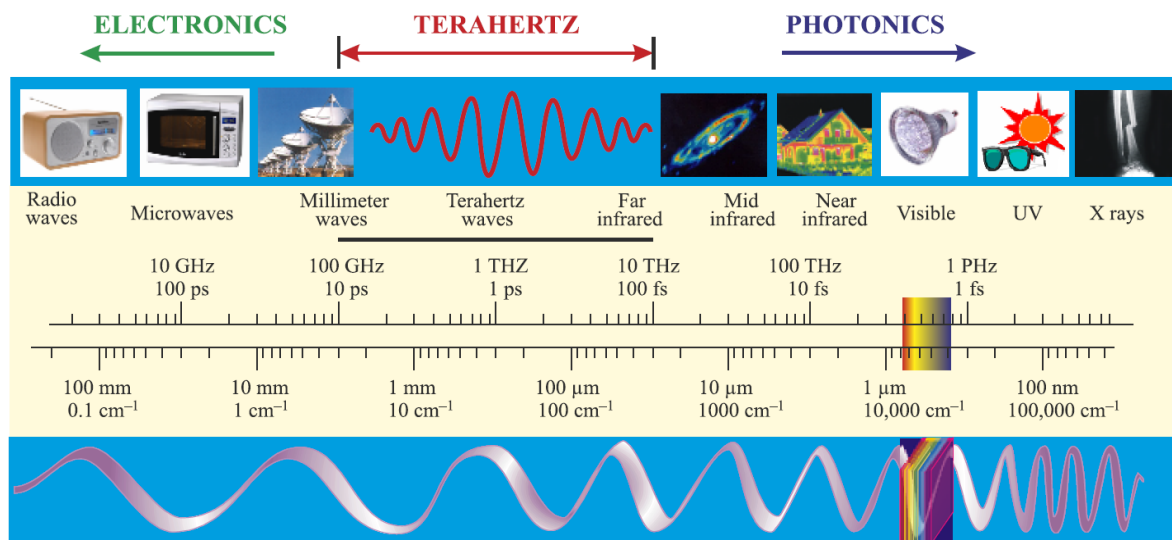


Fig.. 1.1. Illustration of the electromagnetic spectrum divisions and frequency ranges. Reproduced from [1].

1.1 – Exploring the Universe: mm and Sub-mm Radioastronomy

A large part of the universe and its phenomena are invisible to optical wavelengths since they occur in regions of space so cold that they do not radiate enough light in the visible spectrum. Furthermore, the opacity of the interstellar dust at optical frequencies prevents telescopes operating in the visible light spectrum from detecting a substantial number of these cosmic phenomena. This part of space is frequently referred as the “cold universe”. The "cold

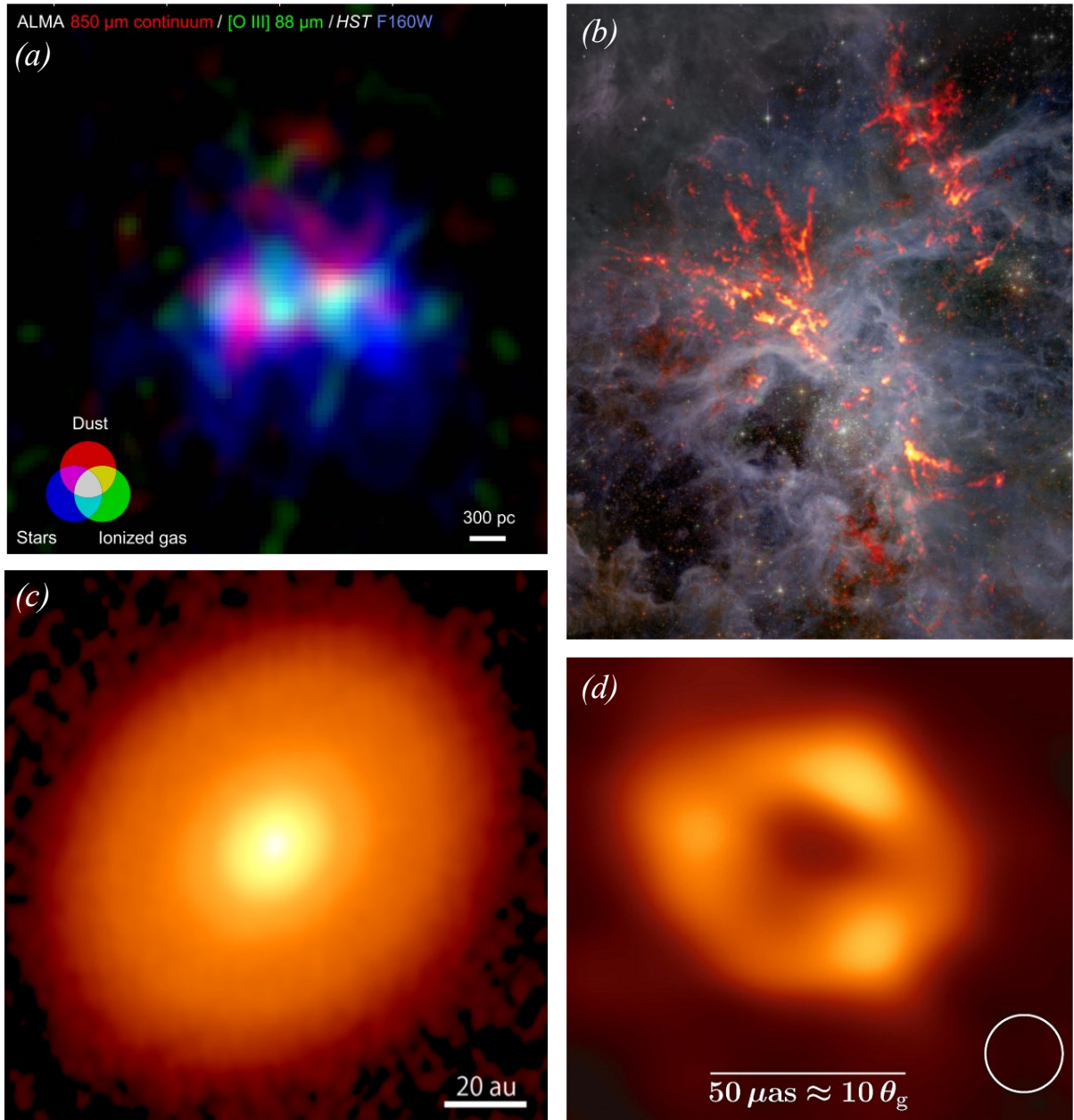


Fig. 1.2. Selection of recent radio astronomy observations. (a) Image of a young galaxy from a period just 600 million years after the Big Bang. This discovery provides valuable insights into the early stages of galaxy formation [9]. (b) 30 Doradus is a large star-forming region located in the heart of the Tarantula Nebula. The image is a composite, of red/orange millimeter-wavelength data from ALMA and data from the Hubble Space Telescope (HST) [10]. (c) High-resolution ALMA image of the protoplanetary disk surrounding DG Taurus at a 1.3 mm wavelength. The smooth appearance, absent of ring-like structures, indicates a phase shortly preceding planet formation [11]. (d) The first image of Sagittarius A, the supermassive black hole at the center of our Milky Way galaxy, was released by the EHT Collaboration in May 2022 [12].

universe " can be investigated by the observation in the mm and sub-mm range. This frequency range is essential for studying molecular lines to determine the chemical and physical characteristics of astronomical objects, seeing through optically thick cosmic dust to uncover stellar and planetary formation processes, and observing the dense molecular clouds where stars and planets are formed [13]. Furthermore, redshift is the phenomenon in which light from distant objects in the cosmos, such as galaxies, shifts to the longer wavelengths, i.e., towards the red end of the visible electromagnetic spectrum. This shift is primarily due to the expansion of the universe, which causes these objects to travel away from us. In other words, this phenomenon shifts the light originally emitted in the optical or infrared into the millimeter and submillimeter range by the time it reaches us. Therefore, mm and sub-mm astronomy is particularly well suited to make observations going back into the early universe, observing light from distant objects, and detecting redshifted continuous emission from and beyond the peak of dust thermal emission. The measured continuum emission reveals important information about dust mass and temperature, star formation activity in dusty regions, and the mass of the interstellar medium (ISM). For instance, it is possible to image distant galaxies and investigate gravitational lensing phenomena [13].

Exploring the universe in the mm and sub-mm range has inspired worldwide efforts to develop and build radio telescopes to perform high-resolution observations. In the last decade, these observations have led to significant milestones for radio astronomy. For instance, the first picture of a supermassive black hole was taken by the Event Horizon Telescope (EHT) [14]. The EHT makes use of Very Large Baseline Interferometry (VLBI), which involves employing multiple telescopes to form a virtual telescope the size of the maximum distance between them. This approach significantly improves spatial resolution and sensitivity, allowing astronomers to view details at much larger distances than a single telescope could. VLBI has been crucial in making groundbreaking observations, such as photographing the black hole in the M87 galaxy, by merging signals from multiple telescopes across the world e.g. the Northern Extended Millimeter Array (NOEMA) [15], the Atacama Pathfinder Experiment (APEX) [16] and the Atacama Large Millimeter/Submillimeter Array (ALMA) [13]. In Fig. 1.2, a small selection of recent radio astronomy observations at these frequencies is shown.

The Atacama Large Millimeter/submillimeter Array (ALMA) is located in northern Chile's Atacama desert at an elevation of 5000 meters on the Chajnantor plateau where the high altitude and minimal precipitable water vapor provide ideal observation conditions. This makes ALMA, with its 66 reconfigurable antennas, one of the most sensitive ground based telescopes ever built for high-resolution investigations at millimeter and submillimeter wavelengths [19]. Each antenna has eight receiver bands that cover frequencies ranging from 84 to 950 GHz, and with the full deployment of Band 1 [17] and 2 [18], this range is extended down to 35 GHz (0.3 to 8.6 millimeters). As it is found in other telescopes operating at this frequency range, the receivers employ state-of-the-art heterodyne technology that provides the highest spectral resolution ($\lambda/\Delta\lambda > 10^6 - 10^7$). In addition, most of these heterodyne receivers rely on superconducting detectors based on Superconductor/Insulator/Superconductor (SIS) junctions. SIS Mixers have become one of the most common mixers in this frequency range since they provide an outstanding sensitivity, achieving noise levels close to the quantum limit [6]. For instance, 8 out of ten receivers of ALMA employ SIS technology [19]. The next section provides a quick outline of the technological principles behind radioastronomy receivers that are relevant to the thesis.

1.2 – Concepts on Radioastronomy Receivers

1.2.1 – Radioastronomy Detectors

The radio astronomy receivers are intended to detect extremely weak signals that can easily be outpowered by noise. The noise affecting the receiver might come from external and internal sources. However, the noise produced in the detector itself is a major factor in the noise performance of the receiver. Therefore, the detector noise must be minimized. This requirement is critical for the receiver performance since the sensitivity of the radiotelescope is intrinsically related to the noise temperature [20] [139]:

$$\Delta T_{min} \propto \frac{T_{SYS}}{\sqrt{\Delta\tau B}} \quad (1.1)$$

where ΔT_{min} is the sensitivity, understood as the minimum variation in the input signal that the system can detect, while τ_{int} is the integration time, and B and T_{SYS} are the bandwidth and the noise temperature of the system, respectively. It is essential to mention that T_{SYS} is defined for the entire system and includes the contributions of the receiver, antenna, atmosphere, and background. From equation 1.1, it can be seen that the system noise temperature is linearly related to the sensitivity. In contrast, the dependence on the integration time is the inverse of the square root. Note that the integration time is limited by the stability of the receiver and the 1/f noise. These relations indicate that reducing the system noise temperature is the most efficient option to increase the sensitivity.

The radio astronomy receiver's low noise and high-frequency operation requirements have inspired the development of three leading technologies with their advantages and disadvantages. Schottky diode mixers emerge as an attractive solution due to their large IF bandwidth and wide temperature range of operation [25]. These detectors are frequently employed in space-borne missions since they do not require cryogenic temperatures to operate [142]. However, the demand for a considerable LO power (\sim mW) and the comparably high noise temperature make them less attractive for applications that require the ultimate sensitivity. Recently, other technologies that provide highly compact solutions at room temperature operation have been tested for the development of receivers, such as BiCMOS [143].

Superconducting hot electron bolometers (HEB) provided the best noise performance for frequencies above \sim 1.2 THz [78]. Their principle of operation relies on heating with microwave radiation an ultrathin superconducting film. As the heating process does not depend on the frequency of the incident radiation, HEB can provide nearly unlimited RF bandwidth. Nevertheless, the thermal response sets a limit in the IF bandwidth of HEB mixers. Even though substantial progress towards larger IF bandwidths has been made in recent years [8,22], the IF bandwidth remains the main challenge for HEB mixers.

Superconductor-insulator-superconductor (SIS) mixers present an outstanding noise performance in the frequency range from 100 GHz to 1.2 THz. In particular, it is possible to approach the theoretical quantum noise limit for a double sideband configuration (DSB) as $hf/2k$, as was demonstrated in [6,23]. Since in this thesis a wideband SIS mixer is designed and simulated, the next subsection details the most basic principles of SIS junction operation.

1.2.2 – SIS working principles

The working principle behind SIS mixers lies in the photon-assisted quasiparticle tunneling through a superconductor-insulator-superconductor SIS tunnel junction. Fig 1.3a illustrates the energy level diagram of a SIS structure employing a semiconductor representation. From the figure, it can be seen that a gap exists between the filled states (shaded) and the empty states. Ideally, at $T=0\text{K}$, the energy states are occupied by paired electrons denominated "Cooper pairs". Meanwhile, at $0 < T < T_{\text{critical}}$, a fraction of superconducting pairs breaks into single electrons, and they are excited into a quasiparticle energy state [25]. When the SIS is biased to a voltage level of $V_b \geq 2\Delta/e$, where " Δ " is the superconductor bandgap, and " e " is the electron's charge, the filled states on the left approach the level of the unfilled band on the right. Therefore, the quasiparticles can tunnel through the insulating layer. In the presence of a photon source with energy hf , the tunneling can occur at a lower bias voltage, i.e. hf/e . This phenomenon is used for developing heterodyne mixers. It is important to note that the tunneling of Cooper pairs, known as the Josephson Effect, is an undesirable effect in SIS mixers since it increases the overall noise. Thus, a steady magnetic field is employed to suppress Cooper pair tunneling. Another interesting feature of SIS mixers is that in contrast to conventional mixers, it is possible to have conversion gain as described in [24].

The SIS junction's structure sets limits for the intermediate frequency (IF) bandwidth and the operational frequency since the IF bandwidth is limited by the geometrical capacitance of the junction. Moreover, the IF bandwidth is further limited by the tuning circuitry capacitance.

The choice of a mixer technology will depend on the characteristics of the radiotelescope, frequency of operation, and noise requirements. Moreover, the receiver detection could be

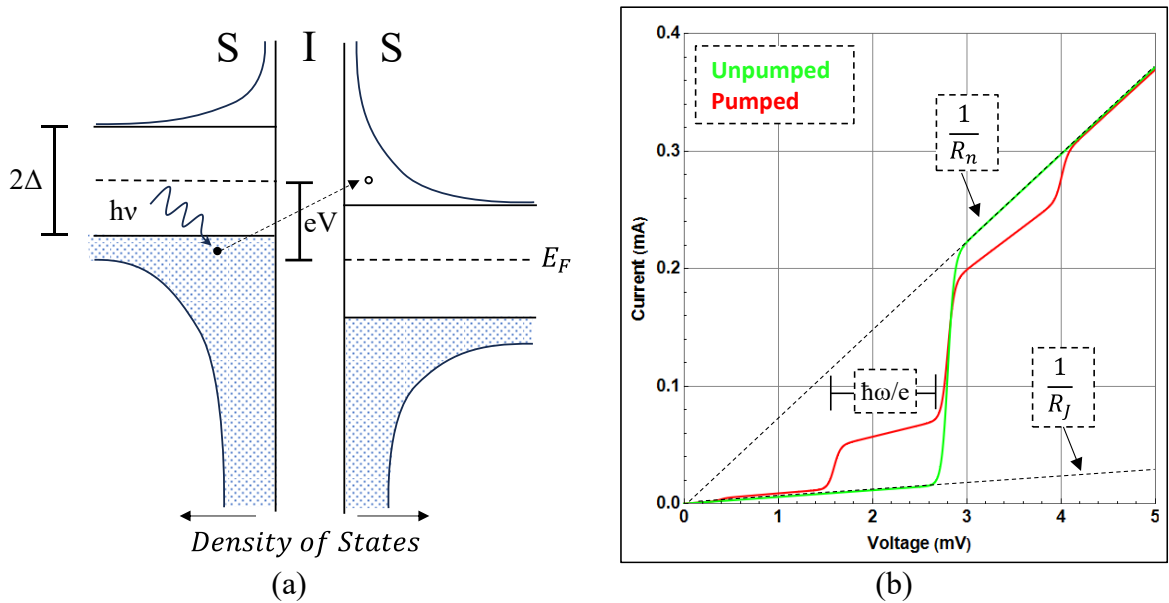


Fig. 1.3. SIS principle of operation. (a) Energy bands of a biased superconducting-insulating-superconducting (SIS) structure. The copper pair is broken by the incoming photon which allows the quasiparticle to tunnel through the insulator. (b) Simulated current voltage curve (IVC) for Unpumped (green), i.e., without LO power applied to the junction, and Pumped (red), i.e. when LO power is applied to the junction. Moreover. The photon assisted tunneling step below the gap is shown. Note that V_g is 2.8 mV. The normal resistance of the junction and the subgap resistance (R_n) are indicated as the inverse of the slope for the normal and subgap regions of the SIS. Since R_J is related to the subgap leakage current, the relation R_J/R_n is employed as a measure of the quality of the junction.

coherent or incoherent. In contrast to incoherent detection, heterodyne (coherent) receivers preserve the phase information of the incoming radiation. The following section elaborates on the key concepts of heterodyne detection.

1.2.3 – Concepts of Heterodyne Detection

A frequency mixer is essentially an analog multiplication of two signals with different frequencies denominated Local Oscillator (LO) and Radio Frequency (RF) in a nonlinear element, such as a SIS junction. The LO is generated in a reference source, while the RF signal presents the information of interest. The mixing between the LO and the RF produces the IF signal that fully preserves the phase and amplitude of the RF information. The mixer output signal has a frequency higher or lower than the input signal depending on whether the process is up-conversion or down-conversion. Radio astronomy receivers make use of the down-conversion process to detect and process the high-frequency signals that come from celestial objects, e.g. [6,26,27,28].

Heterodyne receivers operate in a variety of modes, depending on the receiver configuration and measurement needs. The DSB mode, shown in Fig. 1.4, combines the lower and upper sidebands into a single IF signal, making them indistinguishable. When only one sideband

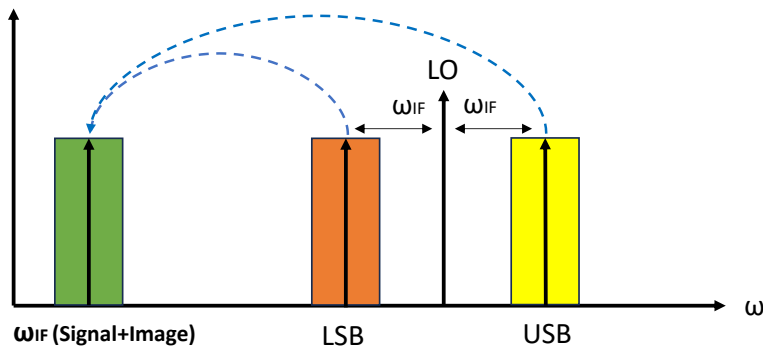


Fig. 1.4. Illustration of the downconversion employing DSB mixer configuration.

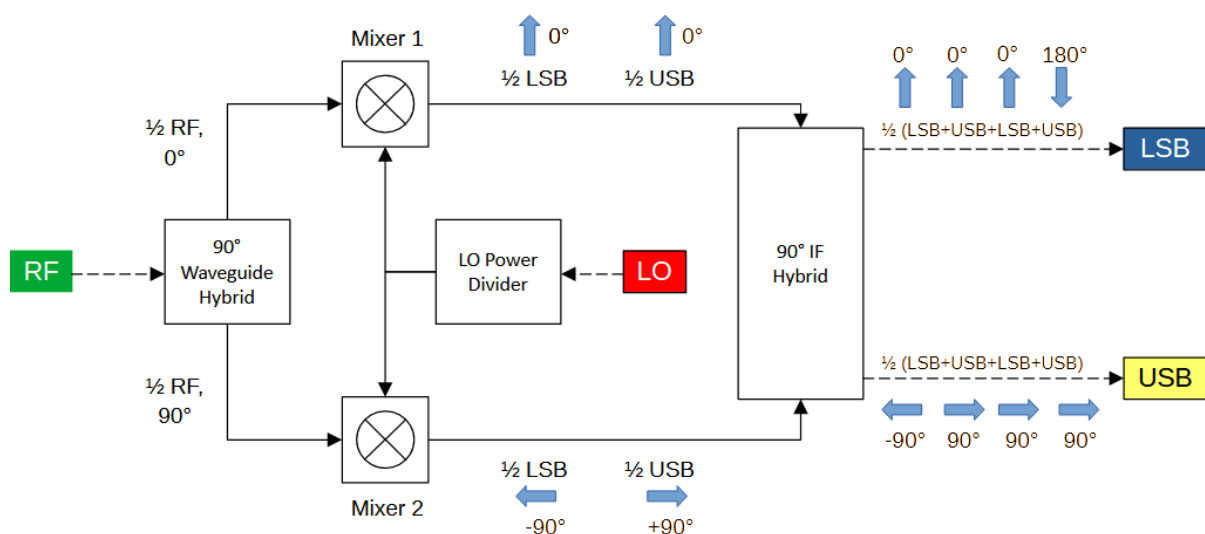


Fig. 1.5. Block Diagram of a Sideband Separating Mixer 2SB. The signal phasor for each sideband illustrates the sideband separation process.

needs to be observed a Single Sideband (SSB) mode is employed, filtering out the sideband that is not needed. SSB eliminates one sideband but retains the associated noise, theoretically doubling the noise temperature over the DSB configuration [45].

When both sidebands are to be observed separately, a sideband separating mixer (2SB) is employed. Fig. 1.5 depicts a block diagram for a receiver with 2SB operation. This setup requires two DSB mixers. The RF signal is split with a 90-degree phase difference using an RF quadrature 3dB hybrid, and the LO power is symmetrically divided across two mixers, e.g. using a waveguide power divider. Then, the IF outputs are combined in a quadrature 3dB IF hybrid to achieve sideband separation. The quadrature hybrid's outputs are connected to independent amplification chains with Low Noise Amplifiers (LNA). Note that ideal sideband separation, however, is dependent on the precise division and phase precision of the RF and LO signals.

For radioastronomy receivers, the trend is toward 2SB receivers, as indicated by modifications such as those in BAND 9 and 10 from their initial DSB configurations [19].

It is essential to note that radio astronomy receivers operating below ~100 GHz incorporate an RF low noise amplifier (LNA) as the first stage, e.g. ALMA band 2 receiver [18]. Even though LNA technology is progressing towards frequencies above ~100 GHz, e.g. [29,30], RF LNAs are not employed in high-frequency receivers since the noise of such devices so far is too large compared to the extremely sensitive SIS mixer. Therefore, the inclusion of an RF LNA would deteriorate the noise performance of the system.

1.2.4 – System Noise Temperature

Since the temperature of a system is inherently connected to the generated noise power, the measurement of equivalent noise temperature provides a figure of merit to evaluate the receiver's performance. The equivalent noise temperature could be defined as the absolute temperature of an equivalent resistor that would generate the same noise as the component [31].

The equivalent noise temperature of a passive device is tightly connected to its losses [31]:

$$T_e = (L - 1)T \quad (1.2)$$

where T is the temperature of the passive device, and L is defined as the loss of signal power resulting from the insertion of the passive device in the transmission path. Therefore, reducing the system noise might be achieved by minimizing their components' losses and decreasing operation temperature. Both strategies are implemented in radio astronomy receivers where the losses are carefully optimized, and the system is generally cooled down to cryogenic

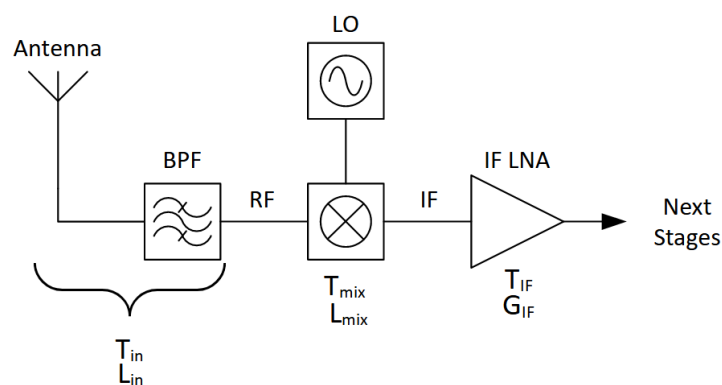


Fig. 1.6. Simplified block diagram for heterodyne receivers for radio astronomy applications.

temperature to reduce the thermal noise. It is important to note that the cryogenic operation is not only grounded by noise reduction but also required for the superconducting detectors' function.

The system noise temperature for the receiver of Fig. 1.6 is defined by cascading the individual contribution of each component as follows:

$$T_{sys} = T_{in} + L_{in} \left[T_{mix} + L_{mix} \left(T_{IF} + \frac{T_{next_stage}}{G_{IF}} \right) \right] \quad (1.3)$$

From the equation, it becomes clear that the first stages significantly impact the overall system noise temperature. In SIS mixer radio astronomy receivers operating beyond ~100 GHz, LNAs are not useful since the noise added by this component as first stage amplifier would dominate the overall system noise temperature. Thus, the SIS mixer is employed as the first stage of the system. It is important to note that SIS mixers can achieve conversion gain [24], and therefore, the term L_{mix} could be replaced by $1/G_{mix}$ which will help to reduce the overall T_{sys} . T_{in} represents the noise of the antenna, optics and all the components located before the mixer stage, e.g. waveguide to substrate transitions and, in polarization-sensitive receivers [6,28,32], OMT and waveguide twist. Moreover, the losses of such components are represented by L_{in} . From equation 1.3, it is seen that the input losses should be minimized to reduce their impact on the overall system noise temperature. Therefore, the minimization of losses was one of the main requirements for the design of the devices presented in this thesis, i.e. waveguide to substrate transitions, and waveguide twist.

1.3 – Motivation of the Thesis

A large number of radio astronomy observations are performed employing state-of-the-art heterodyne receivers with high spectral resolution. Although modern THz receivers have already achieved an outstanding performance [6,26,28], the science goals set for the next decades will demand remarkable technological development. The recommendations found in technological roadmaps such as The ALMA roadmap to 2030 [33], The ALMA20230 Wideband Sensitivity Upgrade [19], and VLBI2030: “A scientific roadmap for the next decade - The future of the European VLBI Network” [34], reflect the needs for the next generation of radioastronomy receivers. Among the requirements for future receivers set in these roadmaps, the following stand out: wider instantaneous bandwidth, i.e. to double or quadruple the current IF bandwidth. Since the RF and IF signals are inextricably tied in the mixing process, it is natural to require wider RF bandwidth too. This is already in progress in new ALMA receiver developments such as the BAND6v2 [36], the demonstration of the BAND 7+8 [35] mixer, and the updated BAND 2 [18]. For instance, the upgraded BAND 2, covers both the original ALMA Band 2, i.e. 67-90 GHz, and the original ALMA Band 3, i.e. 84-116. Furthermore, the upgraded BAND 2 has an IF Range of 4-18 GHz with a future goal to reach 4-20 GHz. Moreover, as depicted in Table 1.1., future receivers are intended to employ 2SB configurations with increased sensitivity in the whole band, i.e. lower noise levels.

To answer the needs of the next generation of radioastronomy receivers, the present thesis proposes various ultra-wideband devices for THz receivers: a set of waveguide twists [**Paper A**] and [**Paper B**], a power divider [**Paper C**], a cryogenic waveguide to substrate transition [**Paper D**], a cryogenic slotline to microstrip transition [**Paper E**], the development of a technological platform for THz applications [**Paper F**], and the design of a novel SIS mixer featuring the newly developed technological platform [**Paper G**].

Table 1.1 - ALMA Bands and Future Upgrade

Band	Original			Future ALMA 2030		
	RF Range [GHz]	IF Range [GHz]	Type	RF Range [GHz]	IF Range [GHz]	Type
1	35-50	4-12	SSB	35-50	4-12	SSB
2	67-90	-	-	67-116	4-16	2SB
3	84-116	4-8	2SB	*	$\geq 4-12$	
4	125-163	4-8		*	$\geq 4-12$	
5	163-211	4-8		*	$\geq 4-12$	
6	211-275	4.5-10		209-281	4-16	
7	275-373	4-8		*	$\geq 4-12$	
8	385-500	4-8		*	$\geq 4-12$	
9	602-720	4-12		*	$\geq 4-12$	
10	787-950	4-12		DSB	*	

Extracted from [19] . The future receivers with "*" indicate that the RF coverage might be upgraded.

Chapter 2

Waveguide Components for Wideband THz Receivers

2.1 – Waveguide Components

Radio astronomy receivers use waveguide components to transport RF and LO signals. Fig. 2.1a depicts the main components of an S2B design, e.g. ALMA Band 5 mixer assembly. The feed horns and orthomode transducers (OMTs) are some of the most important components in terms of receiver performance. The feed horn is used to couple incoming electromagnetic radiation into the waveguide system, and the OMT, which is connected to the feed horn's output, is critical for polarization discrimination [37]. OMTs, which are commonly utilized in current polarization-sensitive receivers [6, 28], detect the polarization of the incoming signal. Given that OMT outputs are typically orthogonal, waveguide twists are required to rotate the E field by 90° , allowing integration of the two signal chains into a single receiver system, as shown in Fig. 2.1. The waveguide twists must achieve E-field rotation with minimal losses since they are located in the RF channel before the mixer. Therefore, the twist losses have a direct impact on the receiver's noise performance and the symmetry of the polarization chains.

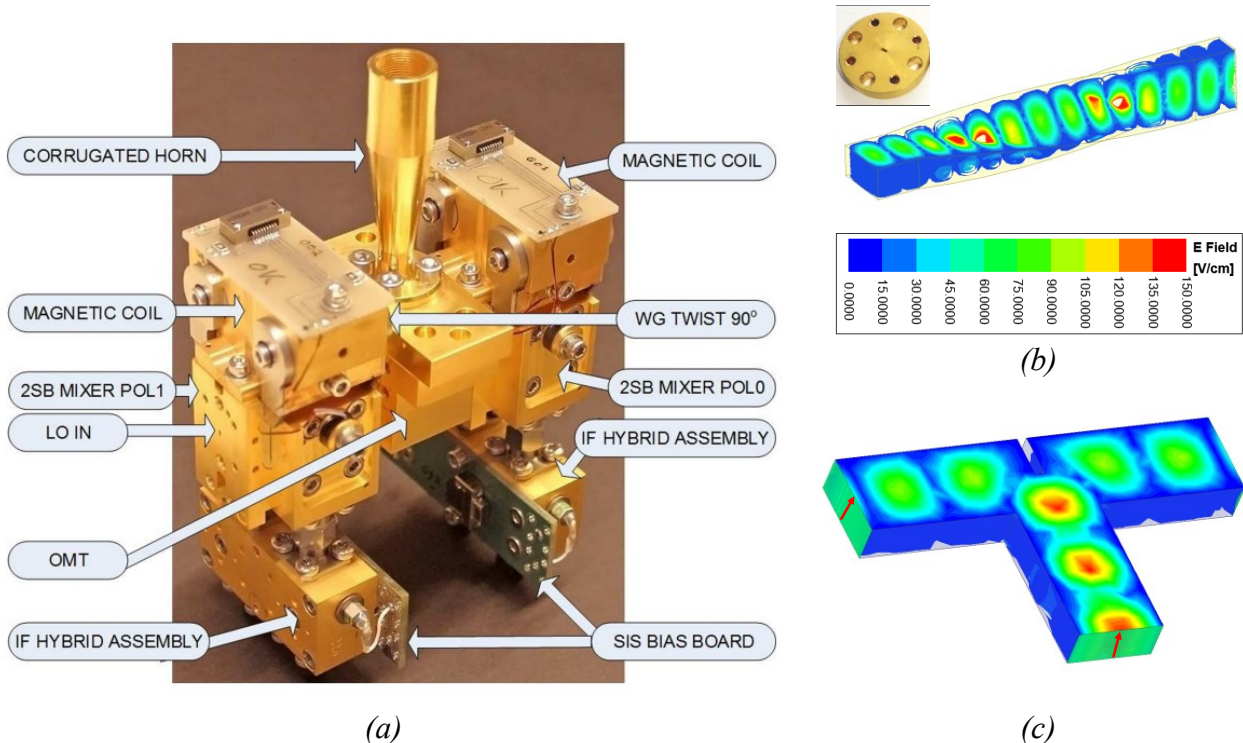


Fig. 2.1. (a) Example of S2B mixer assembly, ALMA Band 5 [38]. Various waveguide components are shown: For instance, corrugated horn, OMT, 90° continuous Waveguide Twist, IF hybrids (b) E-field magnitude simulation of a continuous twist. It is appreciated how the E-field of the rectangular waveguide main mode is gradually rotated along the continuous twist. Top: left image of continuous 90° waveguide twist employed in [38]. (c) E-field magnitude simulation of a classical waveguide power divider based on T-Junction with septum.

It is important to note that compact and low-loss waveguide twists are critical not only in radioastronomy but also in various mm-wave and sub-mm systems, including satellite systems with limited space and RF power [39].

Other key components in S2B designs include LO couplers, which inject a fraction of the LO power into the mixer, as well as RF and IF quadrature hybrids, which evenly divide the incoming signals and allow sideband separation. Moreover, power dividers are also required to equally distribute the LO signal to each SIS DSB mixer. The majority of power dividers used in modern radioastronomy receivers are simple three-port waveguide designs with a septum as depicted in Fig. 2.1c. These power dividers are intended to transmit half of the LO power to each output port without dissipation. However, their output matching and isolation performance is relatively poor, which means that reflections from one side can interfere with the other output port. This has an impact on the receiver's noise temperature and sideband rejection ratio (SBR), which are important metrics for determining the receiver's performance.

2.2 – Compact Wideband Waveguide Twists with Low Insertion Loss

2.2.1 – An Overview of Waveguide Twists

A great variety of 90° waveguide twists have been extensively studied in recent years to achieve compactness, low insertion loss, and minimum reflections [40-50]. These designs tend to differentiate from commercially available solutions where continuous rotation twists are frequently employed. Continuous twist relies on the gradual rotation of the E-field inside a twisted rectangular waveguide, as shown in Fig. 2.1b. The gradual rotation guarantees broadband operation with minimum reflections. However, continuous twists require a length of several guided wavelengths, which makes them incompatible with highly integrated waveguide systems. Moreover, the electroforming process employed for its fabrication is costly and takes a significant amount of time.

Variant forms of continuous twists do not employ continuous rotations of a rectangular waveguide. Instead, these twists progressively change their cross-sectional shape until the rectangular waveguide is rotated. This approach was first proposed in [51]. Notably, a similar approach was implemented in the 220-330 GHz frequency region, as demonstrated in [40], yielding good results. Other examples are documented in the literature, including those discussed in [50] and [52]. Progressive twists provide reasonably wideband performance and are more compact than their continuous counterparts, nonetheless, they still require a minimum length close to a wavelength to achieve field rotation [52].

An alternative solution is found in step-twist which introduces 1 or more waveguide segments with identical cross sections that rotate the E-field of the input waveguide. The design presented in [41-43], explores multi-step twists. These twists are formed by a series of waveguide sections that are gradually rotated until the full E-field rotation is achieved. Although this solution is less bulky than a continuous twist, its fabrication is rather complicated since each section is frequently fabricated individually. Furthermore, the overall performance of the multi-step twists depends on the fabrication and mounting tolerances of each section. Therefore, these twists are especially challenging to implement at higher frequencies where mounting tolerances are more critical. Therefore, the integration of the multistep into a split block technology is desirable such as in the design presented in [40]. Nonetheless, in these

cases, the shape of each section is limited due to CNC capabilities. In this thesis, a 2-step twist is proposed. The design is optimized for fabrication through direct milling on a single washer **[Paper B]**.

The single-step twists constitute the most compact solution. In this approach, a single waveguide section is inserted with half the angle of rotation, which allows the E-field to rotate. The bandwidth and performance of these twists are related to the shape of the cross-section of the step twist. As a consequence, various shapes have been extensively studied [48, 47, 44, 50]. In particular, the corner-cut shapes with multiple sharp corners have been widely adopted since they tend to maximize the bandwidth of the twist. The sharp corners are rather challenging to fabricate with simple techniques such as direct milling, especially at higher frequencies. This has led to alternative fabrication methods, as presented in [49], where micromachining techniques are employed for producing a 90° step twist. Although micromachining allows to precisely define the cross-section shape, it is so far a rather complicated and expensive process for waveguide twists. To address this problem, in **[Paper A]**, I demonstrate a novel compact wideband 90° twist with a performance less sensitive to geometry variations.

2.2.3 – Principle of operation of Step twists

To rotate the E-field in a rectangular waveguide, a discontinuity is introduced, resulting in the excitation of evanescent modes. These modes exist within the step twist cavity but do not propagate into the rectangle waveguide. This notion is discussed in [47]. The discontinuity created by a step twist is often inductive [47]. Moreover, in an ideal single-step twist scenario, the discontinuities at the input and output are identical. If the step thickness is about a fourth of the guided wavelength ($\lambda_g/4$) of the dominant mode in the twist cavity, these discontinuities can mutually cancel. Note that the alignment of the twist with the input and output waveguides is critical to avoid in-band resonances, as demonstrated in **[Paper A]**.

In the case of multi-step twists, two scenarios are possible: If the steps have a cross-section of a rotating rectangular waveguide equal in size to the input/output waveguides and the rotation angle remains constant, the reactive discontinuities are equal and they will cancel out if the thickness of each section is $\lambda_g/4$. Second, if the cross-section of the steps is not rectangular **[Paper B]**, the discontinuities between steps differ from those at the input and output. As a result, the step thickness and rotation angle must be adjusted to compensate for the unequal reactive discontinuities. The optimum thickness for each segment may vary from $\lambda_g/4$, and the rotation angle may not be consistent, causing the angular rotation from the input waveguide to the first step to vary from the subsequent steps.

The maximum achievable bandwidth of a single-step twist is frequently limited by the apparition of resonances that are explained by trapped modes inside the twist cavity. A trapped mode occurs when one of the modes involved in the field rotation is confined to a specific region within the twist cavity and cannot propagate beyond it. The mode confinement is due to the discontinuity generated by the introduction of the twist. An alternative to increase the bandwidth is the implementation of a multi-step twist.

2.2.4 – Design and Performance of Wideband 90° Twists

The single-step twist proposed in [Paper A] and the 2-step twist described in [Paper B] are displayed in Fig. 2.2. Both designs are based on modified ridge waveguide sections and incorporate rounded features that ease the fabrication through direct milling without compromising the overall bandwidth and performance.

The single-step twist was aimed to cover the frequency range of 140 to 220 GHz, i.e. 44% fractional bandwidth. Through a careful study of the single-step twist, a second design with 2 sections was proposed for a targeted frequency range of 210-375 GHz, i.e. 56% fractional bandwidth. The device remains highly compact since both steps are fabricated on the same washer.

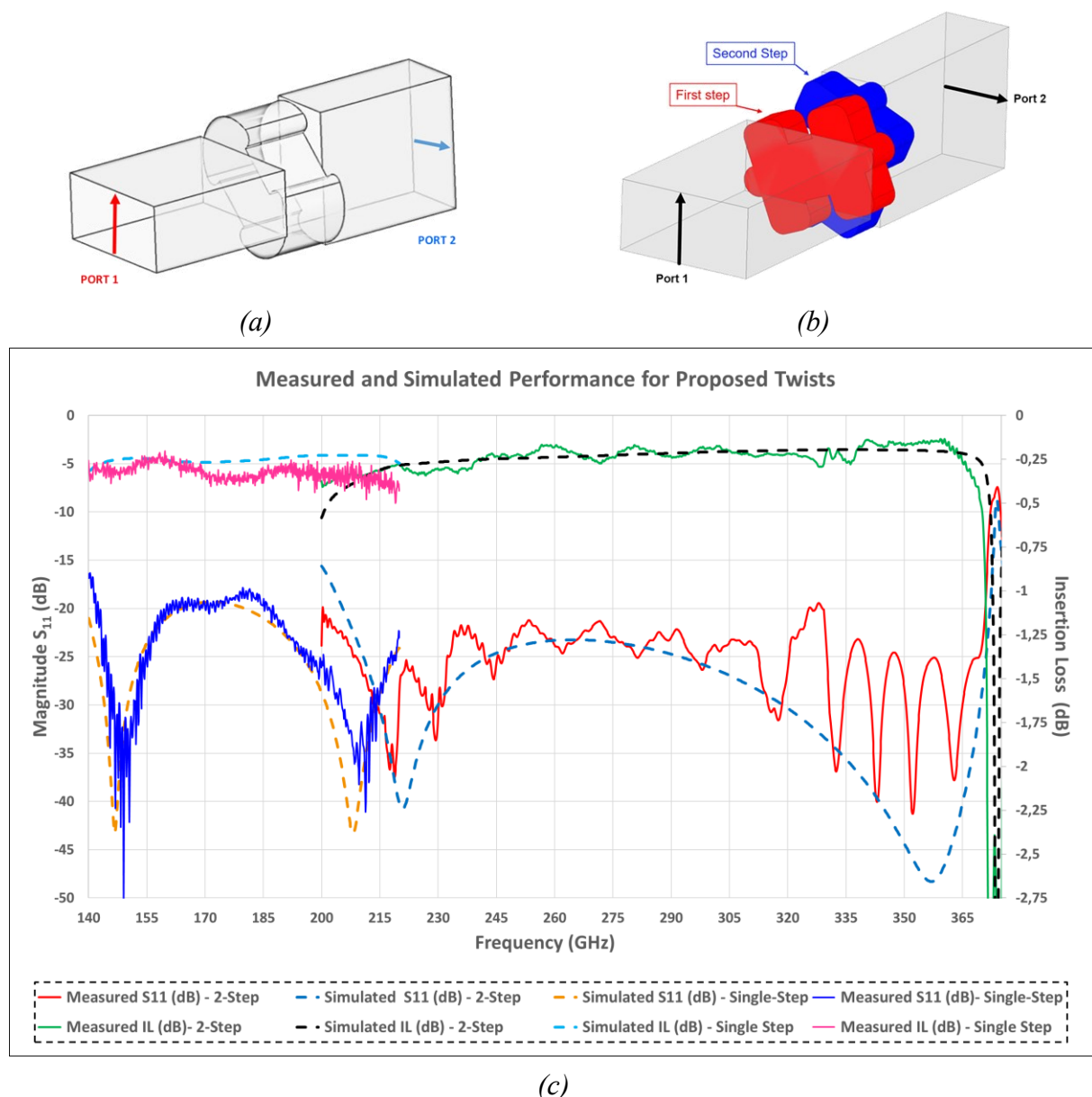


Fig. 2.2. Compact wideband waveguide twists. Note that dashed lines indicate simulated performance and continuous lines depict measurements results. (a) Layout for the single-step twist described in [Paper A] (b) Layout for the 2-step twist presented in [Paper B] (c) Measured and simulated performance for proposed waveguide twists.

The second design introduces “lobes” with a circular shape that enhances the device bandwidth at the lower edge of the band. This is explained by the increment in the effective width of the ridge structure and, hence, a better matching at the lower edge of the band. It is important to note that due to inaccuracies in the fabrication, the intended bandwidth was shifted to 205-365 GHz. The simulated and measured performance of both designed twists is depicted in Fig. 2.2.

2.2.5 – Comparative Analysis with Existing Designs

Table 2.1 shows a comparative analysis of 90° waveguide twists. From the table, it is seen the outstanding performance of the designs in references [40] and [55]. However, their compactness is limited due to fabrication into a split block. The designs in [49] and [50] include several sharp corners, which complicates production. Notably, the design in [50] achieves high-frequency operation (500-700 GHz) with a 20 dB return loss through direct milling. In contrast, reference [49] uses micromachining with the LIGA Process to accurately produce features in the 600-750 GHz range. Furthermore, [52] employs an alternate micromachining approach incorporating deep silicon etching (DRIE) and metallization, resulting in a progressive twist with an excellent insertion loss of 0.2 dB between 220 and 325 GHz. In [53], 3D printing is employed to create continuous and single-step twists. While this developing technology has yet to equal the performance of existing fabrication methods, its rapid development promises to open up new design opportunities in the future.

From the table, it is also seen that the twists from [Paper A] and [Paper B] stand out due to their exceptional compactness and superior performance in both Reflection Loss (RL) and Insertion Loss (IL). The single-step twist in [Paper A] achieves the full standard waveguide

Table 2.1 - State of the art comparison of 90° Twists							
Ref	Frequency [GHz]	FBW [%]	Length [λ_g]	IL [dB]	RL [dB]	Fabrication	Type
[6]	140-220	44%	1.8	~0.2	30	Electroforming	Continuous
[50]	220-320	37%	? 4	0.5	~20	Milling	Progressive
	500-700	33%	NR	2.5	20		
[42]	75-110	37%	1	0.11	25	Milling	Multistep
[49]	600-750	22%	0.43	0.3	20	Micromachining-UV-LIGA Process	Single-step
[55]	220-330	40%	8.75	0.6	20	Milling	Single-step integrated in split block
[54]	75-110	40%	0.42	~0.2	20	Milling	Single-step
	170-260	42%	0.33	~1	15		
[40]	220-330	40%	18.14	1	25	Milling	Progressive
[53]	110-170	43%	0.46	2	~15	3D Printing and PVD Metallization	Continuous
			0.35	2	~10		Single-step
[52]	220-325	38.5%	0.7	0.2	20	Micromachining - DRIE Silicon and Metallization	Progressive
[Paper A]	140-220	44%	0.3	0.4	~20	Milling	Single-step
[Paper B]	205-365	56%	0.3	0.3	~20	Milling	Double-step

IL: Insertion Loss RL: Reflection Loss λ_g : guided wavelength NR:Not Reported

bandwidth of WR-5.1 while also combining outstanding reflection and insertion loss with a compact design, as indicated by its total length in λ_g . In contrast, the two-step twist from **[Paper B]** outperforms the former in fractional bandwidth and insertion loss while maintaining comparable levels of reflection loss and compactness. Furthermore, both designs were optimized for a well-established and precise manufacturing technique, i.e. direct milling.

2.3 – Novel Waveguide 3dB Power Divider with Matched Ports

2.3.1 – Overview of Power Dividers

Waveguide power dividers are essential components in a wide range of applications, especially in high-power systems that combine numerous power amplifiers. In radioastronomy, these components are critical in S2B mixers within receivers, equally splitting the Local Oscillator (LO) over the two DSB mixers. In particular, most ALMA receivers make use of simple three-port waveguide structures such as the one shown in Fig. 2.1c [6]. These power dividers provide adequate input matching with reasonable phase and amplitude imbalances. Nonetheless, they suffer from poor isolation and output matching. In principle, it is impossible to exceed -6 dB in these respects, since microwave theory states that no tri-port network can be lossless, reciprocal, and matched at all ports at the same time.

Various studies have investigated classical waveguide power splitter designs that incorporate septums to improve input matching. In [56] and [57], output power is delivered to a substrate via E-probes, whereas [58] and [59] achieve power splitting in a substrate-based structure. The intrinsic absence of isolation in these systems means that reflections from one port negatively affect the other [31]. In theory, this limitation might be solved by adding a fourth port to absorb reflected energy, improving isolation and output matching, as the limits of a three-port network do not apply to a four-port network. This approach has been the subject of various investigations in recent decades. A pioneering work in [60] incorporates a resistive material through a slot, which is feasible at lower frequencies but unsuitable at millimeter-wave frequencies due to the structure dimensions becoming too small for accurate fabrication. Further developments include the addition of a resistive material to the septum of the waveguide divider at the Ka-band [61], which improves isolation and output matching. An alternative technique described in [62] uses a ceramic substrate loaded with thin film resistors. However, these strategies result in additional insertion losses due to power dissipation in the resistive material. In [63], a coaxial fourth port is placed between the ports of a Y-junction waveguide power divider, resulting in an effective fourth port that can be matched for improved performance. This concept is further developed in [64] and [65], where an E-probe is placed at the junction of a T-junction power divider. Notably, in [64], a grounded lumped resistor is used as a matched load, but this solution is less effective at millimeter wavelengths due to the significant parasitic inductance and the practicality of discrete/lumped surface-mounted device load resistors at these frequencies.

[Paper C] describes a compact waveguide power divider optimized for millimeter-wave and THz applications. This unique design combines waveguide structures with substrate-based features that significantly enhance output port isolation and matching.

2.3.2 – Design and Performance of Waveguide Power Divider

The power divider described in [Paper C] employs a waveguide T-junction structure combined with a chip based on microstrip technology. This chip makes use of a wideband E-probe that is patterned on the chip to absorb and dissipate reflected signals from the output ports. The chip is placed in a substrate channel located in the waveguide junction. The energy coupled by the E-probe is absorbed by a floating resistive load made of a Titanium-Nitride (Ti-N) mixture chosen for its resistive properties and compatibility with thin-film technology. Fig. 2.3 shows the proposed design.

The fabricated device was tested using a vector network analyzer (VNA) with WR-5 frequency extenders that covered the 150-220 GHz range. The experimental verification was consistent with the simulation results. As shown in Fig 2.4, the measurements revealed a return loss of 20 dB at both the input and output ports, as well as an isolation better than 16 dB between the output ports. The excess insertion loss is limited to 0.3 dB, with amplitude and phase imbalances of only 0.15 dB and close to 0° . Note that the design greatly improves port isolation and matching when compared to commonly used traditional T-junction waveguide dividers. The isolation between the output ports improved from 6 dB to 16 dB, representing a 10 dB improvement with respect to traditional designs. Simultaneously, the return loss at the output ports has improved by at least 14 dB, from 6 dB to 20 dB. Furthermore, the proposed power divider achieved a fractional bandwidth of 38%.

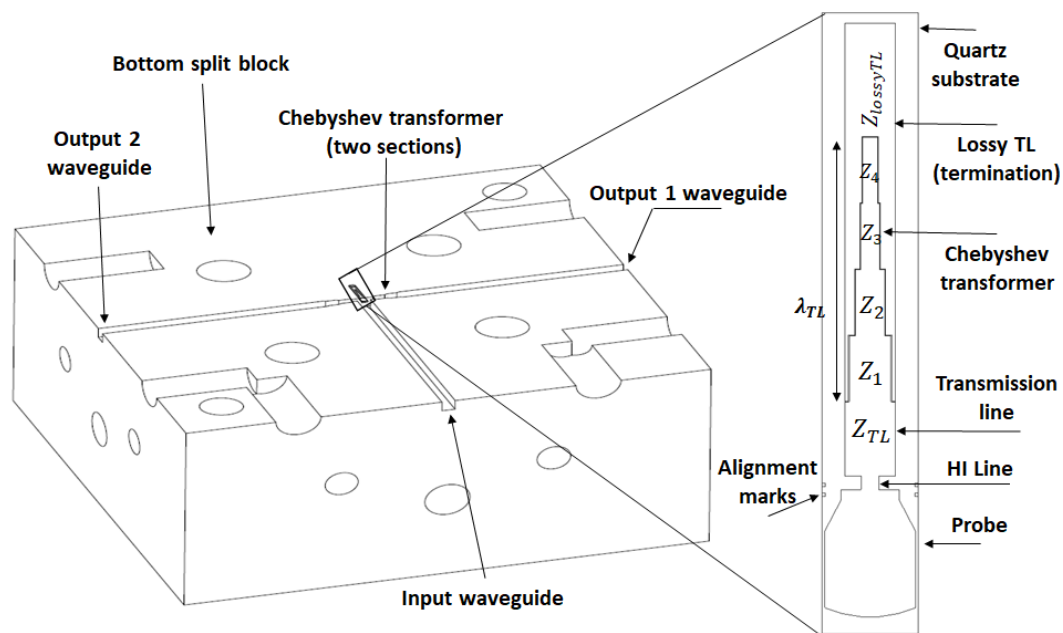


Fig.2.3. Power divider presented in [Paper C]. Detailed 3D drawing of the bottom waveguide split block and the overall chip layout.

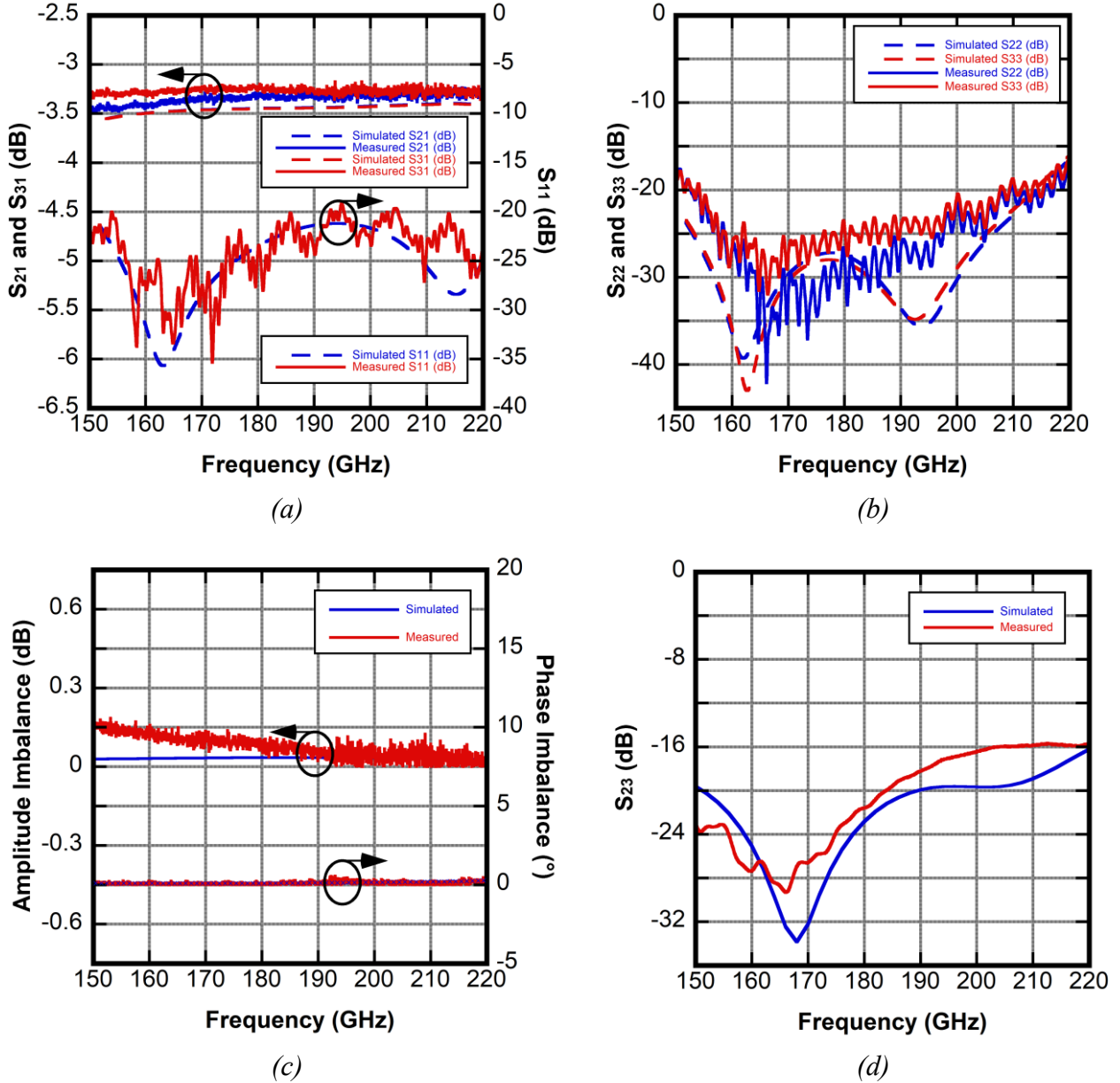


Fig.2.4. Simulation and Measurement results for Waveguide Power Divider proposed in [Paper C]. (a) insertion loss and input return loss, (b) output return loss, (c) amplitude and phase imbalance, and (d) isolation of the power divider.

2.3.3 – State-of-the-Art Comparison

Table 2.2 show a comparative analysis with the state-of-the-art equal slit power dividers, detailing the principle of operation and their measured results. From the table, it is clearly seen that few designs are developed for frequencies above 50 GHz. For instance, the device presented in [56] implements a classical waveguide power divider employing a novel double probe. In [66], a similar concept to the proposed structure in [Paper C] is implemented but with a metamaterial structure based on Spoof Surface Plasmon Polaritons (SSPPs) partnered on the chip. It achieves good isolation and output return loss but only over a limited fractional bandwidth of 18%. On the other hand, the design presented in [67] implements a combination

of multiple design strategies, with a partial septum, an inductive iris, and a piece of absorber, with limited performance. It is important to note the device proposed in [63] which is specifically tailored for ALMA receivers. This device introduces a coaxial port in the waveguide junctions that are connected to a matched load. Nonetheless, the performance is noteworthy, the use of commercial coaxial load might introduce variability in the performance and difficulties to scale the design at higher frequencies. From the comparative analysis, it is seen that the device described in **[Paper C]** stands out for its wideband performance, its novel implementation, and the higher frequency of operation, making the device a very practical component for millimeter-wave and THz systems, in particular, radio-astronomy receivers.

Table 2.2 - Comparison With State-Of-The-Art Equal Split Power Divider									
Ref	FBW [%]	Fc [GHz]	IL [dB]	RL [dB]		I [dB]	Imbalance		Comment
				In	Out		Amp [dB]	Phase [°]	
[56]	30	100	0.3	NR	6	6	0.3	~0	E- Probes and substrates are used for power division.
[58]	4.4	93	0.5	15	6	6	0.12	1.38	The division is achieved through a Substrate Integrated Waveguide chip.
[61]	23	34	0.2	20	20	20	NR	NR	A Resistive Film is introduced in the Septum position.
[62]	18	55	0.4	16	13	20	0.19	1.4	Ceramic Substrate Loaded with Thin Film Resistors introduce in the Septum position.
[64]	20	30	0.2	17	17	20	0.06	NR	E- Probes and grounded lumped resistor employed as matched load.
[63]	38	92.5	0.2	19	14	14	NR	NR	Added coaxial fourth port in waveguide junction. This coaxial is connected to coaxial matched load.
[66]	18	215	0.3	20	15	15	NR	NR	E probe and Spoof surface plasmon polaritons (SSPPs) structure.
[67]	28	87.5	~0.25	15	10	10	0.15	7.5	Waveguide T-Junction combine with Septum, Iris and absorber.
[Paper C]	38	185	0.3	~20	~20	16	0.15	~0	Waveguide T-junction structure combined with a chip based on microstrip technology.

FBW: Fractional Bandwidth **Fc:** Central Frequency **IL:** Insertion Loss **RL:** Reflection Loss **I :** Isolation **NR:**Not Reported

Chapter 3

Waveguide to Microstrip Transition for Prospective 2SB SIS Mixers

3.1 – A Review of Waveguide-to-Substrate Transitions

Thin-film technology is the main pillar for mixer fabrication in radio astronomy receivers, thus, waveguide-to-substrate transitions play a crucial role in the receiver performance. The main requirements for the waveguide to substrate transitions are a low insertion loss accompanied by proper impedance matching. In addition, a simple mounting process and the associated mounting tolerances are also essential requirements.

3.1.1 – Probes

Probes have been extensively employed as waveguide-to-substrate transitions. This enormous popularity responds to their ease of fabrication and versatility. The primary classification of probes differentiates between H and E types [31]. E-probes are designed to interact with the electric component of an electromagnetic field, whereas H-probes are intended to interface with the magnetic component. The literature on H-probes in the mm and sub-mm ranges is sparse, reflecting their limited applications at these frequencies [68]. Although H-probes can be used as in-line waveguide-to-substrate transitions with no backshorts or tuning

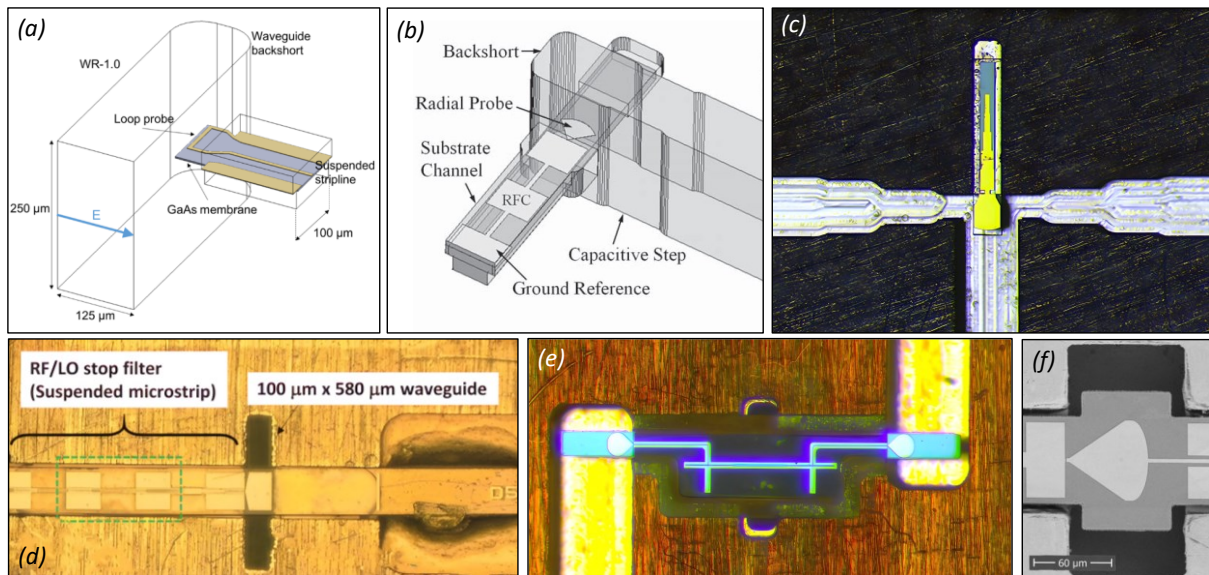


Fig. 3.1. Examples of probes waveguide to substrate transition. (a) H-Probe designed for frequency range 750-1100 GHz [68]. (b) 90° Radial “one-side” probe with tuning capacitive step in the input waveguide. Design for SIS mixer operating in the frequency range 275-425 GHz. [70] (c) E-Probe employed in [Paper C] covering the frequency range 150-220 GHz. (d) 275-500 GHz “double-side” E-Probe for back-short configuration with waveguide of reduced height for wideband operation. Employed in SIS Mixer in [35]. (e) Single-side E-Probe for 295-375 GHz employed in [Paper E] for back-to-back measurements (f) Radial E-Probe for HEB mixer 1-1.5 THz [8].

elements [69], they have a high impedance when suspended striplines are employed as final transmission lines [68]. Furthermore, these probes do not have the same broad bandwidth performance as E-probes in the mm and sub-mm ranges [69]. As a result, E-probes are commonly used in waveguide-to-substrate transitions for THz applications. In radioastronomy, for instance, E-probe mixers are widely employed for a variety of frequencies and detector types, as shown in Fig. 3.1*b, c, d, e* and *f*. 'One-side' E-probes, especially radial probes, are widely used in this field [70], [8], [38]. These probes, which partially extend their electrically conducting structures over the waveguide, have been found to have a low impedance. This is explained by the contributions from the waveguide modes, which add up in series, and only the propagating fundamental mode couples to the resistive part of the input impedance, resulting in the lower characteristic impedance [71], [72]. In contrast, 'double-side' E-probes have a parallel addition of evanescent waveguide modes, which complicates and increases the real component of the input impedance [72]. In such cases, the waveguide height is frequently reduced to accommodate a lower impedance at the expense of higher waveguide losses. Therefore, "one-side" probes are generally employed for SIS mixer designs since the RF impedance of the superconducting tunnel junction is low. Fig. 3.1*b* and 3.1*d* show examples of "one-side" and "double-side" probes respectively. Radial probes are preferred over other E-probe designs because of their wide impedance range (10 to 60 Ohms), which varies depending on substrate and radius specifications [73]. Achieving pure real impedances needs fine-tuning to cancel the probe's impedance imaginary portion, which is significantly dependent on the probe's position relative to a waveguide backshort and the alignment to the chip channel. Traditional designs position the backshort at a quarter guided wavelength ($\lambda_g/4$), limiting the maximum bandwidth of E-probes [73]. Some designs offer in-line E-probes that do not use traditional backshorts and instead compensate with waveguide elements such as irises and T-junctions [19]. In recent years, significant progress has been made toward wideband probes with fractional bandwidth reaching 50% [70] where a capacitive step is introduced in the input waveguide to increase the fractional bandwidth. Although this approach dramatically improves the probe's bandwidth, the positioning of the probe with respect to the waveguide backshort remains a critical parameter for the performance. Therefore, it becomes clear that there is a need for an alternative waveguide to substrate transition for the next generation of radio astronomy receivers.

3.1.2 – Finlines

Since finlines structures were first proposed in [76], they have been used for a wide variety of applications, from microwave to the sub-mm wave range [77-80]. Finlines are waveguide-to-substrate transitions constituted by a pair of conductive fins over a dielectric substrate. It is important to remark that finline structures are meant for split block technology. In general, the conductive fins are positioned where the E-field magnitude is maximum for the fundamental TE₁₀ rectangular waveguide mode, i.e., at the center of the waveguide broader wall "wa", as shown in Fig 3.2*a*. The positioning inside the rectangular waveguide gives finlines a considerable advantage with respect to other waveguide-to-substrate transitions, i.e. their tolerance to mounting and more straightforward block fabrication since a backshort is not needed.

Among the different existing configurations, the unilateral, antipodal, and bilateral finlines are the most widely used. The unilateral layout is the simplest and probably the best suited for high-frequency applications since both metallizations are located on the same side of the dielectric slab, as illustrated by Fig. 3.2 . This configuration eliminates the problems related to the fins' alignment but increases the overall impedance of the line since a large part of the electromagnetic field propagates outside the dielectric. The unilateral configuration has been applied for mixer design in [85] and [86]. In these designs, different techniques were employed to mitigate the main problem associated with finlines, i.e. the impedance matching between the waveguide and the substrate. The poor impedance matching degrades the performance of the transition and limits its operating bandwidth. In Fig. 3.3b and d, unilateral finline mixers are presented. Note that different solutions for improving the matching are presented. These solutions are based on impedance transformers [82] patterned on the substrate aiming to gradually load the waveguide and minimize the mismatch. Although these techniques partially solved the matching problem, they extend the substrate inside the waveguide, which increases the dielectric losses of the transition.

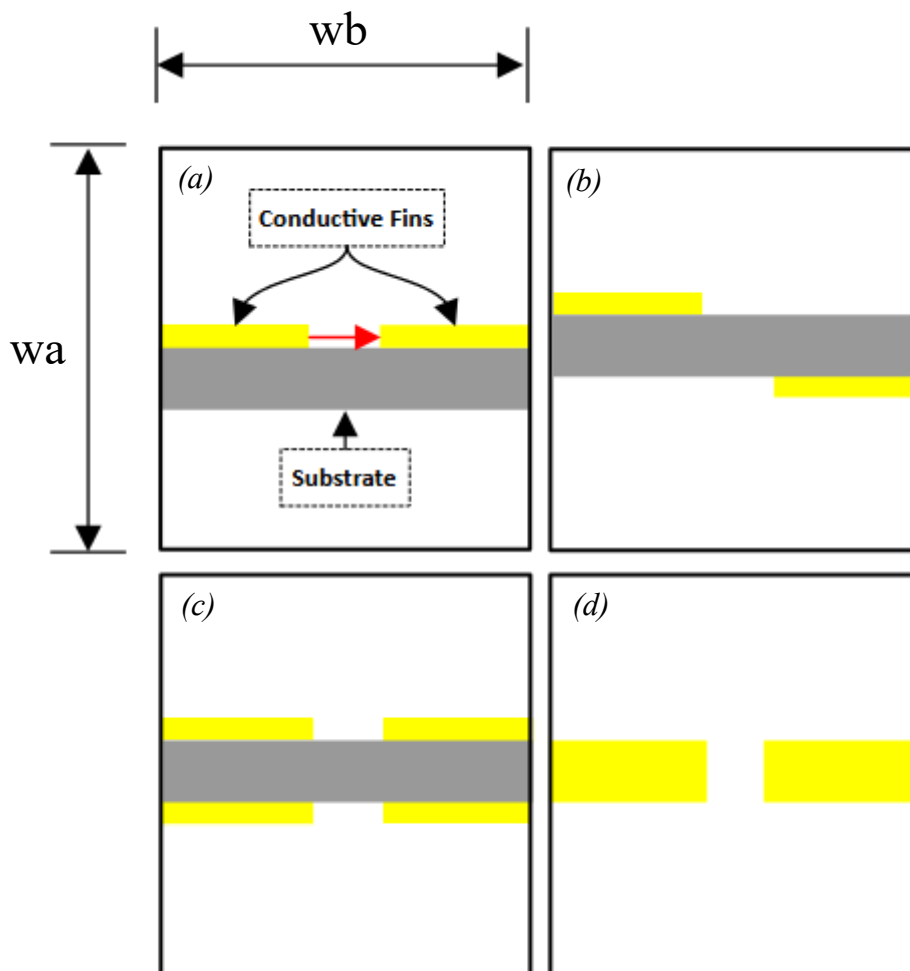


Fig. 3.2. Cross section of four commonly used finline configurations. Dimensions a and b of a standard rectangular waveguide are indicated as w_a and w_b . (a) In the unilateral finline configuration the fins are located on only one side of the substrate. The red arrow illustrates the electric field excitation of the fin-gap. (b) Antipodal configuration. (c) Bilateral. (d) Metallic Finline.

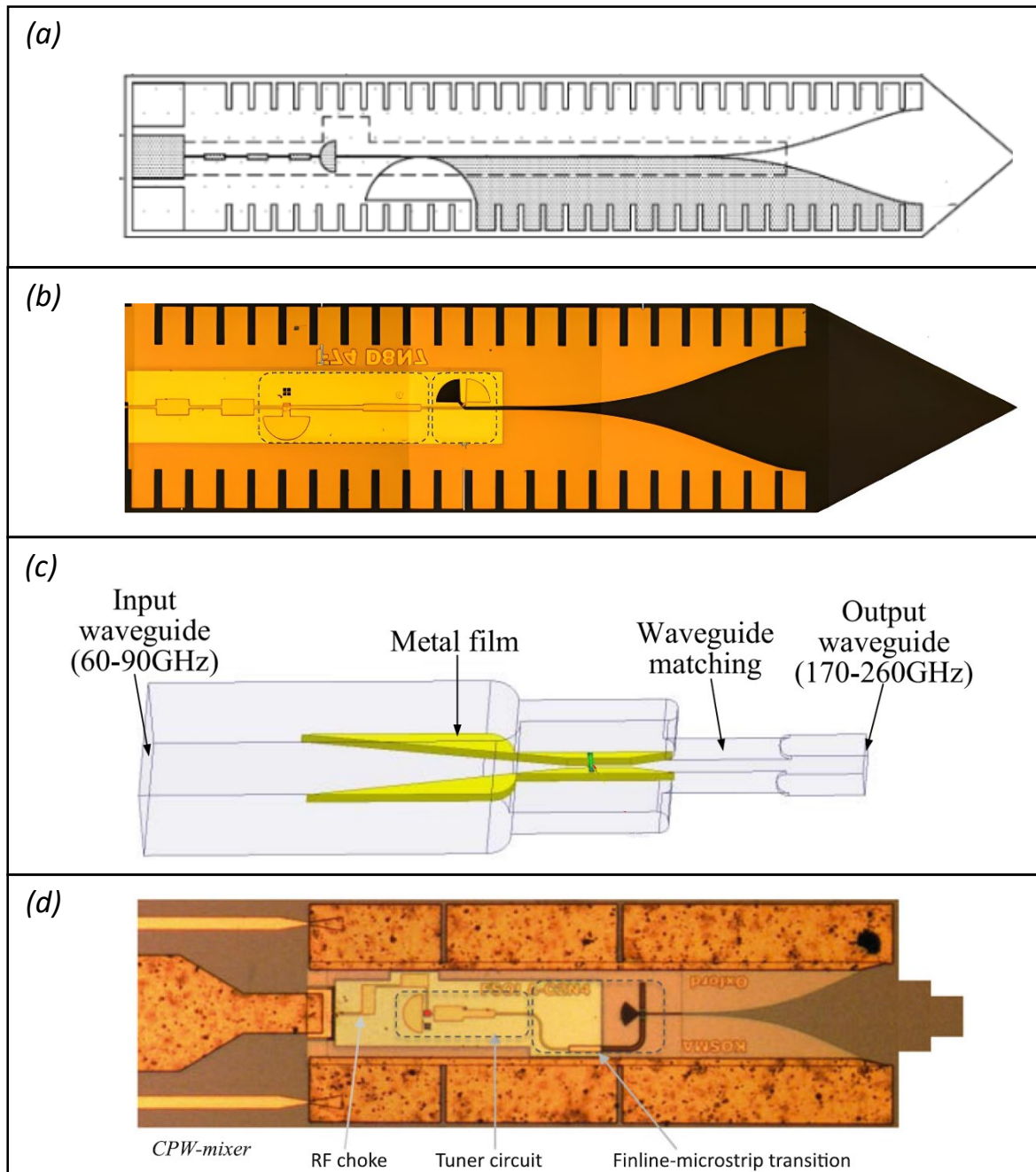


Fig. 3.3. Examples of finline devices (a) Antipodal SIS finline mixer designed for 350 GHz operation. [81] (b) SIS mixer fabricated on $60\ \mu\text{m}$ quartz substrate. The finline transition makes use of a triangular notch in the substrate to improve matching. In addition, serration chokes are employed to guard against the propagation of substrate mode. [83] (c) Metallic finline employed for a Schottky frequency tripler [84] (d) SIS mixer fabricated over $15\ \mu\text{m}$ Si substrate. Note that a multi-stage silicon matching notch is employed. Since the Si substrate is extremely thin, no serration is needed to preclude substrate modes from propagating. [83].

In antipodal finlines, the fins are separated by the substrate, as shown in Fig 3.2. This type of finline achieves lower impedance levels since the field is concentrated inside the substrate. Moreover, the antipodal layout allows a direct transition to microstrip. This advantage has been explored in [81], where an antipodal finline mixer was developed as illustrated in Fig. 3.3a. However, the performance of the antipodal configurations is sensitive to the alignment between the fins, especially at high frequencies where a few μm wide fin-gap is frequently employed. This problem is common also for bilateral finline configuration since it presents a pair of fins on both sides of the dielectric slab, as depicted in Fig. 3.2c. Furthermore, the bilateral arrangement generally presents significant losses due to higher field concentration inside the dielectric [82]. Within the various finline configurations, there is a variant that does not include a dielectric slab, referred to as metallic finlines. This design employs free-hanging thin metallic films and is distinguished by the absence of a dielectric substrate, resulting in a higher characteristic impedance than other finline designs. This characteristic makes matching impedance with rectangular waveguides easier. However, metallic finlines are mostly used in low-frequency applications. The reason for this is the complex process of fabricating and then aligning each fin separately within the waveguide. Fig. 3.3c depicts a notable implementation of all-metal fins in the 170-260 GHz band, as detailed in reference [84]. In this design, a metal film is shaped into a finline to make a frequency tripler based on Schottky diodes. Each metallic fin is separately mounted and the diodes are then attached to the structure using conducting glue. While this approach is feasible, it has limitations in more complex applications where fin-gap precision and alignment relative to the fin gap are critical for performance.

An alternative solution is explored in this thesis [**Paper D**], where a new type of finline, the Substrateless finline, is presented. In this finline configuration, the substrate confined by the fins is removed to improve the matching and reduce the dielectric losses.

3.2 – Advancements in Finline Technology for THz Applications

3.2.1 – Substrateless Finline

The substrateless finline described in [**Paper D**] is a novel approach to unilateral finline design, with the substrate completely removed between the conductive fins, as illustrated in Fig. 3.4. However, the substrate beneath the fins is preserved. As mentioned in Section 3.1.2, this design focuses on two main challenges related to finline transitions: dielectric losses in the substrate and wideband impedance matching. The gradual insertion of the dielectric slab into the substrateless finline eases the matching of the structure with the waveguide, dramatically improving the bandwidth of the transition. This makes substrateless finlines an attractive choice for wideband design applications. The waveguide-to-substrate transition is built on a thin silicon substrate coated with a superconducting niobium layer. An additional gold layer is used to facilitate grounding and mounting in a split block. The design was simulated, fabricated, and tested at cryogenic temperatures, as described in [**Paper D**]. The simulation showed a fractional bandwidth of 55% with a return loss reaching 15 dB for a single transition. The experimental results at cryogenic temperatures confirmed these findings, with an the measured insertion loss of 0.5 dB for most of the band for a single transition. The demonstrated performance demonstrates the suitability for wideband mixer designs and other applications requiring low losses and large fractional bandwidth. Fig. 3.4 depicts the fabricated structures according to the technique specified in [**Paper D**], while Fig. 3.5 provides an overview of the experimental results.

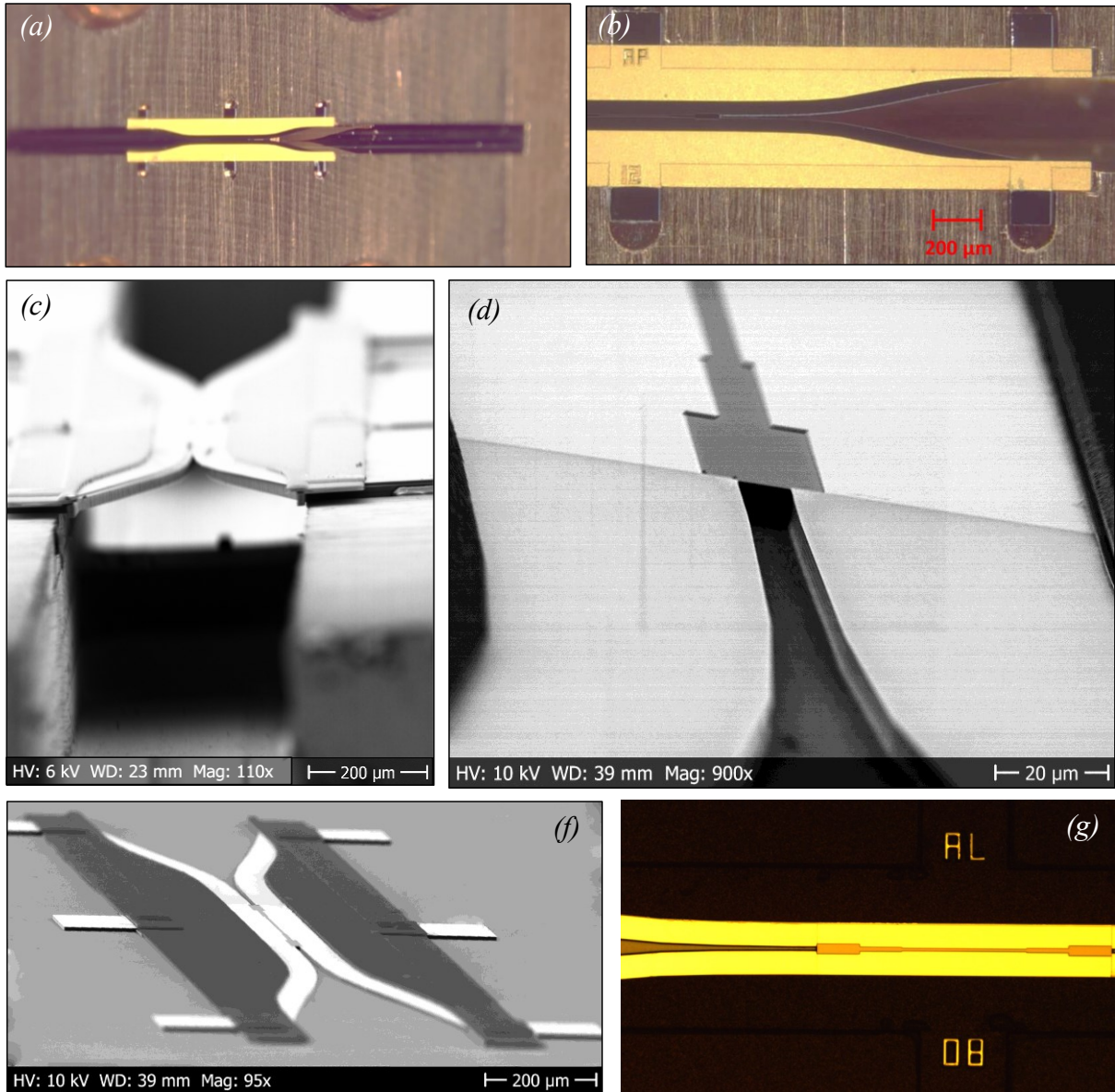


Fig. 3.4. Fabricated waveguide to substrate transition. (a) Finline mounted in the tellurium-copper waveguide block with dimension $800 \times 400 \mu\text{m}$ (b) Magnified image of the mounted finline. (c) Scanning electron microscope (SEM) image of the fabricated back-to-back device mounted into the split-block. (d) SEM picture of the finline structure after etching the first $5 \mu\text{m}$ of the Si device layer. The verticality of the side walls could be appreciated. (e) SEM picture of the device before release. (f) Detail of the central slotline transformer in a back-to-back configuration.

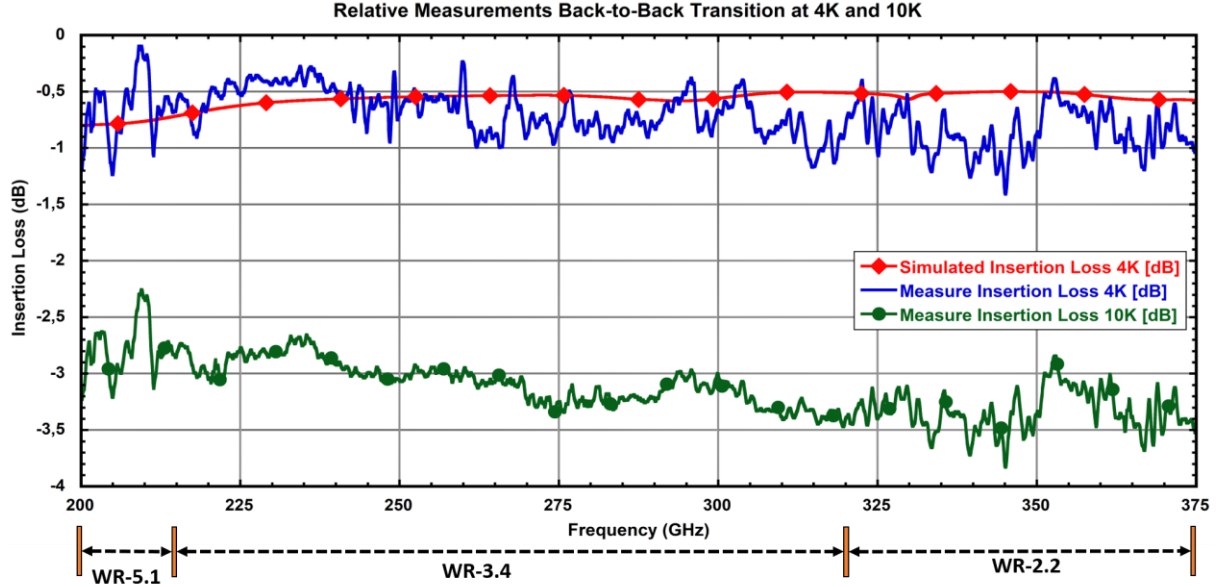


Fig. 3.5. Measured Insertion loss of the proposed finline in [Paper D] at the physical temperature of 4K and 10K. It can be seen how the losses above the transition temperature for Nb increase considerably. The simulation at 4K is shown in red. Three different VNA extension modules were used in the experiment to be able to cover the frequency range of 200-375GHz.

3.2.2 –Analysis of State-of-the-Art Waveguide to Substrate Transitions

Table 3.1 depicts the most recent advances in waveguide-to-substrate transitions, demonstrating a range of techniques to achieve large fractional bandwidths in millimeter and submillimeter wavelengths. These designs predominantly employ E-probes in a variety of configurations. One notable example is found in the design presented in [73], which proposed a cryogenic transition with a significant fractional bandwidth of 45.7%, yet its insertion loss is not specified. This design, along with those suggested in [87], [89], and [90], has been verified with a scaled model at lower frequencies and ambient temperature. While this method supports the design concept, it does not fully capture the transition's actual performance. Furthermore, thermal contraction and cooling-induced stress, as well as mounting and positioning sensitivity, can only be empirically validated in the desired frequency band at cryogenic temperature.

Another novel design in [7] employs radial E-probes in a split-block layout for a frequency multiplier. Despite the low insertion loss and significant fractional bandwidth of 44.4%, these findings are primarily based on electromagnetic models and estimation from direct measurements. Furthermore, Table 3.1 presents novel designs that include ridge waveguides in combination with E-probes [94], and Substrate Integrated Waveguides (SIW) [93]. The ridge waveguide, in particular, aids in field concentration and impedance matching, but its precise fabrication presents challenges at higher frequencies, as indicated by differences between intended and measured fractional bandwidths in these works.

Another noteworthy design is the bifurcated probe in [97] which exhibits remarkable performance with low insertion loss throughout a wide fractional bandwidth, as confirmed in a back-to-back configuration at room temperature. Moreover, the device in [96], that employs a bow-tie probe with a bed of nails has a significant fractional bandwidth. Nonetheless, it has

only been tested in simulation and is not yet verified by measurement. Emerging trends, as illustrated in [75] and [74], include the use of E-probes as inline transitions with additional waveguide features to compensate for the imaginary impedance of the probe and increase bandwidth. These transitions attained measured bandwidths of up to 42%. Finline transitions, while uncommon at these frequencies, are demonstrated in [83] and [90]. In particular, the work in [90] was verified employing a scaled model, demonstrating a measured fractional bandwidth of 38.2% and an insertion loss of 0.5 dB.

In Table 3.1, the substrate materials of the waveguide-to-substrate transitions are listed. It is seen that quartz is the preferred substrate material due to its low loss and dielectric constant ($\epsilon_r \sim 3.8$). This limits the excitation of unwanted electromagnetic modes and allows thicker substrates with mechanical strength for easy handling and mounting. Although Si presents a high dielectric constant, its mature processing technology and low dielectric loss tangent at cryogenic temperatures make it an attractive option [7], [89], [88], **[Paper E]**. Notably, high-dielectric-constant materials such as InP and GaAs have lately been investigated as substrate material for waveguide-to-substrate transitions, driven by the development of mm and sub-mm HEMT amplifiers employing MMIC methods based on these materials [92], [95], [68].

The transition in **[Paper E]** stands out, with a remarkable bandwidth of $\sim 56\%$ and low insertion losses. This design, to the author's knowledge, presents the highest fractional bandwidth among all analyzed and the only design tested directly at cryogenic temperatures, has the potential for a wide range of applications, particularly in broadband mixer design for radioastronomy receivers, due to its wide bandwidth, low losses, and simple design and mounting.

Table 3.1 State-of-the-art Waveguide-to-Substrate transitions

Reference	Transition Type	Intended Frequency Band	Intended FBW	Measured FBW @ 15 dB Return Loss	Insertion Loss [dB]	Measurement Method	Substrate Material
87	Radial Probe to microstrip	375-500	28.57%	~31%	0.15	Scale Model Verification - Warm	Quartz
7	Radial Probe to microstrip	140-220	44.4%	44.4%	0.45	Estimation from Cryogenic Measurement	Si - 60 μm
73	Radial Probe to microstrip	270-430	45.7%	45.7%	Not Reported	Scale Model Verification - Warm	Quartz -50 μm
88	Radial Probe to microstrip	700-1100	44.4%	NA	Not Reported	Simulation	Si - 7 μm
89	Dual-dipole antenna to microstrip	580-800	31.8%	31.8%	2	Scale Model Verification - Warm	1 μm thick SiN on top of 200 μm Si
83	Unilateral Finline to slotline	550-750	30.7%	NA	Negligible	Simulation	Si -15 μm
90	Unilateral Finline to slotline	170-265	43.6%	38.2%	0.5	Scale Model Verification - Warm	Quartz - 100 μm
68	H-Probe to Suspended Microstrip	750-1100	37.8%	24.56%	~2	Back to Back Warm Measurement	GaAs - 3 μm
91	E-Probe to Microstrip	110-170	42.8%	NA	0.14	Simulation	Rogers RT/duroid 5880
92	Radial Probe to microstrip	300-350	15.3%	15.3%	~2.5	Back to Back Warm Measurement	InP - 50 μm
93	SIW to microstrip aided by ridge waveguide	75-110	37.8%	14.6%	~0.8	Back to Back Warm Measurement	Alumina
94	E-Probe aided by ridge waveguide	60-90	40%	22%	0.77	Back to Back Warm Measurement	Ceramicsubstrate - 127 μm
95	E-Probe to microstrip	220-325	38.5%	38.5%	~2.5 ~1.25	Back to Back Warm Measurement	GaAs - 50 μm Quartz - 300 μm
96	E-Probe Bow Tie to microstrip	106-180	51.7%	NA	0.97	Simulation	Quartz - 50 μm
97	E-Probe Bifurcated to microstrip	170-260	41.8%	41.8%	~0.42	Back to Back Warm Measurement	Quartz - 50 μm
75	Inline E-Probe with Iris	75-110	37.8%	34.6%	0.4	Back to Back Warm Measurement	RT/Rogers 5880 substrate
74	Inline E-Probe with T-junction	170-260	41.8%	41.8%	0.6	Back to Back Warm Measurement	Quartz -50 μm
Paper E	Unilateral Substrateless Finline	75-110	37.8%	34.6%	~0.5	Back to Back Warm Measurement	Quartz -127 μm
		211-375	55.9%	55.9%	~0.5	Cryogenic Back to Back Insertion Loss Measurement	Si-30 μm

3.3 – Wideband Slotline-to-Microstrip Transition

3.3.1 – Overview of Slotline-to-Microstrip Transitions

Thin-film superconducting microstrips are fully compatible with the fabrication of the trilayer SIS structure [Paper F]. Furthermore, thin-film microstrips can reach impedances below $10\ \Omega$, which is especially suitable for the SIS RF impedance matching circuit. Consequently, most modern SIS mixers rely on thin-film microstrip lines for on-substrate interconnections [38], [35]. On the other hand, finline structures can be easily coupled to slotlines as the main electromagnetic propagation mode is essentially identical. Nevertheless, fabricating slotlines with small characteristic impedance is rather challenging due to the small slot size. Therefore, finline mixers usually employ an additional transition step from slotline to microstrip.

Slotline-to-microstrip transitions are expected to have low insertion loss with sufficient return loss level, and chip area minimization. These requirements are challenging to accomplish due to the inherent impedance difference between slotlines and microstrips[82]. While $40\ \Omega$ slotlines can be fabricated with thin-film technology, lower impedance values are unpractical as the slot dimension decreases to the μm range and below. On the other hand, it is rather difficult to achieve impedance values higher than $20\ \Omega$ with thin-film microstrips, where the dielectric layer thickness is comparable to the strip thickness. Therefore, the matching between slotlines and thin-film microstrips is highly challenging. Through the years, a large number of different solutions have been proposed [98-101].

One of the classical solutions is the cross-junction transition [100], as depicted in Fig. 3.6a. In these junctions, the microstrip is defined on one side of the dielectric, while the slotline is located on the opposite side of it. The transmission lines cross each other at a 90° angle and terminate in $\lambda/4$ stubs. These stubs are open and short circuits for the microstrip and the slotline, respectively. Therefore, the electromagnetic energy is transferred at the intersection from one transmission line into the other through the magnetic field. The energy transfer is maximized when the stubs are exactly $\lambda/4$ long. Hence, the cross-junction transition performance is limited by the stubs bandwidth. Radial stubs are frequently employed since they provide larger fractional bandwidth. However, the radial stubs dramatically increase the chip area together with the equivalent capacitance shown by the circuit at lower frequencies. This becomes especially problematic for SIS mixers where the IF bandwidth depends on the capacitance value.

Double Y baluns emerge as an alternative solution to cross-junction transitions [101], as displayed in Fig. 3.6c. The double Y balun employs short and open terminations for both microstrip and slotlines to optimize energy transfer and improve the overall bandwidth of the transition. Nonetheless, the slotline open termination significantly increases the area on the chip, and it is a potential source of resonances due to energy radiation. Furthermore, the realization of the short circuits in a microstrip makes the design and fabrication rather complex.

The inherent impedance difference between microstrips and slotlines could be overcome with indirect transitions, where an auxiliary transmission line is employed to facilitate the matching [83]. Among the different auxiliary lines, coplanar waveguides (CPW) are the most popular solution due to the wide range of impedances and field compatibility with slotline and microstrip, as illustrated by Fig. 3.6b. Indirect transitions with CPW enhance the bandwidth of microstrip to slotline transitions. Nevertheless, the fabrication of such a transition is rather problematic due to the extra transition steps and the need for an air bridge to suppress parasitic CPW modes.

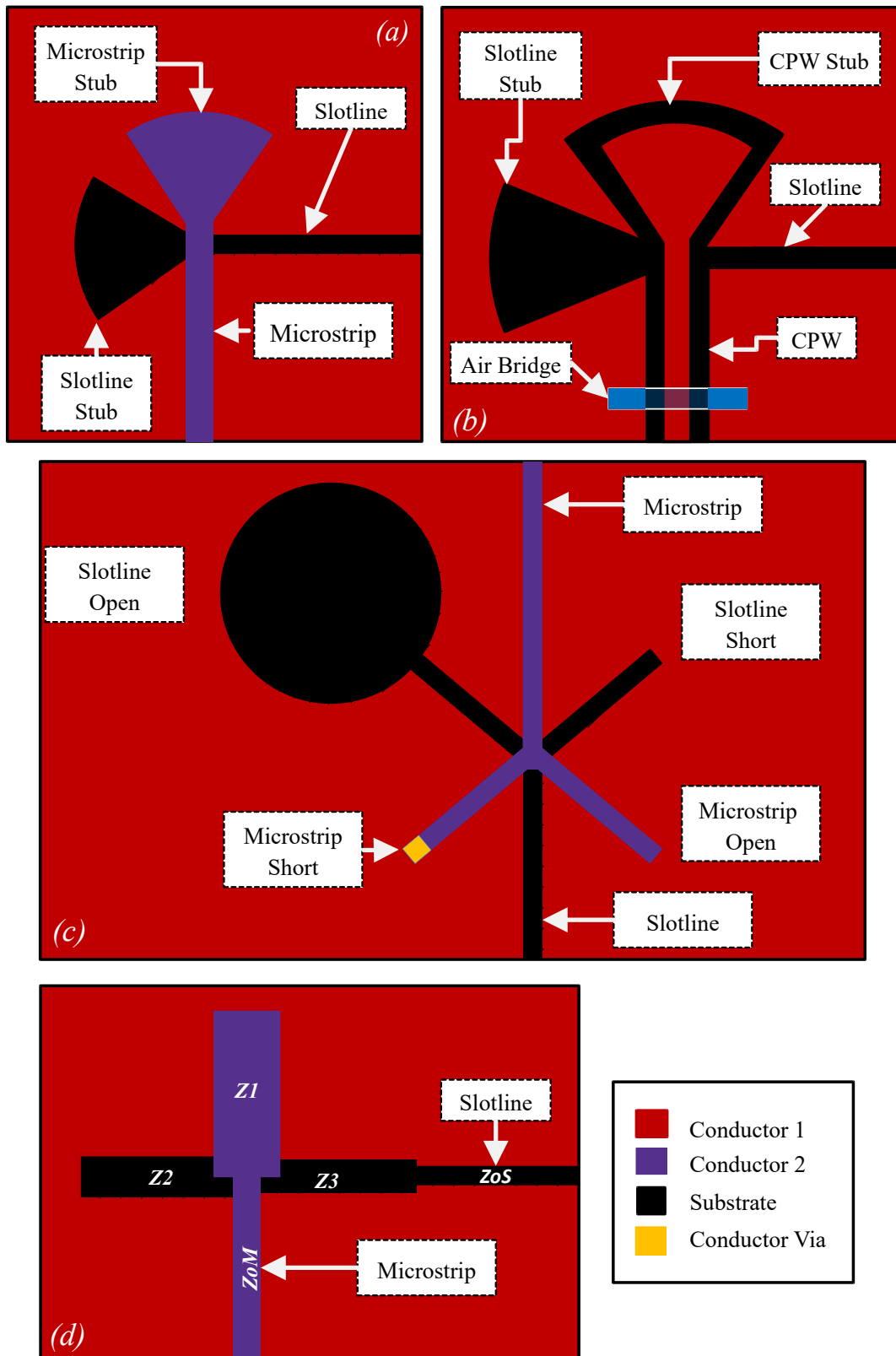


Fig. 3.6. Slotline to microstrip transitions. It is important to note that the dielectric layer located between the conductors is not shown in the images for clarity. (a) Cross-junction transition. (b) Indirect transition with CPW. (c) Double Y balun transition (d) Marchand balun transition.

The Marchand balun transition arises as a promising solution due to its compactness and design flexibility [98]. The Marchand balun structures resemble a cross-junction transition. However, its bandwidth does not rely on $\lambda/4$ stubs, but it combines different impedances to synthesize a particular response. For instance, a third-order Chebyshev passband response could be synthesized for the balun as depicted in Fig. 3.6d. Furthermore, since this balun does not employ radial or circular stubs, the transition is highly compact. These advantages make Marchand baluns an attractive solution for broadband low-loss microstrip to slotline transitions. In [Paper E] a wideband low-loss slotline to microstrip transition is presented.

3.3.2 – Wideband Low-Loss Slotline-to-Microstrip Transition

In [Paper E] a novel slotline-to-microstrip transition is presented for the 210–375 GHz frequency band, based on Marchand baluns which are traditionally used in low-frequency applications [98]. The design, simulation, and cryogenic characterization of the proposed balun are detailed in [Paper E].

To be able to measure the entire bandwidth of the baluns, they were integrated with 2 different E-probes, covering the lower and upper part of the targeted frequency band. Moreover, in order to deembed the losses associated with the E-probes, chips without the transitions were fabricated, featuring only a microstrip connecting the two probes. The experimental cryogenic verification and deembedding revealed an impressively low insertion loss of 0.3 dB across most of the band and a significant 56% fractional bandwidth. Fig. 3.7 depicts pictures of the fabricated transition, the measurement setup, and the measured performance of the devices at 4K.

The proposed slotline-to-microstrip transition is proven to be a promising solution for THz applications due to its outstanding fractional bandwidth, low loss, and compact design. The experimental verification at 4K supports the transition application for wideband mixer design within the 210–375 GHz frequency band.

Integrating substrateless finlines with Marchand baluns is a promising solution for achieving a wideband waveguide-to-microstrip transition. However, this design can be further enhanced by completely removing the dielectric beneath the fins, resulting in purely metallic finlines produced via a micromachining process. These metal micromachined finlines, which are free of any dielectric substrate, present an attractive design approach. In such structures, the chip area is not limited by the excitation of substrate modes and resonances. Furthermore, the all-metal structure has low thermal capacitance and has greater tolerance to stress during cooling processes [102]. Chapter 4 further explores employing a metallic substrate as a technological platform for THz applications and details the design of an SIS mixer employing this metallic substrate platform.

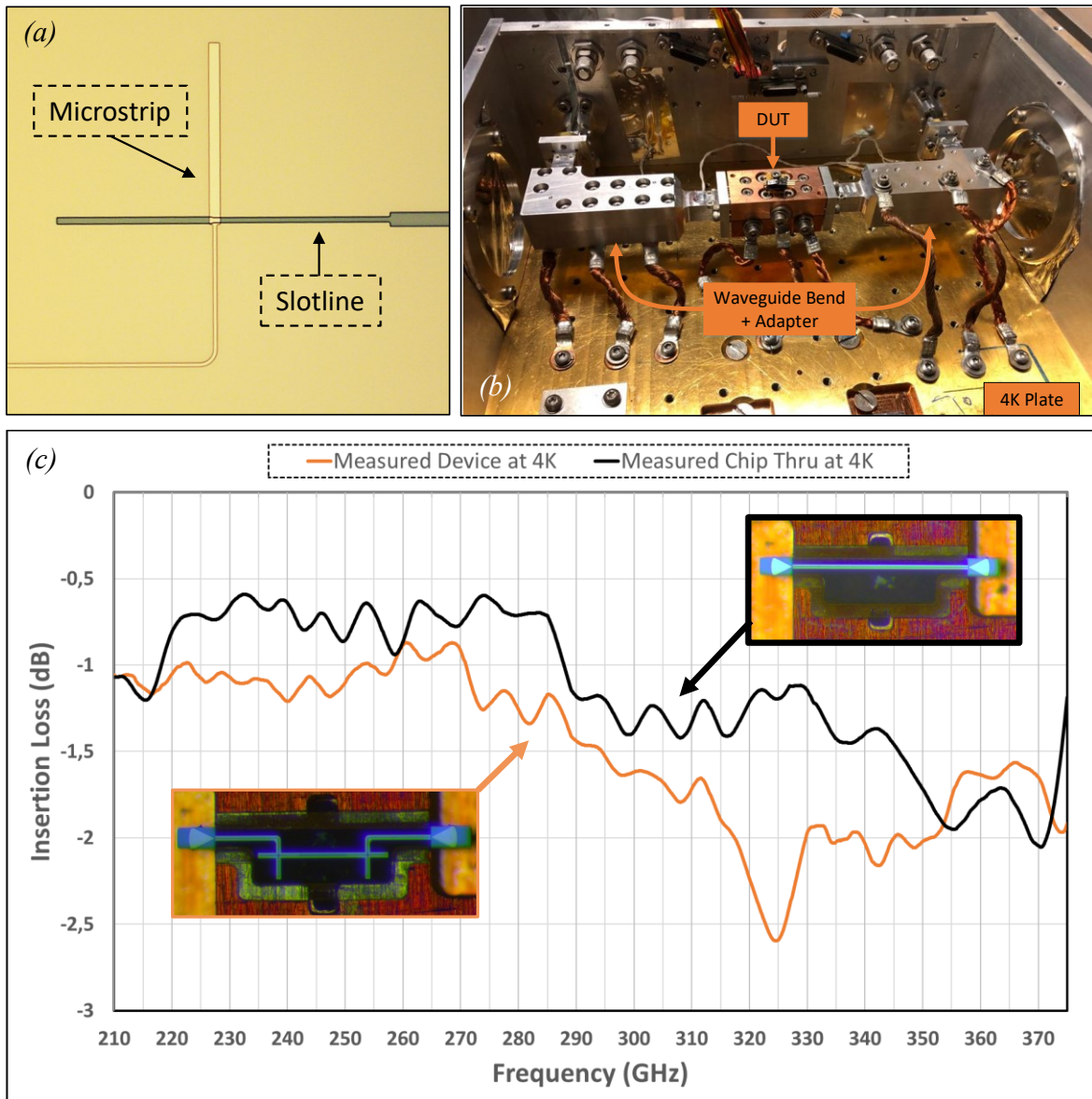


Fig. 3.5. Marchand Balun transition proposed in [Paper E]. (a) A photograph of the fabricated Microstrip to Slotline transition is depicted. (b) Measurement setup inside a closed cycle cryostat. (c) Insertion loss measurements at cryogenic temperatures of the chip with thru connection and the chip with the Marchand balun structure.

Chapter 4

A Novel Ultra Wideband SIS Mixer

4.1 – Modern SIS Mixers

4.1.1 – Fundamentals of SIS Mixer Design

The basis for SIS mixer design was established by Tucker and Feldman in [24] where they described the principles of quantum mixing. The small signal analysis of an SIS mixer is based on the following assumptions: first, only the LO frequency is applied to the junctions and all the higher harmonics are effectively short-circuited by the geometric capacitance of the SIS structure. Therefore, only the signal, the image, and the output IF signal are taken into account in the analysis. Secondly, it is assumed that the IF frequency is much smaller than the LO frequency. These assumptions allow the definition of the small-signal circuit model for 3-ports as shown in Fig. 4.1.

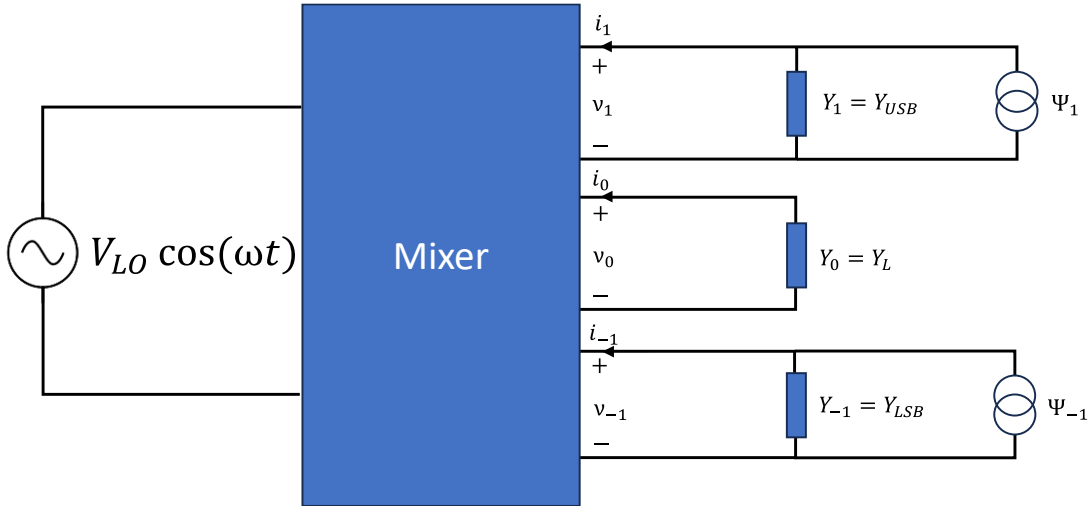


Fig. 4.1. Circuit model for 3 port heterodyne mixer presented in [24]. A sinusoidal LO frequency is applied generating 2 sidebands and an IF output. The RF signal applied to each sideband is represented by the current sources Ψ_1 and Ψ_{-1} for the USB and LSB, respectively.

This circuit model defines the embedded admittances for each port: Y_1 is the admittance shown by the matching circuit to the upper sideband, while Y_{-1} is the equivalent for the lower sideband. In a DSB mixer, those admittance values are identical. Meanwhile, the IF load admittance is represented by Y_0 . Employing the same notation the relation between currents i_m and voltages v_m is defined by:

$$i_m = \sum_{m'} Y_{mm'} v_{m'} \quad (4.1)$$

where Y_{mm} is the small signal admittance matrix defined for the 3 port model detailed in Fig. 4.1 as follows:

$$\begin{bmatrix} \Psi_1 \\ 0 \\ \Psi_{-1} \end{bmatrix} = \begin{bmatrix} Y_{1,1} + Y_1 & Y_{1,0} & Y_{1,-1} \\ Y_{0,1} & Y_{0,0} + Y_L & Y_{0,-1} \\ Y_{-1,1} & Y_{-1,0} & Y_{-1,-1} + Y_{-1} \end{bmatrix} \begin{bmatrix} v_1 \\ 0 \\ v_{-1} \end{bmatrix} \quad (4.2)$$

This admittance matrix fully describes the behavior of the SIS mixer. However, one of the key parameters for the design is the RF conductance $G_{1,1}$ and susceptance $B_{1,1}$ for the image and signal frequencies. For a DSB mixer:

$$Y_{1,1} = Y_{-1,-1} = G_{1,1} + jB_{1,1} \quad (4.3)$$

From Tucker's quantum mixing theory, these values can be calculated employing the following set of equations:

$$G_{1,1} = \frac{e}{2\hbar \omega_{LO}} \sum_{n=-\infty}^{\infty} [J_{n-1}(\alpha)^2 - J_{n+1}(\alpha)^2] I_{DC} \left(V_0 + n \frac{\hbar\omega}{e} \right) \quad (4.4)$$

$$B_{1,1} = \frac{e}{2\hbar \omega_{LO}} \sum_{n=-\infty}^{\infty} [J_{n-1}(\alpha)^2 - 2J_n(\alpha)^2 + J_{n+1}(\alpha)^2] I_{KK} \left(V_0 + n \frac{\hbar\omega}{e} \right) \quad (4.5)$$

Where I_{DC} and I_{KK} are the un-pumped current-voltage curve (IVC) of the SIS junction and its Krammers-Kroning transform, respectively. Meanwhile, α is the pumping factor defined as $\alpha = \frac{eV_{LO}}{\hbar\omega}$ which is closely related to the level of LO pumping. Moreover, J corresponds to the

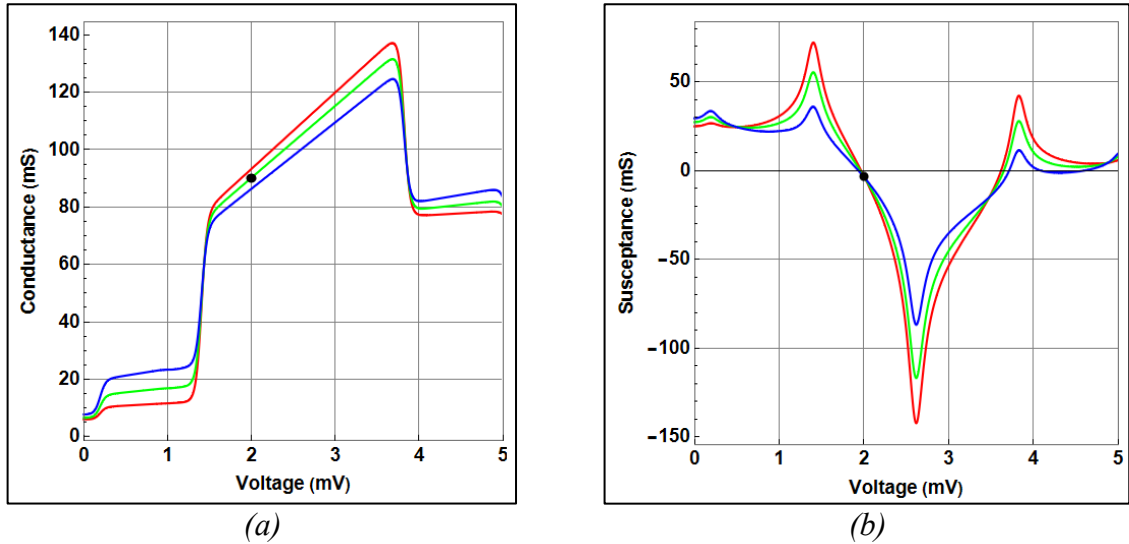


Fig. 4.2. Example of simulated real and imaginary parts of the complex admittance for the SIS junction at RF. The nominal bias point is marked with a black dot. (a) RF conductance for 3 values of α , 0.5 (blue), 0.8 (green), and 0.9 (red). (b) RF susceptance for 3 values of α , 0.5 (blue), 0.8 (green), and 0.9 (red). Note that the design's nominal bias voltage is generally chosen in the middle of the first photon step before the gap voltage V_g where $B_{1,1}$ is closer to 0.

Bessel function of the first kind, V_0 is the bias voltage of the SIS junction, \hbar is the reduced Plank constant and e is the electron charge. In Fig. 4.2 examples of the simulated $G_{1,1}$ and $B_{1,1}$ for different bias voltages are displayed.

In the design process, the SIS is biased in the middle of the first photon step below the gap voltage V_g . This bias condition makes $B_{1,1}$ approximately 0, and therefore the junction geometric capacitance, C_g , defines the resultant imaginary part of the SIS junction admittance. Then, the SIS could be represented at RF by an equivalent circuit with the quantum conductance shunted by the geometric capacitance as shown in Fig.4.3a.

To calculate the IF response, the mixer chip's IF impedance needs to be calculated, which is the parallel combination of real R_{IF} and imaginary C_{IF} components. The slope of the pumped I-V curve determines the real component of the IF output impedance, which is typically 8-10 times R_n [24]. Meanwhile, the C_{IF} capacitance is defined as the sum of the junction capacitance C_J and the matching circuitry capacitance C_M , as illustrated in Fig. 4.3b. C_M is the equivalent capacitance of the RF/LO matching circuit at IF. This capacitance will set a limit to the achievable IF bandwidth, and therefore, it is desirable to minimize it.

Modern mixer designs take advantage of 3D electromagnetic simulation software such as High-Frequency Structure Simulator (HFSS). Such simulators allow the simulation and extraction of the complex embedded admittance of the mixer Y_1 . Furthermore, it is possible to introduce the simulation of superconducting microstrips and slotlines employing surface impedance models as detailed in [107] [108]. The junction complex impedance for the intended frequency range can be introduced into the model employing lumped ports.

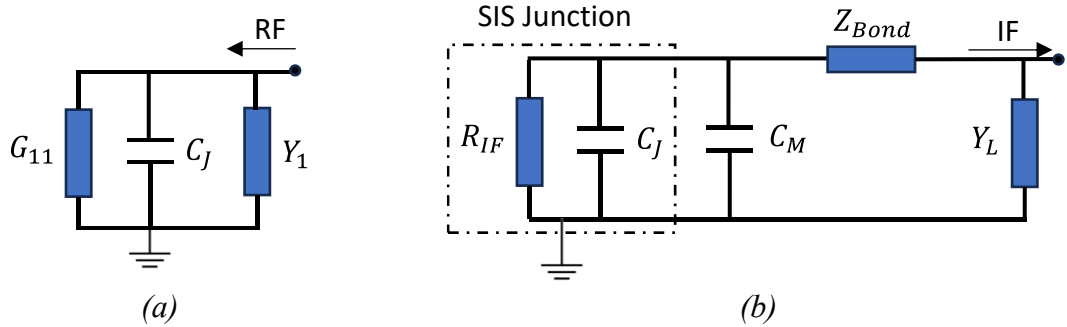


Fig. 4.3. Equivalent circuits for SIS at RF and IF. (a) RF equivalent circuit for a single junction bias at nominal voltage. $G_{1,1}$ is the conductance of the SIS and C_J its geometric capacitance. Y_1 is the embedded admittance of the mixer, i.e. the admittance showed to the junction by the waveguide-to-substrate transition and the RF matching circuitry. (b) Simplified IF equivalent circuit for a single SIS junction. C_M corresponds to the capacitance added by the RF matching circuitry. Y_L is the load impedance that might be adjusted to control the conversion efficiency of the mixer. It is important to consider the impedance of the bonding wires for IF extraction Z_{Bond} .

4.1.2 – RF matching techniques for SIS junctions

The RF matching circuit is designed to efficiently couple the incoming signal to the SIS impedance by canceling the susceptance and matching the conductance. This is generally accomplished by employing one or several SIS junctions [105] [38] [103] [134] with one or more matching sections to the waveguide-to-substrate transition. A classical solution for RF matching is a small piece of inductive line employed to compensate for the susceptance of the junction while a $\lambda/4$ open stub creates an IF extraction point [137] as depicted in Fig. 4.4a.

Variations of this technique are commonly found in the literature. For instance, a radial stub might be used to compensate for the susceptance [85]. This type of stub has a broadband performance when compared with line stubs. Nonetheless, its large area adds extra capacitance at IF, compromising the IF bandwidth.

A broadband matching might be achieved by employing a twin junction configuration [105] [106] shown in Fig.4.4b. The twin junction is composed of 2 SIS junctions separated by a piece of line that acts as an impedance inverter. As a consequence, the susceptance of the junctions are mutually canceled providing a broadband RF matching. Nonetheless, the twin junction arrangement also increases the total capacitance of the circuit, which together with the capacitance of the matching circuitry will ultimately limit the achievable IF bandwidth. Moreover, the twin junction configuration lacks a “cold point” for IF extraction, defined as the part of the circuit that is at the lowest potential energy. Therefore, a high-impedance line might be employed for that purpose [38].

Although the twin junction arrangement provide a broadband RF response, the quality factor of a junction, defined as $Q = \omega R_n C_j$ determinates the maximum bandwidth where the SIS junction can be matched to the embedding circuit. Note that the direct calculation of C_j requires the barrier thickness measurement. However, since this parameter is challenging to measure, the specific capacitance C_s (fF/ μm^2) is usually measured. Then, the product of C_s and $R_n A$

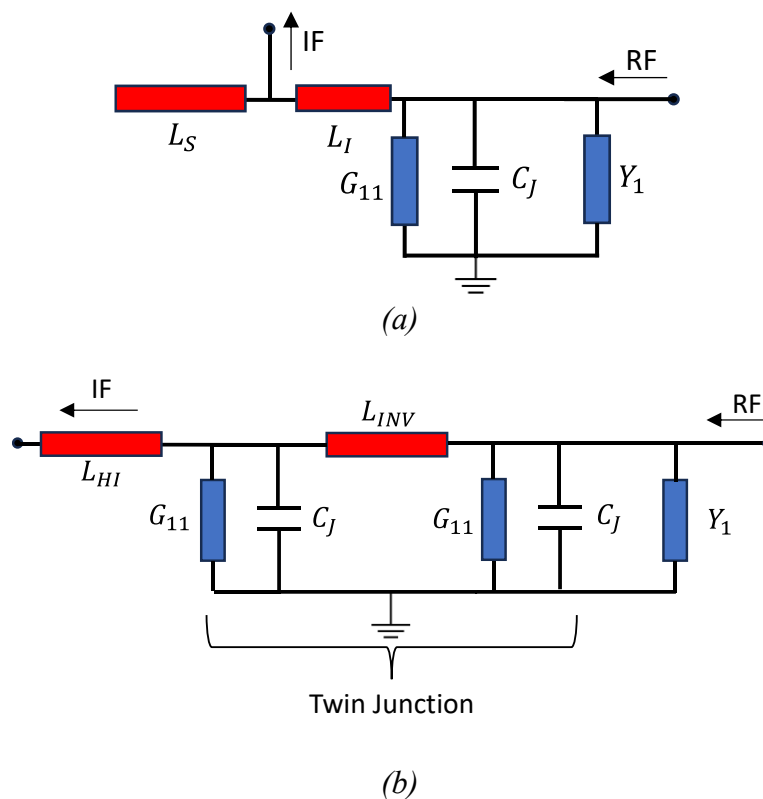


Fig. 4.4. Equivalent circuits for SIS RF matching. The IF extraction point is shown in each case. Note that to increase the RF/LO rejection a filter is commonly employed at the IF extraction. (a) A single SIS junction with an inductive piece of line L_I for susceptance compensation and open $\lambda/4$ stub to create a point for IF extraction. (b) RF equivalent circuit for twin junction. The piece of line L_{INV} between the junctions acts as an impedance inverter to cancel the capacitive susceptance. A high-impedance line L_{HI} is commonly employed for IF extraction.

($\Omega \cdot \mu\text{m}^2$) is equal to the RC product of the junction for a given barrier thickness. In addition, this depends on the barrier material. The next subsection describes the differences and advantages of Nb-based SIS junctions and their relation with the Q factor.

4.1.3 – Overview of Nb-based SIS junctions: Nb/Al- AlO_x /Nb and Nb/Al-AIN/Nb

In order to increase the achievable RF bandwidth of an SIS mixer the quality factor of a junction, defined as $Q = \omega R_n C_j$ should be decreased. Reducing the area of the junction will not suffice to reduce the Q factor since C linearly decreases with the area while R_n increases. Therefore, to effectively reduce the Q factor, the $R_n A$ ($\Omega \cdot \mu\text{m}^2$) product must also be lowered, or equivalently employ thinner barriers and higher current densities. However, the significant reduction of the $R_n A$ product might degrade the junction quality increasing the leakage current I_j . For Nb/Al- AlO_x /Nb SIS the quality typically degraded below $15 \Omega \cdot \mu\text{m}^2$ [136]. An alternative solution is to employ a different material for the barrier such as Nb/Al-AIN/Nb junctions which have thicker tunnel barriers for the same current density as compared to other SIS technologies as AlO_x tunnel barrier junctions. Simultaneously, the thicker tunnel barrier has lower specific capacitance, thus further contributing to the decreased Q. In Fig.4.5, the graph depicts C_s (fF/ μm^2) as a function of the $R_n A$ product for AlO_x and AIN SIS technologies. From the graph, it is seen that Nb/Al-AIN/Nb junctions can reach lower C_s for the same $R_n A$, reaching lower Q factors. The next section analyzes a selection of the last decade's SIS mixers and the employment of Nb/Al-AIN/Nb technology.

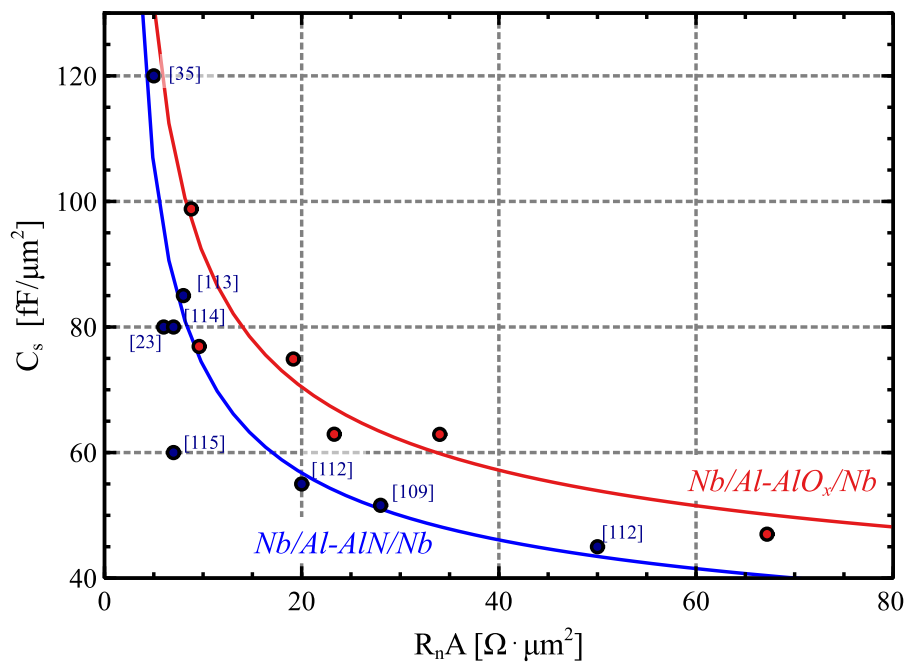


Fig. 4.5. Specific capacitance as a function of $R_n A$ for SIS barriers of AlO_x and AIN for various authors. The Nb/Al- AlO_x /Nb data points are extracted from [111]. The graph was adapted from [109]. The C_s capacitance data for the junctions are approximated with the relation $C_s = a / \ln(R_n A)$ [110], where a is equal to 211 [111] for the Nb/Al- AlO_x /Nb junctions and 170 for Nb/Al-AIN/Nb junctions [112].

4.1.4 – State of The Art SIS Mixers

Recent developments in the field of SIS mixers are shown in Table 4.1 for frequencies ranging from 100 to 1300 GHz. A selection of the most advanced SIS mixers is shown in this table, which highlights the advancements made in the last decades. There has been a noticeable change in favor of Nb/Al-AlN/Nb SIS mixers, which has been attributed to their improved performance characteristics over their Nb/Al-AlOx/Nb counterparts. Research has shown that mixers using both Nb/Al-AlOx/Nb and Nb/Al-AlN/Nb junctions and operating in the same frequency range often show a tendency toward lower noise temperatures for AlN technology, i.e., such as the mixers presented in [26] and [23] in particular.

Furthermore, the table shows a slow evolution towards greater intermediate frequency (IF) bandwidths from 4-8 GHz to 4-12 GHz or greater. One notable example is the mixer described in [132], which attained an exceptional 4–21 GHz instantaneous bandwidth. Regarding RF bandwidth, it has proven difficult to find SIS mixers in the literature covering an RF fractional bandwidth larger than 30%. However, the mixer design in [132] is particularly noteworthy since it achieves a 58% RF fractional bandwidth and covers both of the current ALMA bands 7 and 8 (275 GHz and 500 GHz).

From the table, it is also seen that twin junction configurations are preferred over single junction since they are easier to match across wider bandwidths. Furthermore, compared to silicon membranes, the table shows that low dielectric constant quartz substrates have been the preferred substrate for SIS mixers. As shown in Fig. 4.6, the analysis also shows that most of the examined mixers have a DSB noise temperature that is between ten times the quantum noise and 2 times the fundamental quantum noise limit ($2hf/k$) [121]. Furthermore, it is seen that E-probes are a well-established technology as the waveguide to substrate transition in most SIS mixers. Nonetheless, there are some outliers, such as the Fineline-based works showcased in references [105] and [78].

In the context of modern SIS mixers, **[Paper F]** and **[Paper G]** present a novel mixer design with a target IF bandwidth of 4-16 GHz that stands out from existing designs. Moreover, the proposed mixer is designed to cover a remarkable RF fractional bandwidth of 56%, covering the frequency range of 211-375 GHz. Such value has been achieved only in [132]. Furthermore, the proposed mixer integrates the most recent SIS technology with a twin junction arrangement and $1 \mu\text{m}^2$ Nb/Al-AlN/Nb junctions. In addition, the mixer distinguishes itself from earlier designs by the introduction of metallic substrates which marks a new approach in SIS mixer design. In the next section, the design, simulation, and fabrication of the proposed SIS mixer is detailed.

Table 4.1 - Selection of State-of-The-Art SIS Mixers											
Ref	Year	DSB Noise [K]		FL [GHz]	FU [GHz]	FBW [%]	IF [GHz]	SIS Barrier Technology	SIS Configuration	Waveguide-to-substrate transition	Substrate material
		Lowest	Highest								
122	2006	240	350	800	960	18,2	4-8	O	T	P	Q
		500	970	960	1120	15,4					
123	2006	30	50	275	370	29,5	4-8	O	T	P	Q
138	2007	330	490	1100	1275	12,7	4-8	N	T	A	NR
140	2007	15	28	275	427	42,8	4-8	N	T	P	Q
125	2008	100	175	385	500	26,0	4-12	O	T	P	Q
126	2010	100	245	600	720	18,2	4-8	O	S	P	Q
78	2012	145	1000	600	700	15,4	4-12	O	S	F	Q
127	2012	25	67,5	275	373	30,2	4-8	O	S	P	Q
128	2013	19	25	163	211	25,7	4-8	O	T	P	Q
124	2013	160	270	787	950	18,8	4-12	O	T	P	Q
129	2014	21,5	25	125	163	26,4	4-8	O	T	P	Q
103	2014	15	20	84	116	32,0	4-8	O	4 Junctions	P	Q
		25	90	211	275	26,3	4-12	O			
135	2014	10	24	180	280	43,4	4-8	N	T	P	Q
		22	30	390	520	28,0	4-8	N	T	P	Q
26	2015	70	125	600	720	18,2	4-12	N	S	P	Q
		80	200					O			
114	2016	240	550	790	950	18,4	NR	N	T	P	Q
130	2019	210	400	800	950	17,1	4-12	N	T	NR	NR
131	2020	125	240	410	510	21,7	3.2-8	N	T	NR	MgO
132	2020	37,5	57	275	500	58,1	4-21	N	S	P	Q
133	2020	25	32,5	211	275	26,3	NR	O	S	P	Q
23	2020	53	250	500	600	18,2	4-8	O	T	P	S
		55	125					N			
141	2020	55	80	325	375	14,0	4-8	O	S	P	Q
28	2022	37,5	87,5	272	376	32,1	4-12	O	T	P	Q
105	2022	40	80	210	260	21,3	2-12	O	S	F	Q
134	2023	30	42	300	360	18,2	4-13	O	S	P	NR
		47,5	61,5	300	360	18,2	4-17	O	3 Junctions	P	NR
Paper G	2024	-	-	211	375	56,0	4-16	N	T	MF	M

FL= Lower Frequency FU= Upper Frequency FBW= Fractional Bandwidth
 O=AlOx N=AlN T= Twin junction S=Single Junction P= E-probe F= Finline MF=Metallic Finline A=Slot Antenna
 Q=Quartz S=Silicon M=Metallic

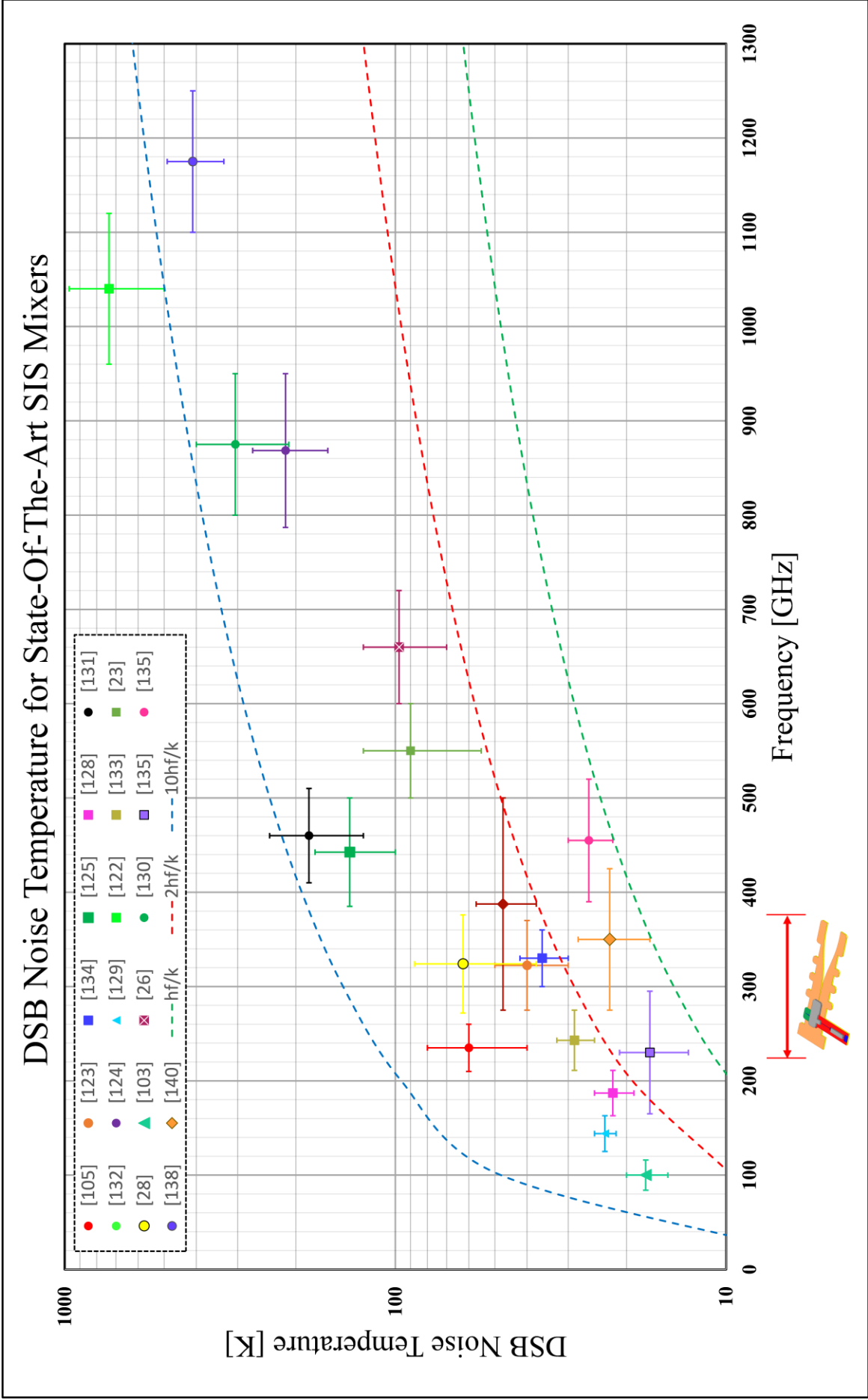


Fig. 4.6. Selection of State-of-the-Art SIS mixer of the last decades. The DSB noise temperature in (log scale) vs frequency is depicted. The center frequency (linear scale) is marked with a point. The x bars indicate the RF bandwidth. The y bars depict the maximum and minimum noise temperature over the RF band. Note that for clarity, not all the mixers from Table 4.1 are displayed here. The intended bandwidth for the mixer proposed in **[Paper G]** is shown for comparison. The DSB noise temperatures are as reported on each reference. In most cases, the reported values are corrected noise temperatures.

4.2 – Ultra-Wideband SIS Mixer Design and Simulation

To achieve a 56% fractional bandwidth, a new broadband SIS mixer has been developed and is intended for use in the 211-375 GHz frequency range. Fig. 4.7a depicts the 3D drawings of the mixer block for DSB measurements. Furthermore, Fig. 4.7b shows the mixer chip and the IF board arrangement.

The proposed design deviates significantly from typical designs since it employs a metallic substrate instead of a standard dielectric substrate for the Nb-Al/AlN-Nb SIS junctions and RF matching circuits. This innovative solution reduces dielectric losses, and unwanted substrate modes as well as makes the chip grounding and substrate shaping easier, especially when incorporating a metallic finline transition. Employing a metallic finline waveguide-to-substrate transition that is integrated into the substrate as depicted in Fig. 4.7c, the design provides impedance matching over a wide range of frequencies without requiring waveguide backshorts. Due to its mounting tolerance, this design also simplifies the block fabrication. As displayed in Fig. 4.7d, the RF matching network consists of a 3rd-order Marchand Balun from slotline to microstrip and a 2-section Chebyshev transformer that effectively couples the incoming RF and LO signals to the twin junctions. As mentioned in the previous section, the twin SIS junction configuration is employed to facilitate broader bandwidth by compensating the imaginary RF impedance of the junctions. The RF resistance of each SIS junction is approximately 11.6 Ohm at the central frequency of 293.5 GHz and its specific junction capacitance, C_s , is determined to be 64.4 fF/ μm^2 .

To provide support to the suspended microstrip lines and help with impedance matching, the chip keeps a silicon layer in key locations, guaranteeing the robustness of the design. To minimize the total capacitance for achieving a larger IF bandwidth, two SiO₂ sections of different thicknesses are incorporated: a thicker layer for the RF filter and Marchand balun, and a thinner layer for the microstrip inverter of the twin junction.

The SIS mixer partially integrates the IF circuitry on the same chip for the 4–16 GHz band. In particular, an RF/LO filter integrated into the chip makes use of an LC circuit with high and low-impedance lines to build an effective low-pass filter, addressing the lack of a natural "cold point" of the twin junction configuration for IF extraction. The total capacitance is calculated to be 376 fF. Moreover, to prevent excessive conversion gain and ensure stable operation of the mixer, the IF load impedance was set to 20 Ω , using a transformer from 50 Ω . This superconducting multisection transformer is realized on an alumina substrate and integrates a broadband bias T.

The Ansys HFSS simulation results reveal an RF coupling to the twin-junction of over 93% across the intended bandwidth, and for the majority of the 4-16 GHz band, the IF circuitry demonstrates losses below 0.3 dB. The simulated performance is shown in Fig. 4.8.

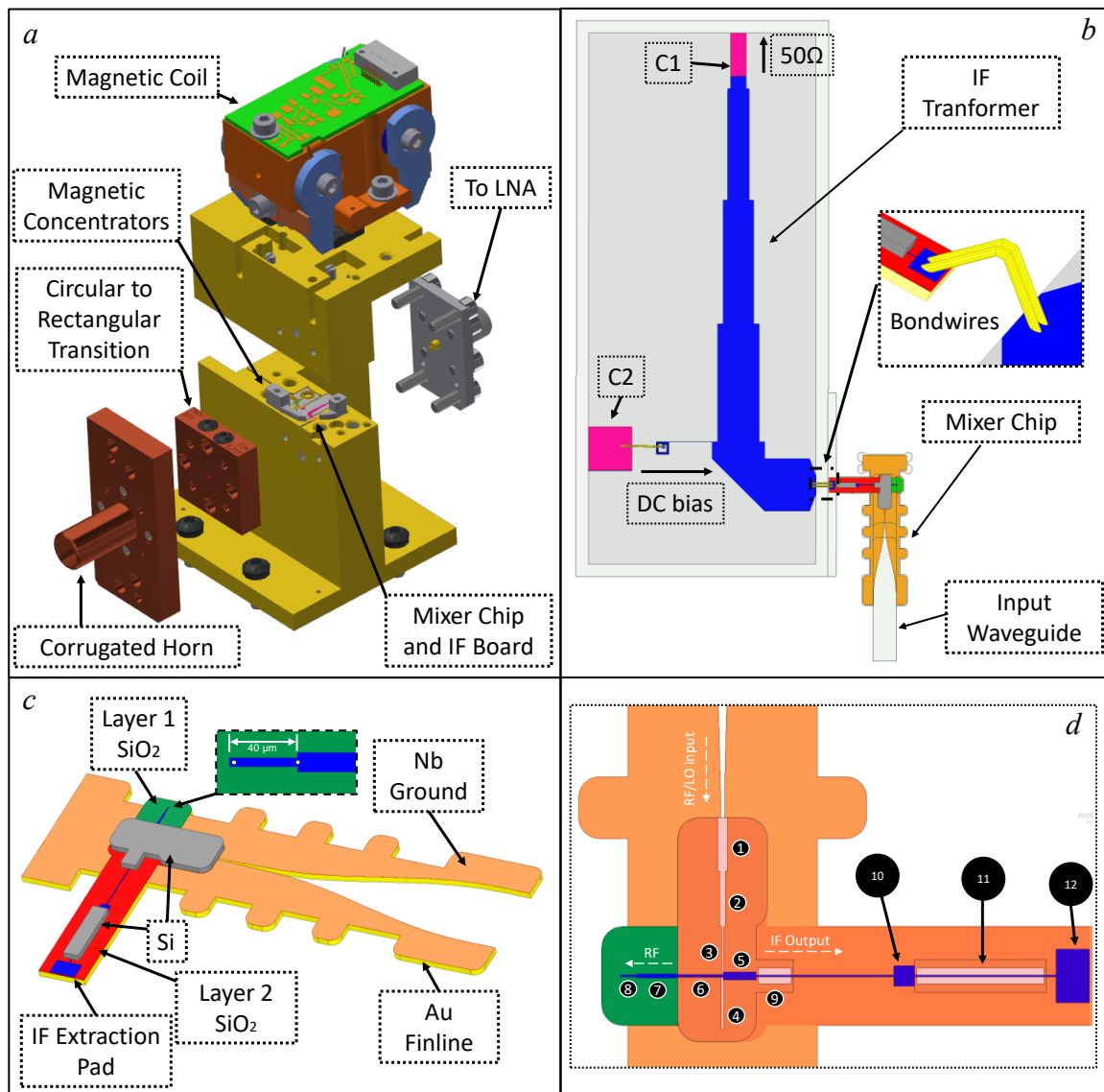
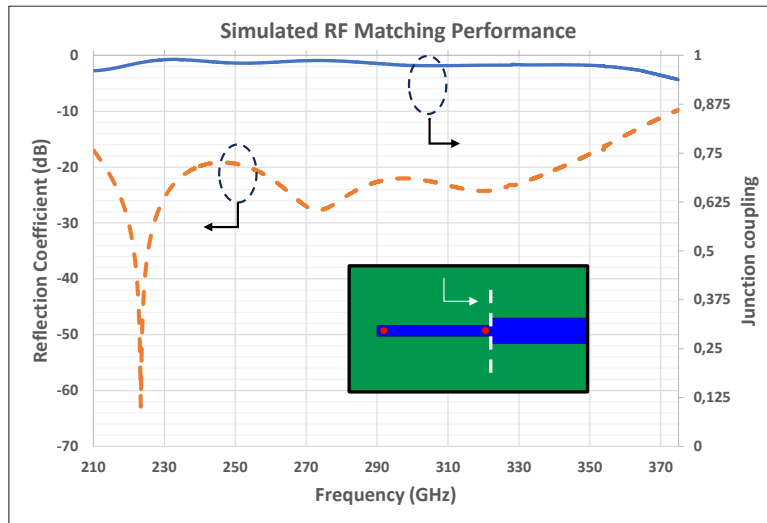
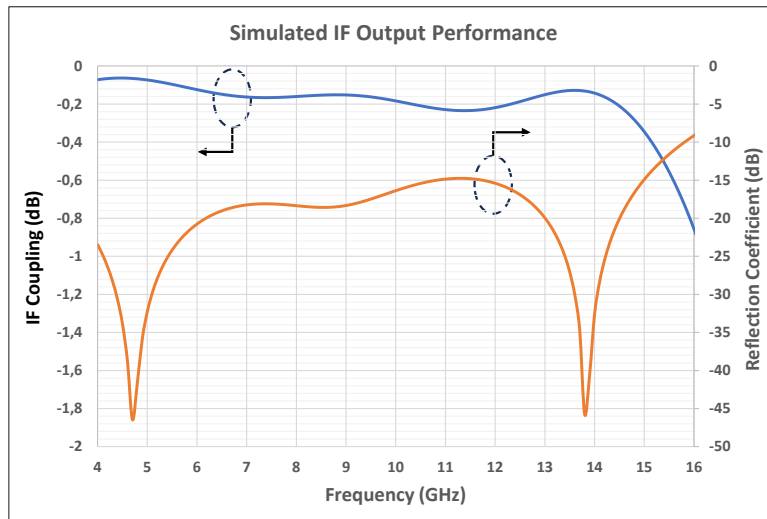


Fig. 4.4. Proposed Mixer Chip in [Paper G]. (a) Exploded view of the DSB block 3D model. (b) Detailed view of the IF board and a layout of the mixer chip. (c) Mixer chip's different layers. (d) Detail of the RF matching and IF output circuitry integrated on the metallic chip. Slotlines 1 and 2 are employed for reducing the impedance from 100 Ohm to 60 Ohm, facilitating a smoother transition from slotline to microstrip. The Marchand Balun is formed by slotlines 3 and 4, and microstrips 5 and 6. This transition is employed for further impedance transformation, acting as a bridge between the higher impedance slotlines and the lower impedance required by the SIS junctions. Microstrips 6 and 7 are a two-section Chebyshev transformer for a broadband impedance match to the SIS junctions. Line 8 is the impedance inverter of the twin junction. Lines 9 to 12 constitute the IF extraction circuitry, forming the RF/LO filter. Suspended microstrips are employed as high-impedance lines.



(a)



(b)

Fig.4.8. Simulated performance of the proposed mixer: (a) Simulated performance of the RF matching circuit. For the HFSS simulation, a lumped port is located as illustrated in the insert. The impedance values for the twin junction circuit were calculated and loaded in the lumped port. (b) Simulated performance for the IF Output circuit.

4.3 – A Novel Technological platform for SIS mixer Design

4.3.1 – Motivation

The choice of substrate material significantly impacts the development of mm and Sub-mm circuits, as it requires a balance between low RF losses, compatibility with cryogenic operation, mechanical robustness, and the possibility of depositing high-quality superconducting films. Among the many requirements, it is desired to have a low dielectric constant to prevent the excitation of undesirable electromagnetic modes, ease of electrical contact, and the possibility to shape the substrate to allow suitable waveguide transitions for minimizing insertion loss [Paper D]. Quartz substrates have traditionally been preferred for

their low dielectric constant and low dielectric loss at THz frequencies. However, this substrate material imposes limitations in shaping the substrate restricting the possibilities for waveguide-to-substrate transitions to mainly E-probes. Silicon, particularly Silicon-on-Insulator (SOI), stands out as an alternative substrate due to the well-established deep silicon etching technology [119] [120], which is suitable for precise substrate shaping. Nonetheless, its high dielectric constant ($\epsilon_r \sim 11.7$) requires ultra-thin membrane-like structures that are brittle and difficult to handle [118]. The reduction in the substrate thickness is implemented to minimize excessive coupling to substrate modes and higher-order modes in waveguide-packaged circuits. In order to maintain this condition, the substrate is progressively made thinner as the frequency of operation increases.

The mixer design presented in [**Paper G**] makes use of a metallic substrate with an integrated finline. This approach provides multiple advantages over existing substrates. Namely, those are: eliminating the excitation of substrate modes which might allow for higher integration and larger chip areas, and ease of connections through bondwires to the chip, e.g. DC biasing, IF extraction, and grounding via wire bonds or solder bump. Moreover, it provides excellent thermal contact with the block. The metallic substrates have the potential to be employed in other active devices in various applications [116], [117]. However, the feasibility of fabricating active devices such as SIS junctions over metallic substrates has not been reported in the literature yet. Therefore, [**Paper F**] presents a fabrication process for the proposed mixer. The SIS junctions are tested at cryogenic temperatures during various fabrication stages to monitor their quality and assess the viability of the process. In Fig. 4.6, pictures of the fabricated devices are depicted.

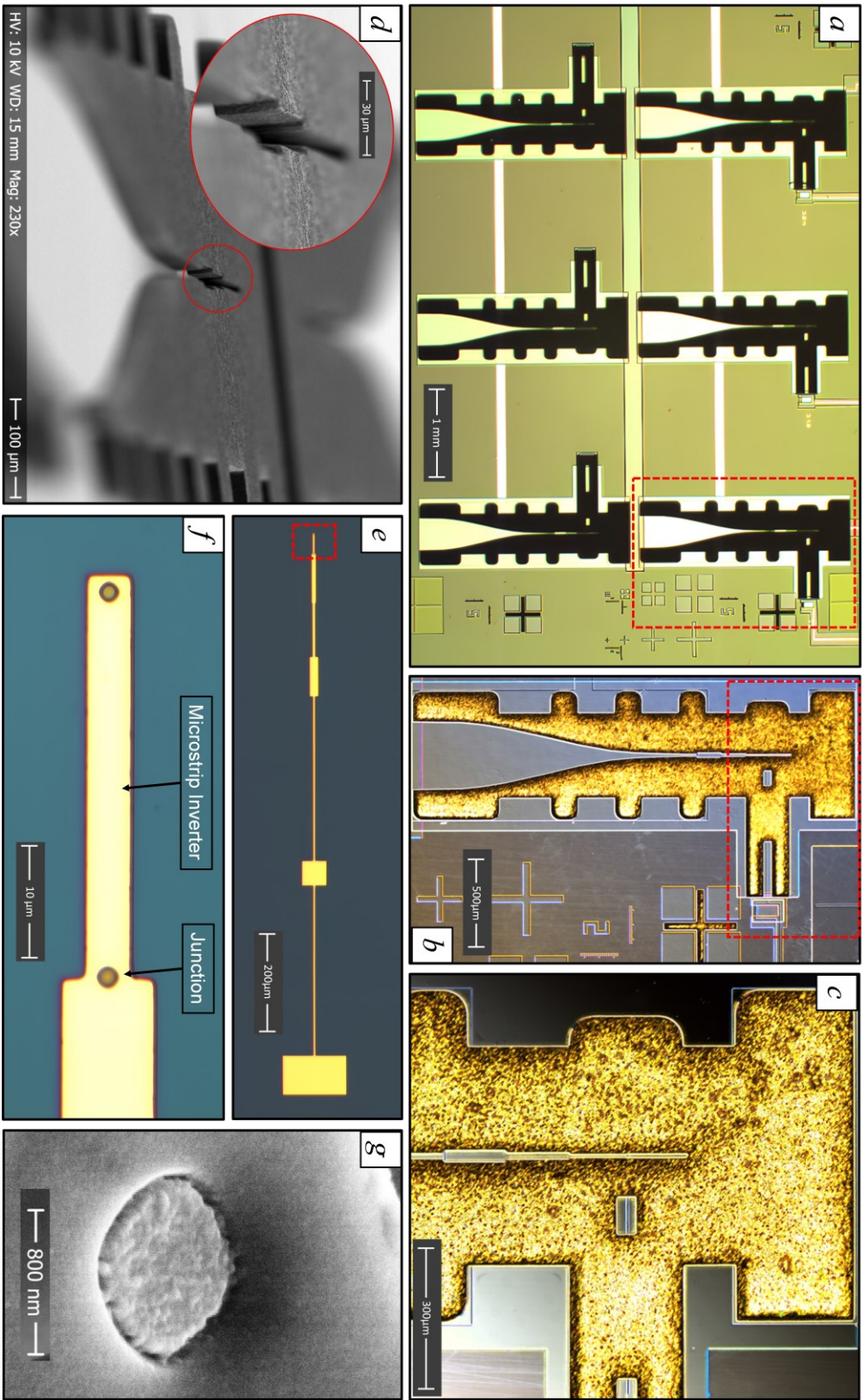


Fig. 4.6. Fabrication of Mixer Chip as presented in [Paper F]. (a) Fabricated devices connected to the DC paths for testing. The device inside the red area is enlarged in the following picture. (b) Fabricated test structure. The electroplated fins are depicted. The area marked with a red dotted line is magnified in the following image (c) Detail of slotline to microstrip transition. The microstrip line is appreciated through the cavities formed in the electroplated Au. (d) SEM images of the electroplated Au finline with the detail of the central transformer. (e) Fabricated microstrip structure. This structure is not visible from the top after the fins are electroplated. The area inside the red rectangle is magnified in the next picture. (f) Fabricated twin junction. (g) SEM image of the SIS junction area after Reactive Ion Etching (RIE) of the top Nb layer of the Nb/Al-AlN/Nb trilayer.

4.3.2 – DC Testing and Results

The IVC of junctions before and after electroplating were investigated using 4-point measurements on 22 devices mounted on a 4K plate in a closed-cycle test cryostat. Fig-4.7 a shows the IV curve of one of the devices before and after electroplating. Note that 5 of the 22 junctions were devices for process control with a single SIS junction. The fabricated devices had nominal sizes ranging from $1.6 \mu\text{m}^2$ to $7.07 \mu\text{m}^2$. However, due to a $0.4 \mu\text{m}$ junction dimension offset typical of the process, the actual areas were between $0.5 \mu\text{m}^2$ and $3.8 \mu\text{m}^2$. The $R_n A$ was extracted from the measurements resulting in a value of $13.24 \Omega \cdot \mu\text{m}^2$ which is close to the target $14 \Omega \cdot \mu\text{m}^2$. The investigation of the R_n values and the R_j/R_n before and after gold plating revealed minor variations and no substantial degradation of the junctions, with R_j/R_n ratios remaining in the high-quality range of 20-30. The results of R_n variation are displayed in Fig. 4.7b. This demonstrates that the gold plating technique does not affect the quality of the SIS connections. The findings support the conclusion that the novel microfabrication process for Nb-Al/AlN-Nb SIS junctions on metallic substrates could be employed for the fabrication of the mixer presented in [Paper G]. Moreover, it has the potential to be used in the development of devices for a variety of applications, including mixers, frequency multipliers, and substrate-based components.

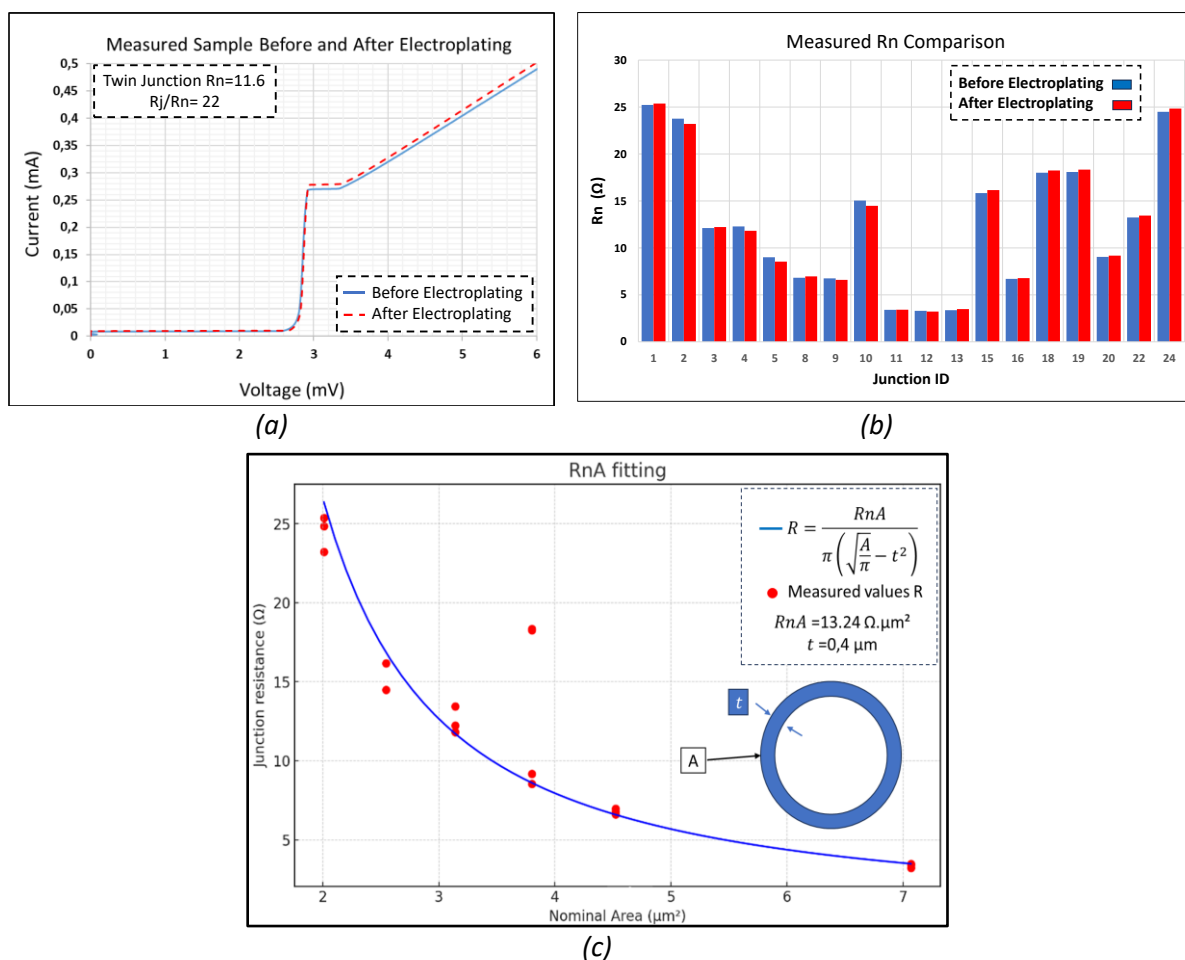


Fig. 4.7. Cryogenic measurements of the SIS junctions. (a) Measured IV curve before and after electroplating. (b) R_n variation before and after electroplating of each fabricated junction. (c) $R_n A$ fitting. The $R_n A$ of the batch results is $13.24 \Omega \cdot \mu\text{m}^2$ with a fabrication offset of $t=0.4 \mu\text{m}$.

Chapter 5

Concluding Remarks and Future Outlook

Even as the radio astronomy receivers at telescopes such as ALMA and APEX continue to make remarkable astronomical discoveries to this day, their future requirements mark a major leap from existing technologies. Furthermore, the next generation Event Horizon Telescope (EHT) has further increased the demand for advanced receiver technology. This thesis addresses the need for such advancements, focusing on the design, fabrication, and testing of components to extend bandwidth capabilities and minimize losses, i.e. minimize its contribution to the noise temperature of the receiver. Moreover, the proposed waveguide components also ensure compactness and reasonable ease of fabrication and assembly.

Although the deadline for developing technology for future radioastronomy receivers is rapidly approaching the target year of 2030, the research of new components and mixers fulfilling the requirements has proven to be a significant technological challenge, as indicated by the extensive review done in this thesis. In particular, the review showed a lack of mixer designs capable of addressing the required RF and IF bandwidth simultaneously. In this context, the mixer proposed in this thesis based on metallic substrates departs from traditional methods. The design is not only intended to achieve a wideband response but also to have a simple mounting process and less the performance dependencies associated with traditional approaches. Furthermore, it opens up new integration possibilities for larger chip areas. Previous attempts to integrate components such as OMTs and S2B mixers on a single chip have encountered difficulties related to resonances due to the dielectric substrates. Consequently, to avoid substrate mode excitation, these designs have to be fabricated onto thin membranes that are difficult to handle and mount. Metallic substrates, as proposed in this thesis, could potentially overcome these problems, allowing for the manufacturing of far thicker metallic chips for easing handling and mounting while being free from substrate-based resonances. This innovation might allow for the integration of several components on a single platform, providing more freedom and flexibility in the design and manufacture of various structures.

Implementing the proposed mixer brought new possibilities for future research while also posing challenges. In particular, the development of a microfabrication process for SIS junctions over metallic substrates required a significant effort. The culmination of this effort was the microfabrication process and the cryogenic DC characterization of SIS junctions presented in this thesis. Furthermore, this work expands the use of metallic substrates beyond SIS junctions to other applications that might employ diverse detectors such as HEB and Schottky diodes, yet demonstrating our ability to fabricate Nb/Al-AlN/Nb junctions with high quality and achieve the desired R_nA . With the metallic substrate concept validated and DC characterization of fabricated SIS junctions accomplished, the next step is to investigate the proposed mixer's RF performance. At the moment of writing this thesis, the mixer chips are near completion and the components needed for cryogenic DSB performance measurement are being fabricated. We plan to test the mixer structures once they are finally produced in the near future but beyond the scope of this thesis.

Bibliography

- [1] A. Rogalski and F. Sizov, "Terahertz detectors and focal plane arrays," in *Opto-electronics Review*, vol. 19, no. 3, pp. 346-404, 2011, doi: 10.2478/s11772-011-0033-3.
- [2] E. Pickwell and V. P. Wallace, "Biomedical applications of terahertz technology," in *Journal of Physics D: Applied Physics*, vol. 39, no. 17, p. R301, 2006, doi: 10.1088/0022-3727/39/17/R01.
- [3] B. Ferguson and X.-C. Zhang, "Materials for terahertz science and technology," in *Nature Materials*, vol. 1, no. 1, pp. 26-33, Sept. 2002, doi: 10.1038/nmat708.
- [4] Farrah et al., "Far-infrared instrumentation and technological development for the next decade," in *Journal of Astronomical Telescopes, Instruments, and Systems*, vol. 5, no. 2, p. 020901, April 2019, doi: 10.1117/1.JATIS.5.2.020901.
- [5] H. -J. Song and T. Nagatsuma, "Present and Future of Terahertz Communications," in *IEEE Transactions on Terahertz Science and Technology*, vol. 1, no. 1, pp. 256-263, Sept. 2011, doi: 10.1109/TTHZ.2011.2159552.
- [6] B. Billade *et al.*, "Performance of the First ALMA Band 5 Production Cartridge," in *IEEE Transactions on Terahertz Science and Technology*, vol. 2, no. 2, pp. 208-214, March 2012, doi: 10.1109/TTHZ.2011.2182220.
- [7] H. Rashid, S. Krause, D. Meledin, V. Desmaris, A. Pavolotsky and V. Belitsky, "Frequency Multiplier Based on Distributed Superconducting Tunnel Junctions: Theory, Design, and Characterization," in *IEEE Transactions on Terahertz Science and Technology*, vol. 6, no. 5, pp. 724-736, Sept. 2016, doi: 10.1109/TTHZ.2016.2583201.
- [8] S. Krause, D. Meledin, V. Desmaris, A. Pavolotsky, H. Rashid and V. Belitsky, "Noise and IF Gain Bandwidth of a Balanced Waveguide NbN/GaN Hot Electron Bolometer Mixer Operating at 1.3 THz," in *IEEE Transactions on Terahertz Science and Technology*, vol. 8, no. 3, pp. 365-371, May 2018, doi: 10.1109/TTHZ.2018.2824027.
- [9] Y. Tamura et al., "The 300 parsec resolution imaging of a $z= 8.31$ galaxy: Turbulent ionized gas and potential stellar feedback 600 million years after the Big Bang," arXiv preprint arXiv:2303.11539, 2023. <https://doi.org/10.48550/arXiv.2303.11539>.
- [10] T. Wong et al., "The 30 Doradus molecular cloud at 0.4 pc resolution with the Atacama Large Millimeter/submillimeter Array: Physical properties and the boundedness of CO-emitting structures," in *The Astrophysical Journal*, vol. 932, no. 1, p. 47, 2022, doi: 10.3847/1538-4357/ac723a.
- [11] S. Ohashi et al., "Dust enrichment and grain growth in a smooth disk around the DG Tau protostar revealed by ALMA triple bands frequency observations," in *The Astrophysical Journal*, vol. 954, no. 2, p. 110, 2023, doi: 10.3847/1538-4357/ace9b9.
- [12] Event Horizon Telescope Collaboration, K. Akiyama et al., "First Sagittarius A* event horizon telescope results. V. Testing astrophysical models of the galactic center black hole," in *The Astrophysical Journal Letters*, vol. 930, no. 2, p. L16, 2022, doi: 10.3847/2041-8213/ac6672.
- [13] "Atacama Large Millimeter/submillimeter Array ALMA," ESO, [Online]. Available: <https://www.almaobservatory.org/en/home/> Accessed: 17-Feb-2024.
- [14] "Event Horizon Telescope," Event Horizon Telescope Collaboration, 2023, [Online]. Available: <https://eventhorizontelescope.org/> Accessed: 19-Jan-2024.

- [15] "Northern Extended Millimeter Array NOEMA," IRAM Institut de Radioastronomie Millimétrique, [Online]. Available: <https://www.iram-institute.org/EN/noema-project.php> Accessed: 17-Feb-2024.
- [16] "Atacama Pathfinder Experiment APEX," ESO, Max-Planck-Institut für Radiastonomie, Onsala Rymdobservatorium, [Online]. Available: <http://www.apex-telescope.org/ns/> Accessed: 17-Feb-2024
- [17] Y. D. Huang et al., "ALMA Band-1 (35-50GHz) receiver: first light, performance, and road to completion," in *Proceedings of Millimeter, Submillimeter, and Far-Infrared Detectors and Instrumentation for Astronomy XI*, vol. 12190, SPIE, Sept. 2022, <https://doi.org/10.1117/12.2629766>.
- [18] V. Belitsky et al., "ALMA Band 2 Cold Cartridge Assembly Design," in *Proceedings of the 32nd IEEE International Symposium on Space THz Technology*, Baeza, Spain, October 16-20, 2022, 2023. [Online]. Available: <https://research.chalmers.se> Accessed: 17-Feb-2024.
- [19] J. Carpenter et al., "The ALMA2030 Wideband Sensitivity Upgrade," arXiv preprint arXiv:2211.00195, 2022. <https://doi.org/10.48550/arXiv.2211.00195>
- [20] J. D. Kraus et al., Radio Astronomy, Powell, Ohio: Cygnus-Quasar Books, 1986.
- [21] M. Morgan and S. Weinreb, "A monolithic HEMT diode balanced mixer for 100-140 GHz," *2001 IEEE MTT-S International Microwave Symposium Digest (Cat. No.01CH37157)*, Phoenix, AZ, USA, 2001, pp. 99-102 vol.1, doi: 10.1109/MWSYM.2001.966848.
- [22] E. Novoselov and S. Cherednichenko, "Low noise terahertz MgB2 hot-electron bolometer mixers with an 11 GHz bandwidth," *Applied Physics Letters*, vol. 110, no. 3, p. 032601, 2017, DOI: <https://doi.org/10.1063/1.4974312>.
- [23] J. W. Kooi et al., "Quantum Limited SIS Receiver Technology for the Detection of Water Isotopologue Emission From Comets," in *IEEE Transactions on Terahertz Science and Technology*, vol. 10, no. 6, pp. 569-582, Nov. 2020, doi: 10.1109/TTHZ.2020.3010123.
- [24] J. R. Tucker and M. J. Feldman, "Quantum detection at millimeter wavelengths," *Reviews of Modern Physics*, vol. 57, no. 4, p. 1055, 1985.
- [25] T. L. Wilson, K. Rohlf, and S. Hüttemeister, Tools of Radio Astronomy, Berlin: Springer, 2009.
- [26] A. M. Baryshev et al., "The ALMA Band 9 receiver - Design, construction, characterization, and first light," *Astronomy & Astrophysics*, vol. 577, p. A129, May 2015, doi: <https://doi.org/10.1051/0004-6361/201425529>.
- [27] A. R. Kerr et al., "Development of the ALMA Band-3 and Band-6 Sideband-Separating SIS Mixers," in *IEEE Transactions on Terahertz Science and Technology*, vol. 4, no. 2, pp. 201-212, March 2014, doi: 10.1109/TTHZ.2014.2302537.
- [28] D. Meledin et al., "SEPIA345: A 345 GHz dual polarization heterodyne receiver channel for SEPIA at the APEX telescope," *Astronomy & Astrophysics*, vol. 668, A2, Dec. 2022, doi: <https://doi.org/10.1051/0004-6361/202244211>.
- [29] W. R. Deal, K. Leong, W. Yoshida, A. Zamora and X. B. Mei, "InP HEMT integrated circuits operating above 1,000 GHz," *2016 IEEE International Electron Devices Meeting (IEDM)*, San Francisco, CA, USA, 2016, pp. 29.1.1-29.1.4, doi: 10.1109/IEDM.2016.7838502.

- [30] G. Moschetti *et al.*, "A 183 GHz Metamorphic HEMT Low-Noise Amplifier With 3.5 dB Noise Figure," in *IEEE Microwave and Wireless Components Letters*, vol. 25, no. 9, pp. 618-620, Sept. 2015, doi: 10.1109/LMWC.2015.2451355.
- [31] D. M. Pozar, *Microwave Engineering*, John Wiley & Sons, 2011.
- [32] S. Asayama *et al.*, "Development of ALMA Band 4 (125–163 GHz) receiver," *Publications of the Astronomical Society of Japan*, vol. 66, no. 3, 57, June 2014, doi: <https://doi.org/10.1093/pasj/psu026>.
- [33] J. Carpenter, D. Iono, F. Kemper, and A. Wootten, "The ALMA development program: Roadmap to 2030," *Monthly Newsletter of International URSI Commission J Radio Astronomy*, January 2020, arXiv preprint arXiv:2001.11076, 2020. <https://doi.org/10.48550/arXiv.2001.11076>.
- [34] T. Venturi *et al.*, "VLBI20-30: a scientific roadmap for the next decade. The future of the European VLBI Network," preprint arXiv:2007.02347, 2020.
- [35] T. Kojima *et al.*, "275–500-GHz Wideband Waveguide SIS Mixers," in *IEEE Transactions on Terahertz Science and Technology*, vol. 8, no. 6, pp. 638-646, Nov. 2018, doi: 10.1109/TTHZ.2018.2873487.
- [36] A. Navarrini *et al.*, "ALMA Band 6v2 receiver development status," *2023 XXXVth General Assembly and Scientific Symposium of the International Union of Radio Science (URSI GASS)*, Sapporo, Japan, 2023, pp. 1-4, doi: 10.23919/URSIGASS57860.2023.10265563.
- [37] D. Henke and S. Claude, "Design of a 70–116 GHz W-band turnstile OMT," *2014 44th European Microwave Conference*, Rome, Italy, 2014, pp. 456-459, doi: 10.1109/EuMC.2014.6986469.
- [38] V. Belitsky *et al.*, "ALMA Band 5 receiver cartridge - Design, performance, and commissioning," *Astronomy & Astrophysics*, vol. 611, A98, 2018, doi: <https://doi.org/10.1051/0004-6361/201731883>
- [39] G. Maral, M. Bousquet, and Z. Sun, *Satellite Communications Systems: Systems, Techniques and Technology*, John Wiley & Sons, 2020.
- [40] L. Zeng, C. E. Tong, S. N. Paine and P. K. Grimes, "A Compact Machinable 90° Waveguide Twist for Broadband Applications," in *IEEE Transactions on Microwave Theory and Techniques*, vol. 68, no. 7, pp. 2515-2520, July 2020, doi: 10.1109/TMTT.2020.2987800.
- [41] M. Baralis, R. Tascone, A. Olivieri, O. A. Peverini, G. Virone and R. Orta, "Full-wave design of broad-band compact waveguide step-twists," in *IEEE Microwave and Wireless Components Letters*, vol. 15, no. 2, pp. 134-136, Feb. 2005, doi: 10.1109/LMWC.2004.842865.
- [42] M. A. Al-Tarifi and D. S. Filipovic, "Design and Fabrication of a Full W-Band Multi-Step Waveguide 90° Twist," in *IEEE Microwave and Wireless Components Letters*, vol. 26, no. 11, pp. 903-905, Nov. 2016, doi: 10.1109/LMWC.2016.2615025.
- [43] J. A. Ruiz-Cruz, J. R. Montejo-Garai and J. M. Rebollar, "Multi-Section Bow-Tie Steps for Full-Band Waveguide Polarization Rotation," in *IEEE Microwave and Wireless Components Letters*, vol. 20, no. 7, pp. 375-377, July 2010, doi: 10.1109/LMWC.2010.2049428.
- [44] A. A. Kirilenko, D. Y. Kulik and L. A. Rud, "Compact 90° Twist Formed by a Double-Corner-Cut Square Waveguide Section," in *IEEE Transactions on Microwave Theory*

- and Techniques*, vol. 56, no. 7, pp. 1633-1637, July 2008, doi: 10.1109/TMTT.2008.925570.
- [45] A. R. Kerr, M. J. Feldman, and S.-K. Pan, "Receiver noise temperature, the quantum noise limit, and the role of the zero-point fluctuations," in Proc. of the 8th Int. Symp. on Space Terahertz Technology, Harvard University, March 1997, pp. 101-111.
- [46] U. Rosenberg, J. Bornemann and S. Amari, "A Compact and Broadband 90-Degree Waveguide Twist Transformer for Integrated Waveguide Subsystems," *2001 31st European Microwave Conference*, London, UK, 2001, pp. 1-4, doi: 10.1109/EUMA.2001.339174.
- [47] H. Asao, G. Hiraiwa and A. Katayama, "A Compact 90-degree Twist using Novel Ridged Waveguide for Integrated Waveguide Subsystems," *2006 European Microwave Conference*, Manchester, UK, 2006, pp. 1185-1188, doi: 10.1109/EUMC.2006.281188. <https://doi.org/10.1109/ICATT.2009.4435192>
- [48] A. A. Kirilenko et al., "Comparative analysis of novel compact and usual smooth 90-degree twists," in Proceedings of International Conference on Antenna Theory and Techniques, 2009, p. 328-330. doi: <https://doi.org/10.1109/ICATT.2009.4435192>.
- [49] L. Chen *et al.*, "A Micromachined Terahertz Waveguide 90° Twist," in *IEEE Microwave and Wireless Components Letters*, vol. 21, no. 5, pp. 234-236, May 2011, doi: 10.1109/LMWC.2011.2127467.
- [50] G. Chattopadhyay, J. S. Ward, N. Llombert and K. B. Cooper, "Submillimeter-Wave 90° Polarization Twists for Integrated Waveguide Circuits," in *IEEE Microwave and Wireless Components Letters*, vol. 20, no. 11, pp. 592-594, Nov. 2010, doi: 10.1109/LMWC.2010.2068541.
- [51] H. F. Lenzing and M. J. Gans, "Machined waveguide twist," in *IEEE Transactions on Microwave Theory and Techniques*, vol. 38, no. 7, pp. 942-944, July 1990, doi: 10.1109/22.55788.
- [52] M. Mehrabi Gohari, O. Glubokov, S. Yu and J. Oberhammer, "On-Chip Integration of Orthogonal Subsystems Enabled by Broadband Twist at 220–325 GHz," in *IEEE Transactions on Microwave Theory and Techniques*, vol. 71, no. 9, pp. 3929-3936, Sept. 2023, doi: 10.1109/TMTT.2023.3253963.
- [53] A. Quint, J. Kowalewski, F. Merli and T. Zwick, "D-Band 90° Waveguide Twists using 3D Printing and PVD Metallization," *2023 53rd European Microwave Conference (EuMC)*, Berlin, Germany, 2023, pp. 239-242, doi: 10.23919/EuMC58039.2023.10290390.
- [54] L. Deng, Y. Zhang, T. Cao, H. Zhu, T. Zhang and B. Yan, "A Broadband Butterfly-Shaped 90° Waveguide Twist for Rapid Design," in *IEEE Microwave and Wireless Technology Letters*, vol. 33, no. 7, pp. 967-970, July 2023, doi: 10.1109/LMWT.2023.3267301.
- [55] J. -Q. Ding, Y. Zhao and S. -C. Shi, "A Full WR-3 Band and Low-Loss 90° Waveguide Twist Based on CNC," in *IEEE Transactions on Terahertz Science and Technology*, vol. 10, no. 1, pp. 93-96, Jan. 2020, doi: 10.1109/TTHZ.2019.2951064.
- [56] V. Vassilev, V. Belitsky, D. Urbain and S. Kovtonyuk, "A new 3-dB power divider for millimeter-wavelengths," in *IEEE Microwave and Wireless Components Letters*, vol. 11, no. 1, pp. 30-32, Jan. 2001, doi: 10.1109/7260.905959.
- [57] X. Xie, R. Xu, R. Diao and W. Lin, "A New Millimeter-wave Multi-way Power Dividing/Combining Network Based on Waveguide-Microstrip E-plane Dual-Probe

- Structure," *2008 Global Symposium on Millimeter Waves*, Nanjing, China, 2008, pp. 257-259, doi: 10.1109/GSMM.2008.4534616.
- [58] R. Ma, M. Luo, H. Sun, Z. Li, and P. Zheng, "Design and simulation of a W-band two-way power divider based on substrate integrated waveguide," in *2013 IEEE International Conference on Microwave Technology & Computational Electromagnetics*, Qingdao, China, 2013, pp. 100-102, doi: 10.1109/ICMTCE.2013.6812399.
- [59] Y. Zhou, K. Song, S. Guo, Q. Li, M. W. Aidoo and Y. Fan, "Novel Subterahertz High Isolation Stacked-SIW Power Divider," in *IEEE Transactions on Terahertz Science and Technology*, vol. 13, no. 4, pp. 316-323, July 2023, doi: 10.1109/TTHZ.2023.3275820.
- [60] F. Takeda, O. Ishida and Y. Isoda, "Waveguide Power Divider Using Metallic Septum with Resistive Coupling Slot," *1982 IEEE MTT-S International Microwave Symposium Digest*, Dallas, TX, USA, 1982, pp. 527-528, doi: 10.1109/MWSYM.1982.1130780.
- [61] Y. -S. Liu, D. -C. Niu and E. S. Li, "Three-port E-plane bifurcated waveguide power divider at millimeter-wave frequencies," *2012 Asia Pacific Microwave Conference Proceedings*, Kaohsiung, Taiwan, 2012, pp. 998-100, doi: 10.1109/APMC.2012.6421804.
- [62] H. Zhang, D. Y. Shao, and Y. Shao, "A broadband millimeter-wave waveguide power divider with high isolation," *Amer. J. Phys. Appl.*, vol. 7, no. 4, pp. 101-108, 2019. doi:10.11648/J.AJPA.20190704.12.
- [63] A. R. Kerr and N. Horner, "A broadband in-phase waveguide power divider/combiner," *ALMA Memo*, no. 10, 2000.
- [64] Z. Xu, J. Xu, Y. Cui and C. Qian, "A Novel Rectangular Waveguide T-Junction for Power Combining Application," in *IEEE Microwave and Wireless Components Letters*, vol. 25, no. 8, pp. 529-531, Aug. 2015, doi: 10.1109/LMWC.2015.2440775.
- [65] W. Lei, L. Li-hao and Y. Zhi-guo, "A novel power splitter based on the waveguide E-type T junction," *Proceedings of 2012 5th Global Symposium on Millimeter-Waves*, Harbin, China, 2012, pp. 217-219, doi: 10.1109/GSMM.2012.6314039.
- [66] H. Zhu *et al.*, "Spoof Surface Plasmon Polaritons for High-Efficiency Terahertz Power Combiner," in *IEEE Transactions on Microwave Theory and Techniques*, doi: 10.1109/TMTT.2023.3309401
- [67] Z. Dang, Y. Zhang, J. Huang, B. Li, B. Zhang and H. -L. Zhu, "An Isolated Waveguide Divider for W-Band Power Combined Amplifier," in *IEEE Microwave and Wireless Technology Letters*, vol. 33, no. 5, pp. 535-538, May 2023, doi: 10.1109/LMWT.2023.3234373.
- [68] J. Hanning, V. Drakinskiy, P. Sobis, T. Bryllert and J. Stake, "A broadband THz waveguide-to-suspended stripline loop-probe transition," *2017 IEEE MTT-S International Microwave Symposium (IMS)*, Honolulu, HI, USA, 2017, pp. 1091-1094, doi: 10.1109/MWSYM.2017.8058785.
- [69] Z. Dang, Y. Zhang, H. -L. Zhu, B. Yan and R. -M. Xu, "An Isolated Three-Way Power Combiner via Magnetically Coupled Microstrip Ring Probes," in *IEEE Transactions on Microwave Theory and Techniques*, vol. 72, no. 1, pp. 298-307, Jan. 2024, doi: 10.1109/TMTT.2023.3297409.
- [70] J. W. Kooi, "Advanced receivers for submillimeter and far infrared astronomy," PhD Thesis, 2008.

- [71] S. Withington and G. Yassin, "An investigation of the input impedance of a microstrip probe in waveguide," in *Proc. of Eighth International Symposium on Space THz Technology*, March 1997.
- [72] S. Withington, G. Yassin, J. Leech, and K. G. Isaak, "An accurate expression for the input impedance of one-sided microstrip probes in waveguide," in *Tenth International Symposium on Space Terahertz Technology*, March 1999, p. 505.
- [73] J. W. Kooi, G. Chattopadhyay, S. Withington, F. Rice, J. Zmuidzinas, C. Walker, and G. Yassin, "A full-height waveguide to thin-film microstrip transition with exceptional RF bandwidth and coupling efficiency," *International Journal of Infrared and Millimeter Waves*, vol. 24, pp. 261-284, 2003, doi: <https://doi.org/10.1023/A:1021903132609>.
- [74] Z. Xu, J. Xu and C. Qian, "Novel In-Line Microstrip-to-Waveguide Transition Based on E-Plane Probe T-Junction Structure," in *IEEE Microwave and Wireless Components Letters*, vol. 31, no. 9, pp. 1051-1054, Sept. 2021, doi: 10.1109/LMWC.2021.3083281
- [75] C. Wu *et al.*, "Millimeter-Wave Waveguide-to-Microstrip Inline Transition Using a Wedge-Waveguide Iris," in *IEEE Transactions on Microwave Theory and Techniques*, vol. 70, no. 2, pp. 1087-1096, Feb. 2022, doi: 10.1109/TMTT.2021.3123349.
- [76] P. J. Meier, "Two New Integrated-Circuit Media with Special Advantages at Millimeter Wavelengths," *1972 IEEE GMTT International Microwave Symposium*, Arlington Heights, IL, USA, 1972, pp. 221-223, doi: 10.1109/GMTT.1972.1123053.
- [77] B. Tan and G. Yassin, "Unilateral finline transition at THz frequencies," in *Proceedings of the Twentieth International Symposium on Space Terahertz Technology*, April 20-22, 2009, Omni Hotel, Charlottesville, Virginia, pp. 263-266.
- [78] Wienold *et al.*, "OSAS-B: A balloon-borne terahertz spectrometer for atomic oxygen in the upper atmosphere," in *IEEE Transactions on Terahertz Science and Technology*, doi: 10.1109/TTHZ.2024.3363135.
- [79] C. Yao, J. Xu, and M. Chen, "Design of Ka-band antipodal finline mixer and detector," *Journal of Semiconductors*, vol. 30, no. 5, 055009, 2009, DOI: 10.1088/1674-4926/30/5/055009
- [80] G. Chattopadhyay and J. E. Carlstrom, "Finline ortho-mode transducer for millimeter waves," in *IEEE Microwave and Guided Wave Letters*, vol. 9, no. 9, pp. 339-341, Sept. 1999, doi: 10.1109/75.790467.
- [81] G. Yassin, S. Withington, M. Buffey, K. Jacobs and S. Wulff, "A 350-GHz SIS antipodal finline mixer," in *IEEE Transactions on Microwave Theory and Techniques*, vol. 48, no. 4, pp. 662-669, April 2000, doi: 10.1109/22.841957.
- [82] R. Garg, I. Bahl, and M. Bozzi, *Microstrip Lines and Slotlines*, 2nd Edition, Artech House.
- [83] B. K. Tan, *Development of Coherent Detector Technologies for Sub-millimetre Wave Astronomy Observations*, Springer, 2015, ISBN 978-3-319-19363-2.
- [84] B. Zhang, D. Ji, D. Fang, S. Liang, Y. Fan and X. Chen, "A Novel 220-GHz GaN Diode On-Chip Tripler With High Driven Power," in *IEEE Electron Device Letters*, vol. 40, no. 5, pp. 780-783, May 2019, doi: 10.1109/LED.2019.2903430.
- [85] B. K. Tan, G. Yassin, P. Grimes, J. Leech, K. Jacobs and C. Groppi, "A 650 GHz Unilateral Finline SIS Mixer Fed by a Multiple Flare-Angle Smooth-Walled Horn," in *IEEE Transactions on Terahertz Science and Technology*, vol. 2, no. 1, pp. 40-49, Jan. 2012, doi: 10.1109/TTHZ.2011.2177736.

- [86] J. Garrett, B. K. Tan, C. Chaumont, F. Boussaha, and G. Yassin, "An End-Fire SIS Mixer with Near Quantum-Limited Performance," *ESS Open Archive*, April 28, 2022, DOI: 10.22541/au.165115382.22953773/v1.
- [87] C. Risacher, V. Vassilev, A. Pavolotsky and V. Belitsky, "Waveguide-to-microstrip transition with integrated bias-T," in *IEEE Microwave and Wireless Components Letters*, vol. 13, no. 7, pp. 262-264, July 2003, doi: 10.1109/LMWC.2003.815182.
- [88] J. W. Kooi, C. K. Walker, and J. Hesler, "A broad bandwidth suspended membrane waveguide to thin film microstrip transition," in 9th International Conference on Terahertz Electronics, Oct. 2001.
- [89] B. K. Tan, S. Withington and G. Yassin, "A Compact Microstrip-Fed Planar Dual-Dipole Antenna for Broadband Applications," in *IEEE Antennas and Wireless Propagation Letters*, vol. 15, pp. 593-596, 2016, doi: 10.1109/LAWP.2015.2462114.
- [90] B. K. Tan and G. Yassin, "A Slotline DC Block for Microwave, Millimeter, and Submillimeter Circuits," in *IEEE Microwave and Wireless Components Letters*, vol. 29, no. 9, pp. 583-585, Sept. 2019, doi: 10.1109/LMWC.2019.2931467.
- [91] W. Xu, F. Liu, and H. Xu, "A novel ultra-wideband waveguide-to-microstrip transition for millimeter-wave applications," *Aip Advances*, vol. 6, no. 10, 105001, Oct. 2016, doi: <https://doi.org/10.1063/1.4964492>.
- [92] L. Samoska *et al.*, "A Submillimeter-Wave HEMT Amplifier Module With Integrated Waveguide Transitions Operating Above 300 GHz," in *IEEE Transactions on Microwave Theory and Techniques*, vol. 56, no. 6, pp. 1380-1388, June 2008, doi: 10.1109/TMTT.2008.923353.
- [93] A. Aljarosha, A. U. Zaman and R. Maaskant, "A Wideband Contactless and Bondwire-Free MMIC to Waveguide Transition," in *IEEE Microwave and Wireless Components Letters*, vol. 27, no. 5, pp. 437-439, May 2017, doi: 10.1109/LMWC.2017.2690846.
- [94] C. Hannachi, T. Djerafi and S. O. Tatu, "Broadband E -Band WR12 to Microstrip Line Transition Using a Ridge Structure on High-Permittivity Thin-Film Material," in *IEEE Microwave and Wireless Components Letters*, vol. 28, no. 7, pp. 552-554, July 2018, doi: 10.1109/LMWC.2018.2835475.
- [95] A. Tessmann *et al.*, "Metamorphic HEMT MMICs and Modules Operating Between 300 and 500 GHz," in *IEEE Journal of Solid-State Circuits*, vol. 46, no. 10, pp. 2193-2202, Oct. 2011, doi: 10.1109/JSSC.2011.2163212.
- [96] Z. Liu, Z. Liu, Q. Li, X. Cheng and Y. Yao, "Microstrip Line to Waveguide Inline Transition for MMIC Integration," *2023 IEEE MTT-S International Wireless Symposium (IWS)*, Qingdao, China, 2023, pp. 1-3, doi: 10.1109/IWS58240.2023.10222307.
- [97] B. Zhang, Y. Zhang, C. Wu and T. Cao, "Millimeter-Wave Broadband Waveguide-to-Microstrip Transition Using a Bifurcated Probe," in *IEEE Microwave and Wireless Components Letters*, vol. 32, no. 9, pp. 1031-1034, Sept. 2022, doi: 10.1109/LMWC.2022.3169628.
- [98] V. Trifunovic and B. Jokanovic, "Review of printed Marchand and double Y baluns: characteristics and application," in *IEEE Transactions on Microwave Theory and Techniques*, vol. 42, no. 8, pp. 1454-1462, Aug. 1994, doi: 10.1109/22.297806.
- [99] K. U-yen, E. J. Wollack, S. Horst, T. Doiron, J. Papapolymerou and J. Laskar, "Slotline Stepped Circular Rings for Low-Loss Microstrip-to-Slotline Transitions," in *IEEE*

- Microwave and Wireless Components Letters*, vol. 17, no. 2, pp. 100-102, Feb. 2007, doi: 10.1109/LMWC.2006.890328.
- [100] M. M. Zinieris, R. Sloan, and L. E. Davis, "A broadband microstrip-to-slot-line transition," *Microwave and Optical Technology Letters*, vol. 18, no. 5, pp. 339-342, 1998, doi: [https://doi.org/10.1002/\(SICI\)1098-2760](https://doi.org/10.1002/(SICI)1098-2760).
- [101] B. Schiek and J. Kohler, "An Improved Microstrip-to-Microslot Transition (Letters)," in *IEEE Transactions on Microwave Theory and Techniques*, vol. 24, no. 4, pp. 231-233, Apr. 1976, doi: 10.1109/TMTT.1976.1128823.
- [102] C. López, V. Desmaris, and D. Meledin, "Design and Fabrication of All-metal Micromachined Finline Structures for Millimeter and Sub-millimeter Applications," in *Proceedings of the 32nd IEEE International Symposium on Space THz Technology (ISSTT 2022)*, Baeza, Spain, Oct. 16-20, 2022. [Online]. Available: <https://research.chalmers.se> Accessed: 17-Feb-2024.
- [103] A. R. Kerr et al., "Development of the ALMA Band-3 and Band-6 Sideband-Separating SIS Mixers," *IEEE Transactions on Terahertz Science and Technology*, vol. 4, no. 2, pp. 201-212, March 2014, doi: 10.1109/TTHZ.2014.2302537.
- [104] J. D. Garrett, B. -K. Tan, C. Chaumont, F. Boussaha, and G. Yassin, "A 230-GHz Endfire SIS Mixer With Near Quantum-Limited Performance," *IEEE Microwave and Wireless Components Letters*, vol. 32, no. 12, pp. 1435-1438, Dec. 2022, doi: 10.1109/LMWC.2022.3190701.
- [105] V. Y. Belitsky and M. A. Tarasov, "SIS junction reactance complete compensation," *IEEE Transactions on Magnetics*, vol. 27, no. 2, pp. 2638-2641, March 1991, doi: 10.1109/20.133753.
- [106] V. Belitsky, S. W. Jacobsson, L. V. Filippenko, and E. L. Kollberg, "Broadband twin-junction tuning circuit for submillimeter SIS mixers," *Microwave and Optical Technology Letters*, vol. 10, no. 2, pp. 74-78, 1995, doi: <https://doi.org/10.1002/mop.4650100203>.
- [107] V. Belitsky, C. Risacher, M. Pantaleev, and V. Vassilev, "Superconducting microstrip line model studies at millimetre and sub-millimetre waves," *International Journal of Infrared and Millimeter Waves*, vol. 27, pp. 809-834, Jun. 2006, doi: <https://doi.org/10.1007/s10762-006-9116-5>
- [108] A.R. Kerr, "Surface Impedance of Superconductors and Normal Conductors in EM Simulators," Electronics Division Internal Report No. 302, NRAO, February 1996.
- [109] A. Pavolotsky, T. Kojima, S. Masui, and V. Belitsky, "SIS technology development to serve Next Generation receivers for ALMA," in *Proceedings of the 32nd IEEE International Symposium on Space THz Technology (ISSTT 2022)*, Baeza, Spain, October 16-20, 2022. [Online]. Available: <https://research.chalmers.se> Accessed: 17-Feb-2024.
- [110] V. Belitsky, S. W. Jacobsson, S. A. Kovtonjuk, et al., "100 GHz mixer with vertically integrated (stacked) SIS junction array," *Int. J. Infrared. Milli. Waves*, vol. 14, pp. 949-957, 1993, doi: <https://doi.org/10.1007/BF02084571>.
- [111] P. Y. Aghdam, H. Rashid, A. Pavolotsky, V. Desmaris, D. Meledin and V. Belitsky, "Specific Capacitance Dependence on the Specific Resistance in Nb/Al-AlOx/Nb Tunnel Junctions," in *IEEE Transactions on Terahertz Science and Technology*, vol. 7, no. 5, pp. 586-592, Sept. 2017, doi: 10.1109/TTHZ.2017.2723803.

- [112] A. Pavolotsky, C. D. López, I. V. Tidekrans, D. Meledin, V. Desmaris, and V. Belitsky, "Specific capacitance of Nb/Al-AlN/Nb superconducting tunnel junctions," in *Proceedings of the 30th International Symposium on Space THz Technology (ISSTT2019)*, Gothenburg, Sweden, April 15-17, 2019.
- [113] J. Kawamura et al., "Very high-current-density Nb/AlN/Nb tunnel junctions for low-noise submillimeter mixers," *Appl. Phys. Lett.*, vol. 76, no. 15, pp. 2119–2121, 2000, doi: 10.1063/1.126272.
- [114] A. Khudchenko et al., "High-Gap Nb-AlN-NbN SIS Junctions for Frequency Band 790-950 GHz," *IEEE Trans. Terahertz Sci. Technol.*, vol. 6, no. 1, pp. 127–132, 2016, doi: 10.1109/TTHZ.2015.2504783.
- [115] C. F. J. Lodewijk, T. Zijlstra, S. Zhu, F. P. Mena, A. M. Baryshev, and T. M. Klapwijk, "Bandwidth limitations of Nb/AlN/Nb SIS mixers around 700 GHz," *IEEE Trans. Appl. Supercond.*, vol. 19, no. 3, pp. 395–399, 2009, doi: 10.1109/TASC.2009.2018231.
- [116] J. Guo, J. Xu, Y. Cui, and C. Qian, "Design of a W-band single-substrate single-waveguide power-combined frequency doubler," *2012 International Conference on Microwave and Millimeter Wave Technology (ICMMT)*, Shenzhen, China, 2012, pp. 1-4, doi: 10.1109/ICMMT.2012.6230469.
- [117] C. E. Groppi, C. Y. Drouet d'Aubigny, A. W. Lichtenberger, C. M. Lyons, and C. K. Walker, "Broadband Finline Ortho-Mode Transducer for the 750-1150 GHz Band," in *Proc. 16th International Symposium on Space Terahertz Technology*, Gothenburg, Sweden, May 2-4, 2005.
- [118] N. Scott Barker, M. Bauwens, A. Lichtenberger and R. Weikle, "Silicon-on-Insulator Substrates as a Micromachining Platform for Advanced Terahertz Circuits," in *Proceedings of the IEEE*, vol. 105, no. 6, pp. 1105-1120, June 2017, doi: 10.1109/JPROC.2016.2612191.
- [119] K. Murakami, Y. Wakabayashi, K. Minami and M. Esashi, "Cryogenic dry etching for high aspect ratio microstructures," *[1993] Proceedings IEEE Micro Electro Mechanical Systems*, Fort Lauderdale, FL, USA, 1993, pp. 65-70, doi: 10.1109/MEMSYS.1993.296953.
- [120] H. Rhee, H. Kwon, C. K. Kim, H. Kim, J. Yoo, and Y. W. Kim, "Comparison of deep silicon etching using SF₆/C₄F₈ and SF₆/C₄F₆ plasmas in the Bosch process," *Journal of Vacuum Science & Technology B: Microelectronics and Nanometer Structures Processing, Measurement, and Phenomena*, vol. 26, no. 2, pp. 576-581, 2008, doi: <https://doi.org/10.1116/1.2884763>.
- [121] A. R. Kerr, M. J. Feldman, and S.-K. Pan, "Receiver Noise Temperature, the Quantum Noise Limit, and the Role of the Zero-Point Fluctuations," in *Proc. Eighth International Symposium on Space Terahertz Technology*, Harvard University, March 1997.
- [122] B. D. Jackson et al., "Low-noise 0.8-0.96- and 0.96-1.12-THz superconductor-insulator-superconductor mixers for the herchel space observatory," in *IEEE Transactions on Microwave Theory and Techniques*, vol. 54, no. 2, pp. 547-558, Feb. 2006, doi: 10.1109/TMTT.2005.862717.
- [123] C. Risacher, V. Belitsky, V. Vassilev, I. Lapkin, and A. Pavolotsky, "A 275–370 GHz receiver employing novel probe structure," *International Journal of Infrared and Millimeter Waves*, vol. 26, pp. 867-879, 2005, doi: <https://doi.org/10.1007/s10762-005-5659-0>.

- [124] Y. Uzawa, Y. Fujii, A. Gonzalez, K. Kaneko, M. Kroug, T. Kojima, and S. Asayama, "Development and testing of Band 10 receivers for the ALMA project," *Physica C: Superconductivity*, vol. 494, pp. 189-194, 2013, doi: <https://doi.org/10.1016/j.physc.2013.04.008>.
- [125] N. Satou, Y. Sekimoto, Y. Iizuka, T. Ito, W. L. Shan, T. Kamba, and M. Sugimoto, "A Submillimeter Cartridge-Type Receiver: ALMA Band 8 (385--500 GHz) Qualification Model," *Publications of the Astronomical Society of Japan*, vol. 60, no. 5, pp. 1199-1207, 2008, doi: <https://doi.org/10.1093/pasj/60.5.1199>.
- [126] F. P. Mena et al., "Design and Performance of a 600–720-GHz Sideband-Separating Receiver Using AlOx and AlN SIS Junctions," *IEEE Transactions on Microwave Theory and Techniques*, vol. 59, no. 1, pp. 166-177, Jan. 2011, doi: [10.1109/TMTT.2010.2090417](https://doi.org/10.1109/TMTT.2010.2090417).
- [127] S. Mahieu et al., "The ALMA Band-7 Cartridge," in *IEEE Transactions on Terahertz Science and Technology*, vol. 2, no. 1, pp. 29-39, Jan. 2012, doi: [10.1109/TTHZ.2011.2177734](https://doi.org/10.1109/TTHZ.2011.2177734).
- [128] B. Billade, A. Pavolotsky and V. Belitsky, "An SIS Mixer With 2hf/k DSB Noise Temperature at 163 - 211 GHz Band," in *IEEE Transactions on Terahertz Science and Technology*, vol. 3, no. 4, pp. 416-421, July 2013, doi: [10.1109/TTHZ.2013.2255734](https://doi.org/10.1109/TTHZ.2013.2255734).
- [129] S. I. Asayama, T. Takahashi, K. Kubo, T. Ito, M. Inata, T. Suzuki, and Y. Uzawa, "Development of ALMA band 4 (125–163 GHz) receiver," *Publications of the Astronomical Society of Japan*, vol. 66, no. 3, pp. 57, 2014, doi: <https://doi.org/10.1093/pasj/psu026>.
- [130] A. Khudchenko et al., "Design and Performance of a Sideband Separating SIS Mixer for 800–950 GHz," in *IEEE Transactions on Terahertz Science and Technology*, vol. 9, no. 6, pp. 532-539, Nov. 2019, doi: [10.1109/TTHZ.2019.2939003](https://doi.org/10.1109/TTHZ.2019.2939003).
- [131] M. Yao, D. Liu, B. -L. Liu, K. Zhang, J. Li and S. -C. Shi, "Characterization of an All-NbN Superconductor-Insulator-Superconductor Mixer for HSTDM," *2020 XXXIIIrd General Assembly and Scientific Symposium of the International Union of Radio Science*, Rome, Italy, 2020, pp. 1-4, doi: [10.23919/URSIGASS49373.2020.9232148](https://doi.org/10.23919/URSIGASS49373.2020.9232148).
- [132] T. Kojima, H. Kiuchi, K. Uemizu, Y. Uzawa, M. Kroug, A. Gonzalez, and T. Kageura, "Demonstration of a wideband submillimeter-wave low-noise receiver with 4–21 GHz IF output digitized by a high-speed 32 GSps ADC," *Astronomy & Astrophysics*, vol. 640, L9, 2020, doi: <https://doi.org/10.1051/0004-6361/202038713>.
- [133] K. Rudakov et al., "Low-noise THz-range Nb based SIS Receivers for Radio Astronomy," *2020 45th International Conference on Infrared, Millimeter, and Terahertz Waves (IRMMW-THz)*, Buffalo, NY, USA, 2020, pp. 1-2, doi: [10.1109/IRMMW-THz46771.2020.9370465](https://doi.org/10.1109/IRMMW-THz46771.2020.9370465).
- [134] J. D. Garrett, C. -Y. E. Tong, L. Zeng, T. -J. Chen and M. -J. Wang, "A 345-GHz Sideband-Separating Receiver Prototype With Ultra-Wide Instantaneous Bandwidth," in *IEEE Transactions on Terahertz Science and Technology*, vol. 13, no. 3, pp. 237-245, May 2023, doi: [10.1109/TTHZ.2023.3263626](https://doi.org/10.1109/TTHZ.2023.3263626).
- [135] J. W. Kooi et al., "Performance of the Caltech Submillimeter Observatory Dual-Color 180–720 GHz Balanced SIS Receivers," in *IEEE Transactions on Terahertz Science and Technology*, vol. 4, no. 2, pp. 149-164, March 2014, doi: [10.1109/TTHZ.2013.2293117](https://doi.org/10.1109/TTHZ.2013.2293117).

- [136] A. Pavolotsky, V. Desmaris, and V. Belitsky, "Nb/Al-AlN/Nb superconducting tunnel junctions: fabrication process and characterization results," in *Proceedings of the 29th IEEE International Symposium on Space THz Technology (ISSTT2018)*, Pasadena, CA, USA, March 26-28, 2018, pp. 107-111.
- [137] Belitsky V., Serpuchenko I.L., Tarasov M.A., Vystavkin A.N., "MM Waves Detection Using Integrated Structure with SIS Junction, Stripline Transformer and Spiral Antenna," *Extended Abstracts of ISEC'89*, Tokyo, Japan, 1989, pp. 179-182.
- [138] A. Karpov *et al.*, "Low Noise 1 THz–1.4 THz Mixers Using Nb/Al-AlN/NbTiN SIS Junctions," in *IEEE Transactions on Applied Superconductivity*, vol. 17, no. 2, pp. 343-346, June 2007, doi: 10.1109/TASC.2007.898277.
- [139] "ALMA Science Portal," About ALMA - ALMA Basics. [Online]. Available: <https://almascience.eso.org/about-alma/alma-basics>. Accessed: 16-February-2024.
- [140] J. W. Kooi *et al.*, "A 275–425-GHz Tunerless Waveguide Receiver Based on AlN-Barrier SIS Technology," in *IEEE Transactions on Microwave Theory and Techniques*, vol. 55, no. 10, pp. 2086-2096, Oct. 2007, doi: 10.1109/TMTT.2007.905503.
- [141] K. Y. Liu, M. J. Wang, C. E. Tong, P. Friberg, G. A. Fuller, T. J. Chen, and W. Zhong, "SIS mixers study on Heterodyne Array Receiver Program (HARP) at JCMT," in *Millimeter, Submillimeter, and Far-Infrared Detectors and Instrumentation for Astronomy X*, Vol. 11453, pp. 608-615, SPIE, December 2020, doi: <https://doi.org/10.1117/12.2561192>.
- [142] J. Treuttel *et al.*, "Jupiter Icy Moon Explorer, Submillimeter wave Instrument: Status and performances of the 1200 GHz high spectral resolution receiver front end," *2020 14th European Conference on Antennas and Propagation (EuCAP)*, Copenhagen, Denmark, 2020, pp. 1-4, doi: 10.23919/EuCAP48036.2020.9135975.
- [143] K. Schmalz, A. Glück, N. Rothbart, A. Güner, M. H. Eissa, and H.-W. Hübers, "Transmitter and Receiver in 0.13 μm SiGe for Gas Spectroscopy at 222–270/444–540 GHz," *IEEE Journal of Microwaves*, vol. [volume number], no. [issue number], pp. [page numbers], Aug. 2022, doi: 10.1109/JMW.2022.3194062.

